A study of the sulfur problem in *Mary Rose* timbers using X-ray techniques

by

Aaron Berko

A thesis submitted to the University of Kent for the Degree of Doctor of Philosophy in Chemistry in the Faculty of Science, Technology and Medical Studies

School of Physical Sciences

The University of Kent

March 2011

Dedication

This thesis is dedicated to the memory of my brother Reginald Berko.

DECLARATION

No part of this thesis has been submitted in support of an application for any degree or qualification of the University of Kent or any other university or institute of learning.

Aaron Berko

30th March 2011

ABSTRACT

This thesis reports a study of the *sulfur problem* which is the production of sulfuric acid via the oxidation of iron sulfide in the timbers of the *Mary Rose* a flagship of Henry VIII's navy which sunk in 1535 and was raised in 1982. The work has involved a range of chemical and physical techniques with particular use of synchrotron sources to measure the iron and sulfur speciation in the timbers with X-ray absorption spectroscopy (XAS) measurements.

XAS measurements are almost unique in providing the speciation of atoms in a sample via the XANES. They are particularly useful for sulfur, which has a wide range of oxidation states. However, the current work has shown the need to use the bulk and microfocus XAS measurements in parallel, particularly for archaeological samples. It is clear that the iron and sulfur contents and speciation can vary widely from sample to sample of the *Mary Rose* timbers. In the study on the effectiveness of chelating agents in the removal of iron species from the timbers care was taken, wherever possible, to ensure that the same samples and sample positions were used for the before and after treatment measurements.

The nature of the iron and sulfur species is of extreme importance because it is assumed that it is Fe^{2+} that gives rise to the production of sulfuric acid. The current study has shown that in the timbers that had not been PEG treated contained iron in the surface regions that was predominantly Fe^{3+}, similar to the findings of other workers. Most of the work in this thesis used samples close to the surface of the timbers. It was only in samples taken deep into the timbers experiments that there were significant concentrations of Fe^{2+}. A range of sulfur species were found in the samples. The predominant species were reduced sulfur species, elemental sulfur and sulfate. Very little pyrite was found in the timbers studied, but it should be noted that these timbers had not been PEG treated. Some pyrite was found in the cell walls. The present studies were predominantly on the surface regions of the timbers and the conclusion is that the bulk of the pyrite which may have been present had oxidised in the moist, oxygen containing environment in which they had been stored after recovery from the sea bed.

A key finding of the present study is the co-location of iron and sulfate in the timbers. This had been suggested but had not been experimentally verified. The production of sulfuric acid in the timbers is thought to involve the oxidation of iron sulfides in the presence of water to produce is iron sulfate and sulfuric acid. The fact that the present experiments show iron and sulfate in the same positions in the XANES maps strongly supports the proposed oxidation mechanism of iron sulfides.

The bulk and microfocus XAS experiments show that a large fraction of the iron in the current samples was in the form of an oxide. This is most likely to be goethite (FeO(OH)). The XANES analysis and the fitting of the EXAFS are consistent with this identification.

All the four chelating agents used in this work (EDTA, DTPA, ammonium citrate and calcium phytate) were effective in removing iron from the timbers. However, the more efficient are DTPA and calcium phytate in terms of amount removed at fixed molarity. For samples that had been treated with PEG the current work showed that the chelating agents were less effective. This is presumably due to the PEG blocking the penetration of the solutions of the chelating agents into the wood.

ACKNOWLEDGEMENTS

I would like to first of all thank the Lord Jesus for His faithfulness and unconditional love. My life has been full of His favour and blessings, so much so that I am sometimes overwhelmed by His extravagant love.

I would also like to thank Dr Ellie Schofield for her support in XAS experiments at Diamond light source and Soleil, especially the second run at I18 in 2009. Thank you also to her for offering her support and expertise in the analyses of the data collected in some three beam time awards.

I would like to thank Professor Mark Jones from the *Mary Rose* Trust for his support throughout this project; the *Mary Rose* samples, chemicals, countless journals and resources that I received from him and the people at the trust, thank you and may God bless you. Thanks also to the *Mary Rose* Trust for funding my research and making it possible for me to complete my research without resorting to busking on Canterbury high street every weekend; I am indebted to you.

Thank you to Dr Andy Smith, I have not met many people like him. He is always willing to offer his expertise and support on every beam time award. He is never reluctant to advice and offer practical help even if it means staying till the early hours of the morning. He was always ready to give his time to help with the analysis and interpretation of results, especially the data from 16.5 and on the arrow tip data from I18. I am almost lost for words in expressing my deep sense of gratitude and admiration for him. Thank you and God bless you richly.

To Dr Fred Mosselmans, thank you for your support and great sense of humour. Coming to I18 was always a joyous occasion is spite of the long hours and sometimes less than appetising meals. Your expertise and ability to make complex things accessible to everyone is inspiring. Thank you and God bless you.

I would like to acknowledge Bob Bilsborrow at the SRS Daresbury for his support on the experiments at station 16.5.

I would like to say a big thank you to Dr Aran Blacklocks for his support and company in room 230, Ingram and also for his help with the exafs software in the early days of my program. I would like to say thank you to Zoe Green and Lorna Keast; second year interns for their support in some of the preliminary work on cellulose and oxidation rates. Dr Mike Cole is also thanked for help on the SEM.

To Dr Gavin Mountjoy, Dr Maria Alfredsson and Professor Robert Newport of the Functional Materials group, thank you for your encouragement and support.

I would like to thank James Redmond, Sarah Saunders and Pat Baldock of the School of Physical Sciences for their support throughout this research.

Now to Professor Alan Chadwick, who I think is a fantastic human being and by far the best boss I have ever had, thank you. I know words are not adequate to express my gratitude but I will try. I have not met many people like him and I am convinced anyone will struggle to meet many like him. His expertise in his field is well celebrated; he has been a long standing member of the University and a very well respected and loved practitioner of materials chemistry research. There are not many things and people in the field he does not know yet, he is humble and a pleasure to be around. He has been more than a PhD supervisor to me and I am most grateful to God that I have had the chance of knowing this great man and personality. He always has a story to tell and they are most times funny and insightful. Spending long hours at synchrotron stations are never fun at the best of times but that never deters him from accompanying his students to every beam time and giving them support. I know the black pudding in the mornings is always an incentive but his determination to give his best to his students is truly amazing.

Three times I wanted to quit my PhD; the second time was when my brother was killed and I was convinced I would not be able to continue. Professor Alan Chadwick found the words to encourage me and he has supported me till the very end. He has been a great inspiration to me and I will forever be grateful to him. I would not be where I am if not for the support I have received from him over my many years in the university of Kent; first as an undergraduate and then as a PhD student. Thank you and God bless you richly.

I would also like to say a big thank you to members of New Life Church Canterbury, especially the senior leadership team for their love and support throughout this research. Special mention to Dr William White for his support and kindness to me in the times I most needed it. May the good Lord bless and recompense him for every investment he has made in my life. Also Carolline Agoi, for her friendship and her support as my assistant in the Chaplaincy and also in the Church; may God bless her for her dedication to God and His people. To Sarah Ahorsu, Shadreck and Violet Chikomba, Peter and Rosamund Duffort, and the entire leadership team of New Life Church; God bless you and thank you for your loving kindness and support.

To my siblings Leslie, Elsie, Lloyd, Yvonne and not forgetting the late Reginald, thank you for being such wonderful people. Your love and support helped me through some of the most difficult times in my life, may God bless you all richly.

To the best parents anyone could ask for; James and Victoria Berko, thank you and God bless you for all you have done and continue to do in my life. Your prayers and words of encouragement have been a great source of strength for me, thank you. I hope this thesis will fill you with a sense of pride and great accomplishment because truthfully I couldn't have done it without you both.

To my fiancé and soon to be wife, Adelaide Akua Agyei, big God bless you for the great joy and happiness you have brought to my life. At a moment when I was feeling unmotivated to finish this PhD,

you walked into my life and brought a ray of sunshine and great delight. You are a confirmation of God's abundant love for me because only He could have sent someone so perfectly suited to me. I would like to share this accomplishment with you and most importantly I look forward to sharing the rest of my life with you.

To all those I have failed to mention, please charge it to my head and not my heart. This thesis would not be able contain all the names of the people I know I need to thank if I were to write down all your names. Thank you and God bless you all.

GLOSSARY OF NOMENCLATURE

Am. Cit.	Ammonium citrate
Cal. Phy.	Calcium phytate
Cit Ac	Citric Acid
CN	Coordination number
DTPA	Diethylenetriaminepentaacetic acid
EDMA	Ethylenediiminobis(2-hydroxy-4-methylphenyl)acetic acid,
EDTA	Ethylenediaminetetraacetic acid
EDX	Energy dispersive X-ray spectroscopy
E_e	Fermi energy
EXBACK	Daresbury EXAFS background subtraction programme
EXCALIB	Daresbury EXAFS calibration programme
EXCURV98	Daresbury EXAFS fitting programme
EXSPLINE	Daresbury EXAFS background subtraction programme
NEXAFS	Near edge X-ray absorption fine structure (XNES)
N_j	Number of atoms in coordination shell
PEG	Polyethylene glycol
PIXE	Particle induced X-ray emission
R_j	Radial distance
SEM	Scanning Electron Microscope
S.S.D	Solid State Detector
XAFS	X-ray Absorption Fine Structure
XANES	X-ray Absorption Near-Edge Spectroscopy
XAS	X-ray Absorption Spectroscopy
XRD	X-ray diffraction
XRF	X-ray fluorescence
θ	Angle
λ	Wavelength
σ	EXAFS Debye-Waller factor

TABLE OF CONTENTS

I. INTRODUCTION

I.1 The History of the *Mary Rose*

I.1.1 Construction

The *Mary Rose* warship, a firm favourite of King Henry VIII, was built between 1509 and 1511. It was built by the king in an effort to expand his navy to stem the threats from France and Scotland. She was one of the first ships able to fire canons from the broadside enjoying a successful career for several years until its unceremonious sinking in 1545. It was constructed mainly using oak timbers which were held together by iron bolts. Oak was a desirable material for the construction of ships because it is soft and easily shaped whilst fresh but dries to form a strong and solid structure which is resistant to water. Oak trees are also big and tall enough to use as main deck beams which on the *Mary Rose* were constructed from single pieces of timber spanning the width of the hull. It was built using the carrack style; the hull contained four levels separated by three decks. The gun ports were above the orlop (lower) deck with each side of the hull containing seven gun ports. The gun ports had heavy lids which rendered the gun ports watertight when closed [1, 2].

I.1.2 Sinking

On the 19th of July 1545, on its way to engage the French fleet and stop them from landing on the Isle of Wight, the *Mary Rose* sank in the river Solent, a few miles from the Portsmouth harbour [2]. Henry VIII and onlookers who had gathered to bid the crew farewell watched as the ship capsized and sank in a few metres of water. No one is really sure why the *Mary Rose* sank but it is reported that it was carrying 700 crewmen and stock instead of the 400 it was built to carry [3]. The ship made a sharp turn and began to capsize probably due to the heavy load it was carrying. Water began to pour into the gun ports and this lead to its sinking. It lay under the sea bed for some 437 years until it was re-discovered and raised in 1982 with millions of people watching on live television. Almost half of the ship was preserved due it being buried in silt which provides an anoxic (free of oxygen) environment restricting the action of wood degrading bacteria and protecting it from wood

boring sea-life. In addition to the ship some 20,000 artefacts have also been recovered providing a unique insight into life at sea in Tudor times [1].

I.1.3 Conservation

Wood degradation occurs rapidly due a variety of processes when it is exposed to wet and humid environmental conditions. It can however be preserved under two specific conditions; firstly being when the wood is kept dry such as a dry tomb chamber and secondly under anoxic conditions like being buried under silt in the ocean bed.

A sketch of the structure of wood is shown in Figure 1. The structure of wood and its mechanical strength is based mainly on the use of two biopolymers; cellulose and lignin. Cellulose provides wood with tensile strength and lignin in the cell wall provides resistance to compression [4]. Wood can be affected by wood degrading bacteria in aerobic conditions. These micro bacteria affect the wood by degrading the cell walls mainly through the breakdown of cellulose and a third constituent of wood called polyose [5]. Lignin is more difficult to breakdown than cellulose as it is indigestible by mammalian and other animal enzymes; however some fungi and bacteria are able to biodegrade the polymer. When wooden artefacts sink to the seabed, they are initially exposed to such microbial agents that begin to degrade the wooden structure.

The main wood degraders in sea water are marine borers like the shipworms *teredinidae* and *limnoria*. These will rapidly degrade wood constituents that are exposed above the seabed. Over a period of time these artefacts can become covered with silt which creates anoxic conditions.

When the *Mary Rose* sank, it would have been initially susceptible to biological (microbial) degradation until the anoxic conditions were created. Such microbial degradation results in the breakdown of these important polymers and consequently the weakening of the wood. Biological degradation leads to a marked decrease of mechanical strength and the integrity of the wood decreases due to the loss of material and the creation of voids in the structure.

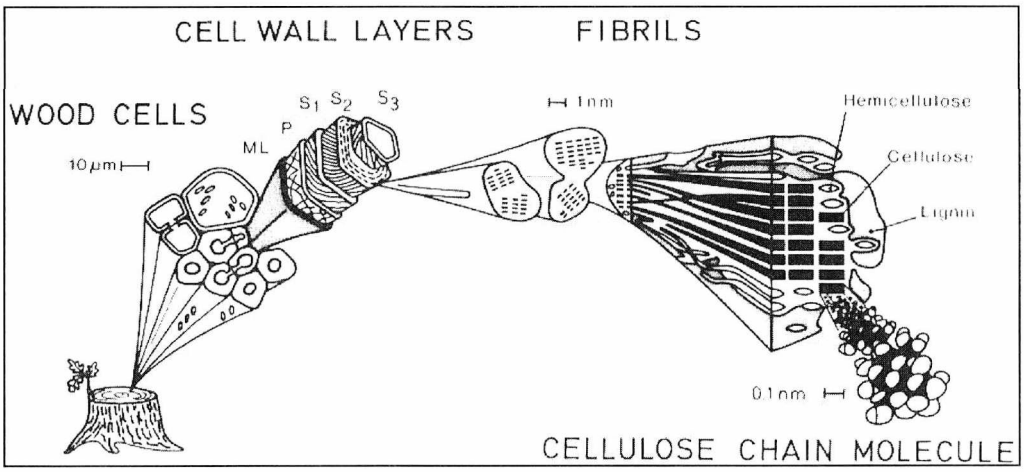

Figure 1: A schematic representation of the structure of wood.

Christensen came up with a scheme in 1970 that described the degree of physical degradation of wood in terms of loss of material [6]. Woods that are easily degraded were put in class one and woods that were degraded least were put in class three. Oak which was used to construct the *Mary Rose* was placed in class three [6].

Biological wood decay occurs due the action of bacteria and fungi in damp and oxygen rich environments. The action of fungi on oak is limited and this could be due to presence of tannates, biochemical components which act as fungicides. Some bacteria function in anaerobic conditions using iron (III) to iron (II) and the sulfate to sulfide redox couple to drive their digestive processes [7].

One other process that affects wood causing degradation is chemical activity. This is referred to as chemical degradation and it occurs through oxidation and hydrolysis, which will be discussed later.

Soon after it was raised, scientist began the mammoth task of preserving this national treasure. This started with the spraying of the ship and some of the larger artefacts with polyethylene glycol, $(CH_2CH_2O)_n$, (PEG). PEG is a simple, linear chain polymer that is available in a wide range of molecular weights (from 156 – known as tetraglyme- to 5,000,000), is non-toxic, colourless, water soluble and inexpensive. The properties of PEG vary from liquid to waxy to soft solid as the molecular weight increases. Most waterlogged wooden artefacts are freeze-dried; this can however give rise to

volume changes that can cause the wood to crack. For this method to be effective in preserving the wooden artefact, a cryoprotectant or a consolidant must be used. The purpose of a cryoprotectant is to reduce the volume changes as the wood cools through water's freezing point. Previously used cryoprotectants include glycerine, creosote and alum, however the most commonly used cryoprotectant in recent times is PEG. This is because PEG is compatible with borax (sodium borate, $Na_2B_4O_7 \cdot 10H_2O$, a fungicide commonly used in wood), it also easy to handle and it readily available and relatively cheap. Conservators working on the *Mary Rose* employed this method.

The treatment of the *Mary Ro*se timbers followed the following series of stages. First, the ship was sprayed with chilled water for several years. This was to wash out some of the salt precipitates and bacterial agents from the ships timbers. This also kept the ship wet and prevented it from drying and cracking. The timbers were then sprayed with solutions of the shorter chain PEG's. The smaller molecules move easily into the damaged wood, including the less damaged wood deeper into the timbers. Then the whole process was repeated with long chain PEG's gradually replacing the shorter chain ones. Longer chain PEG's will not be able to penetrate the less damaged deeper part of the timbers, but they will displace the shorter PEG's from the more easily accessible surface areas. The idea is the surface will then not have the tacky feel when dried which is the case when shorter chain PEG's are used. As mentioned before the use of PEG's will also prevents the wood from shrinking and cracking when dried.

The *Mary Rose* is currently being sprayed with longer chain PEG's (molecular weight 2000). The process is due to continue for the next three years.

Figure 2: Recent picture of the *Mary Rose* (courtesy of the *Mary Rose* Trust)

I.2 The Sulfur Problem in Water-logged Archaeological Wood

The production of sulfuric acid and its effects on marine wooden artefacts known as the *sulphur problem* has become a major concern for conservationist in recent years. The problem was highlighted by scientists working on the restored 17th century Swedish warship *Vasa* in 2000 [9]. This problem is more pronounced in artefacts that have been in the seabed as opposed to riverbeds.

Wooden marine artefacts like the *Mary Rose* can be preserved under the seabed for several years due the slowing down of microbial degradation due to anoxic conditions created by silt covering the artefacts. These conditions inhibit the mechanisms of wood degradation by bacteria and thus preserve such wooden artefacts. However these conditions are also ideal for sulfur reducing bacteria (SRB). Large numbers of sulfur compounds exist naturally in the sea at different oxidation states. For example, hydrogen sulfide (H_2S), pyrite (FeS_2), sulfates (SO_4^{2-}), sulfur dioxide (SO_2), elemental sulfur (S) and where iron is present, iron sulfide (FeS). Under anaerobic conditions sulfur reducing bacteria of the genus *Desulfovibrio* and *Desulfotomaculum* can turn sulfates and thiosulfates or other reducible sulfur species into hydrogen

sulfide. These micro-organisms are heterotrophic, that is they depend on complex organic substances for nutrition. They utilize sulfates (SO_4^{2-}), thiosulfates($S_2O_3^{2-}$), sulfites (SO_3^{2-}), or other reducible sulfur-containing ions as terminal electron acceptors in their respiratory processes. In the process these sulfur containing ions are reduced to hydrogen sulfide. A simplified overall reaction is given below [10].

$$2CH_2O + SO_4^{2-} \rightarrow H_2S + 2HCO_3^-$$

In the above reaction, $2CH_2O$ represents organic matter, i.e. cellulose.
Hydrogen sulfide can easily penetrate degraded waterlogged wood and react with organic matter. These sulfur species can accumulate in the wood over time and once exposed to oxygen rapidly oxidise to sulfates and eventually sulfuric acid. This process is thought to be catalysed by the presence of iron [11].
The sulfur problem was detected in the timbers of Tudor ship, the *Mary Rose* soon after the discovery of the effects seen in the *Vasa* timbers. A number of the wooden artefacts, such as arrows and dagger handles, showed a blackening where there had been contact with iron parts. Also a number of artefacts showed mineral aggregates (later identified as iron sulfates) on the surface.
The formation of sulfur salts was first discovered on dried and displayed wooden artefacts in the *Mary Rose* Museum. Like the *Vasa*, it was discovered that the problem was more pronounced in areas where there used to be iron bolts or fastenings (Figure 3) or where the wood was in direct contact with iron, like in a dagger (Figure 4).

Figure 3: Handle of a wooden chest from the *Mary Rose.* The arrow marks the degradation.

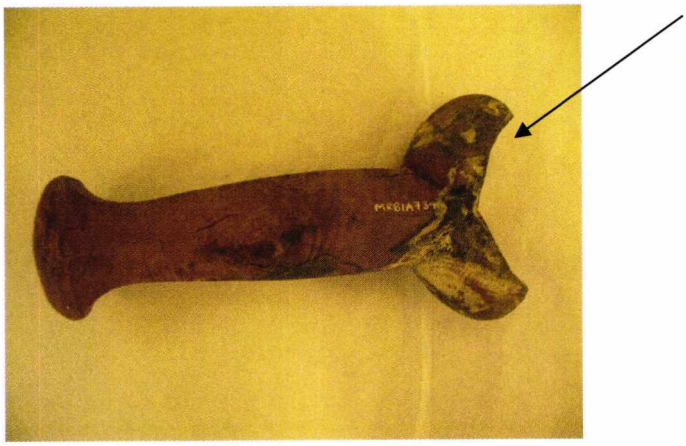

Figure 4: Dagger handle from the *Mary Rose.* The arrow marks the degradation.

This led to the suggestion that the iron may be playing a catalytic role in the formation of the sulfuric acid. The iron found in the wood of the *Mary Rose* is mainly from corroding iron bolts and fastenings which were commonly used in ship building in the early years. This iron readily binds with sulfur to form iron sulfide. This is oxidised in humid conditions to form iron sulfate and sulfuric acid [12].

$$2\ FeS_2 + 7O_2 + 2\ H_2O \rightarrow 2\ FeSO_4 + H_2SO_4$$

Analyses show the presence of various iron species present in the wood [8]. However it is believed that the iron (II) sulfide species is primarily responsible for the production of sulfuric acid [13]. The iron present on the ship began to corrode almost immediately once it came into contact with the sea water.

Electrolytic corrosion can be used to explain why the iron bolts holding the *Mary Rose* corroded so extensively in the sea bed [14]. The exposed end of an iron fastener shows evidence of hydroxyl ions (OH^-) formation [15]. This indicates that the exposed head of the iron bolt forms a cathode and the shank forms the anode of a galvanic cell.

The chemical reactions occurring in such a galvanic cell can be written as;

$$\text{Cathode: } O_2 + 2H_2O + 4e \rightarrow 4OH^-$$

$$\text{Anode: } Fe \rightarrow Fe^{2+} + 2e$$

These ferrous ions liberated are unstable and oxidise to form ferric ions (Fe^{3+}). In anaerobic conditions, the oxidation of ferrous ions to ferric ions will be slow and both iron (II) and iron (III) species will typically be present. These ions go on to form either black iron tannate dyes or rust. Iron ions catalyse chemical reactions that cause strength loss to cellulose [16]. In marine environments, the presence of chloride ions can form acidic conditions around the iron bolt which accelerates the corrosion of the iron bolts which in turn further the damage the wood. The corrosion of these iron bolts frees up iron ions which penetrate the wood (the level of penetration depends on porosity) and combine with sulfur to form iron sulfide. Iron sulfide has been identified as the intermediate in the formation of sulfuric acid in recovered marine archaeological wood.

A great deal of research has also been dedicated to the investigation of microbially influenced corrosion of metals and some bacteria have been reported to accelerate the corrosion of metals.

Sulfur reducing bacteria like *desulfovibrio desulfuricans, Pseudomas sp* and *bacillus sp* have been reported to accelerate metal corrosion [17].

Microbially influenced corrosion of metals is dependent on the morphology of biofilms secreted by these bacteria on the surface of metals. A porous biofilm will trap metabolites secreted by the bacteria as well as create pH gradients, dissolved oxygen and chlorides over time. This alters and detrimentally influences the immediate region of the metal surface leading to localised corrosion on the metal surface. In contrast a compact non-porous biofilm could act as a protective film on the metal surface preventing corrosion [18].

As mentioned before, sulfur reducing bacteria like *desulfovibrio desulfuricans* utilise sulfates (SO_4^{2-}), thiosulfates ($S_2O_3^{2-}$), sulfites (SO_3^{2-}), or other reducible sulfur-containing ions as terminal electron acceptors in their respiratory processes.

Kuhr *et al* [19] proposed that the following reactions occur in such a process;

$$4Fe \rightarrow 4Fe^{2+} + 8e^- \quad \text{(anodic reaction)}$$

$$8H_2O \rightarrow 8H^+ + 8OH^- \quad \text{(water dissociation)}$$

$$8H^+ + 8e^- \rightarrow 4H_2 \quad \text{(cathodic reaction)}$$

$$SO_4^{2-} + 4H_2 \rightarrow S^{2-} + 4H_2O \quad \text{(bacteria consumption)}$$

$$Fe^{2+} + S^{2-} \rightarrow FeS \quad \text{(corrosion products)}$$

$$4Fe + SO_4^{2-} + 4H_2O \rightarrow 3\,Fe(OH)_2 + FeS + 2OH^- \quad \text{(overall reaction)}$$

The overall process is a cathodic depolarisation with the sulfur reducing bacteria consuming the hydrogen accumulated at the cathode by a hydrogenase enzyme [20]. Researchers have theorised that corrosion is accelerated due to the cathodic reduction of H_2S:

$$H_2S + 2e^- \rightarrow H_2 + S^{2-}$$

The anodic reaction is in turn accelerated by the formation of iron sulfide:

$$Fe + S^{2-} \rightarrow FeS + 2e^-$$

This model is however accepted to be too simplistic to fully explain this phenomenon since many factors may be involved in sulfur reducing bacteria

influenced corrosion [21, 22]. Sulfur reducing bacteria thus not only increase the sulfur content in the woods but may also contribute to the corrosion of iron in the ship leading to an increase in the amount of iron distributed in the timbers of the *Mary Rose.*

X-ray maps of core samples from the *Mary Rose* hull taken using scanning electron microscopy (SEM) show that; the iron content decreases with increasing depth of the *Mary Rose* hull. The sulfur content was on the other hand found to generally increase with increasing depth. This trend is however not consistent throughout the samples we analysed. This could be due to the way the ship was laying whilst it was in the seabed [see Figure 5 below]. This means the formation of sulfuric acid should be more pronounced near the surface of the wood depending on its porosity.

Figure 5: *Mary Rose* lying on its side on the seabed.

I.2.1 Effects of Sulfuric Acid on Wood

The presence of sulfuric acid in these archaeological woods can further degrade the wooden structure by catalysing the hydrolysis of cellulose which provides the wood with mechanical strength [23]. The mechanism of this acid catalysed hydrolysis is shown below (Scheme 1)

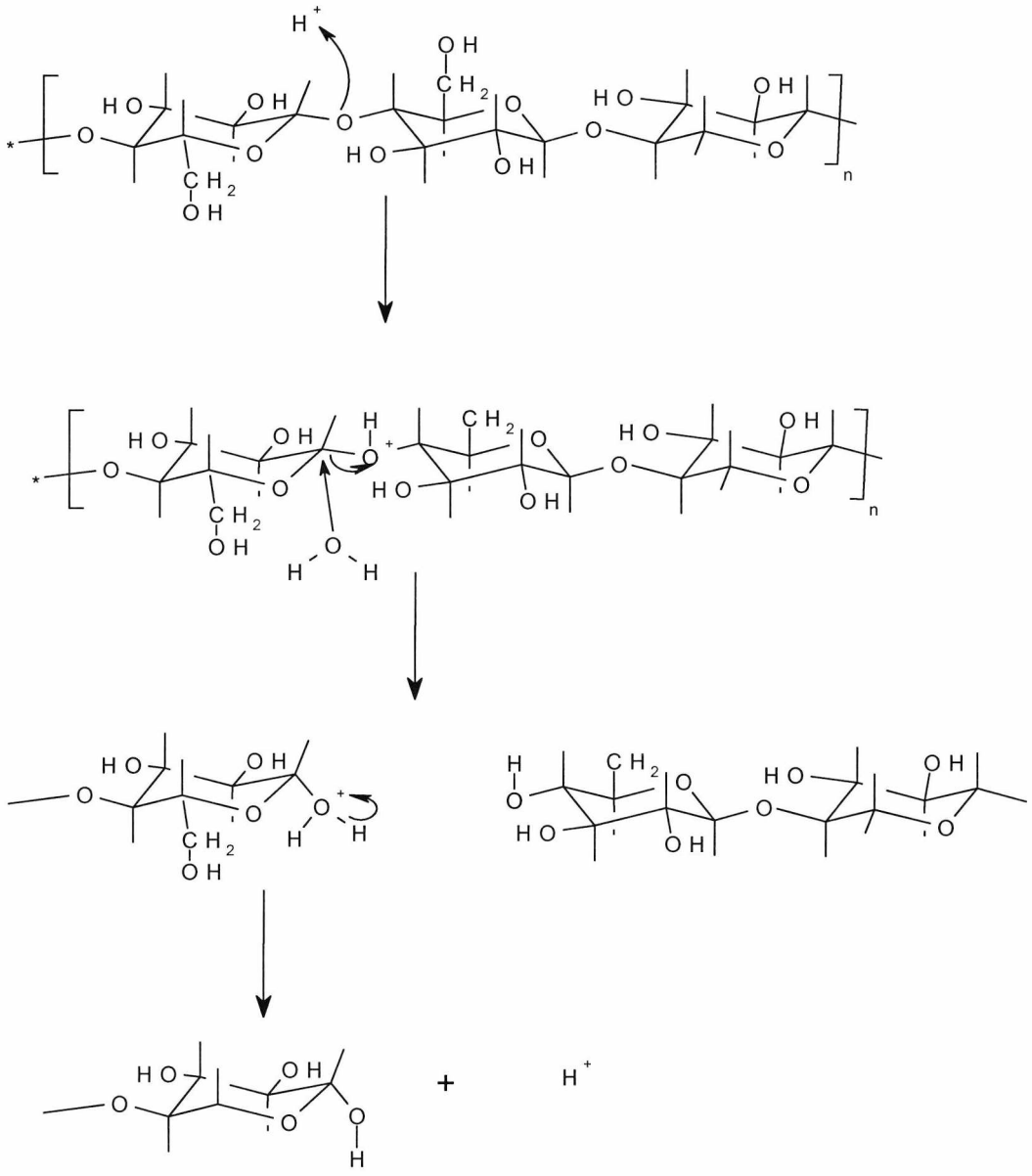

Scheme 1: Acid hydrolysis of cellulose.

Acid hydrolysis proceeds in three steps:

1. The reaction starts with a proton from the acid interacting rapidly with the glycosidic oxygen linking two sugar units, forming a conjugate acid.
2. The cleavage of the C-O bond and breakdown of the conjugate acid to the cyclic carbonium ion then takes place, which adopts a half-chair conformation.
3. After a rapid addition of water, free sugar and a proton are liberated [24].

Allowing the build up of sulfuric acid or any acid for that matter in these archaeological woods would therefore further reduce their mechanical strengths. SEM images of samples from the *Mary Rose* show such degradation of cell walls which substantially reduce mechanical strength [Figure 6].

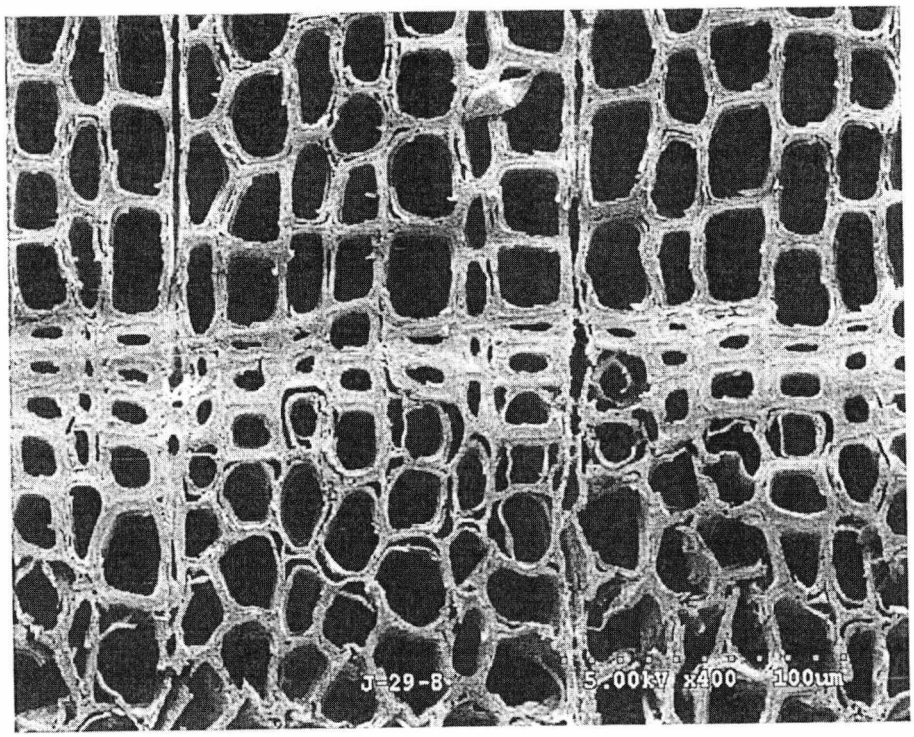

Figure 6: SEM image of sample from a poplar arrow from the *Mary Rose* showing the breakdown of cell walls (courtesy of the Mary Rose Trust).

I.3 Objectives of Present Study

The task is to find a way to stop the formation of sulfuric acid or its activities in these archaeological woods or at the very least slow it down by a considerable amount.

There are three ways this could be achieved:

1. Remove all sulfur species present in the wood
2. Remove iron ions from the wood
3. Create a surface barrier to prevent oxygen/moisture/bacteria entering the wood
4. Incorporate alkaline nanoparticles into the wood to neutralise any acid that if formed over time.

The current research has the following objectives:

1. To investigate the effectiveness of chelating agents in the removal of iron from *Mary Rose* timbers. This objective was chosen as opposed to investigating the removal of sulfur species because there are a number of agents that chelate iron ions very well to form very stable complexes. This will render the iron inactive and thus not being able to catalyse the formation of sulfuric acid. Some of these chelating agents like DTPA and EDMA (ethylenediiminobis(2-hydroxy-4-methylphenyl)acetic acid),render the iron species soluble in water which means the resulting complex could then be washed out of the wood. Some of these chelating agents have mild or moderate toxicity levels and this makes them desirable in conservation.

2 To use a range of analytical (including methods using synchrotron radiation) and chemical techniques will be employed to test the effectiveness of the treatments with chelating agents.

3 Investigate the role of iron (especially iron (II)) in the formation of sulfuric acid and the breakdown of cellulose.

II. METHODOLOGY

II.1 X-ray techniques

II.1.1 Generating X-rays

X-rays have shorter wavelengths and consequently higher energies compared to other electromagnetic waves like visible light and ultraviolet waves. In 1895 the German physicist Wilhelm Roentgen discovered X-rays quite fortuitously when experimenting with vacuum tubes. His discovery transformed the world of medical imaging and X-rays have been routinely used in medical imaging ever since. He coined the term Roentgen rays to refer to this new form of radiation but the term X-rays were later adopted due to it being an unknown type of radiation at that time.

This discovery has led to giant leaps in analytical methods in physical science; X-ray diffraction was developed soon afterward the discovery as the basis for structural investigation in solid state physics, chemistry, geology and eventually, biology. This was followed by X-ray spectroscopic techniques for microanalysis and mapping of electron energy levels. [25]

X-rays are a form of radiation with capabilities of penetrating materials that normal light cannot penetrate, thus they useful for photographing the inner parts of the human body from the outside.

A vacancy in an atomic shell plays an important role in physics and chemistry. Defined as an electron missing from the normal complement of electrons in a given atomic shell, a vacancy can be produced in various ways for example; Compton scattering, photoelectric effect and triplet production. An atom with a vacancy in its inner shell is in a highly excited state and returns to its ground state through a series of electronic transitions. Electrons from higher atomic shells will fill the shell vacancies and the energy difference in binding energies between the initial and final shell or sub-shell will be emitted from the atom in one of two ways:

1. Characteristic X-rays
2. Auger electrons [26].

Generating characteristic X-rays is fairly straightforward. A cathode and an anode that sit inside a glass vacuum tube are needed to generate X-rays in the laboratory. This is shown schematically in Figure 7.

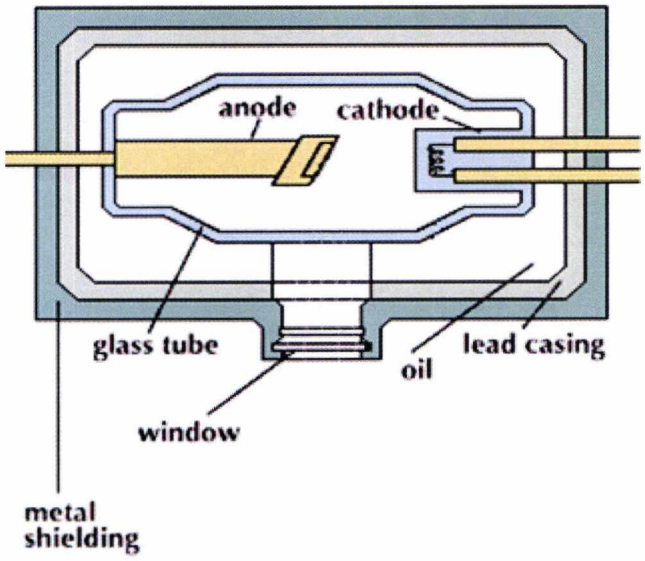

Figure 7: A schematic diagram of a hot cathode X-ray tube

The negatively charged cathode is a heated filament and the positively charged anode is a flat disc made of a suitable target metal (for example molybdenum) depending on the energy and wavelength of X-ray desired. The machine passes current through the filament, heating it up. The heat sputters electrons off of the filament surface and they are accelerated towards the positively charged anode at high speeds using high voltages. If the electrons bombard the tungsten plate with sufficient energies they are able to eject electrons from inner shells of the atoms of the metal target. Electrons from higher orbitals fall into these vacancies emitting X-rays with defined frequencies associated with the difference between the atomic energy levels of the target atoms [27].

In energy diagrams like the one depicted in Figure 8, there are allowable electron transitions, however only specific transitions produce characteristic X-rays. Transitions between outer shell electrons may result in optical photons and are referred to as optical transitions (hv of the order of a few eV); transitions between inner shells of high atomic number elements can result in the production of X-rays and are referred to as X-ray transitions (hv of the order of 10 to 100 keV).

In general the following conventions are used:

1. Transitions to the K shell are referred to as the K lines, to the L shell as L lines, to the M shell as M lines, etc.
2. Transitions from the nearest neighbour shell are designated as α transitions, from the second nearest neighbour shell β transitions, etc.
3. Transitions from one shell to another do not all have the same energy because of the fine structure (sub-shells) in the shell levels. The highest energy transition between two shells is usually designated with number 1, second highest with number 2, etc.
4. In Fig. 8 the transition $K_{\alpha 3}$ represents a forbidden transition (transitions from j = 0 to j = 0 are forbidden).
5. The transition $K_{\beta 1}$ represents an allowed transition from the M to the K shell (3p3/2 → 1s1/2 with Δ = 1 and Δj = 1).

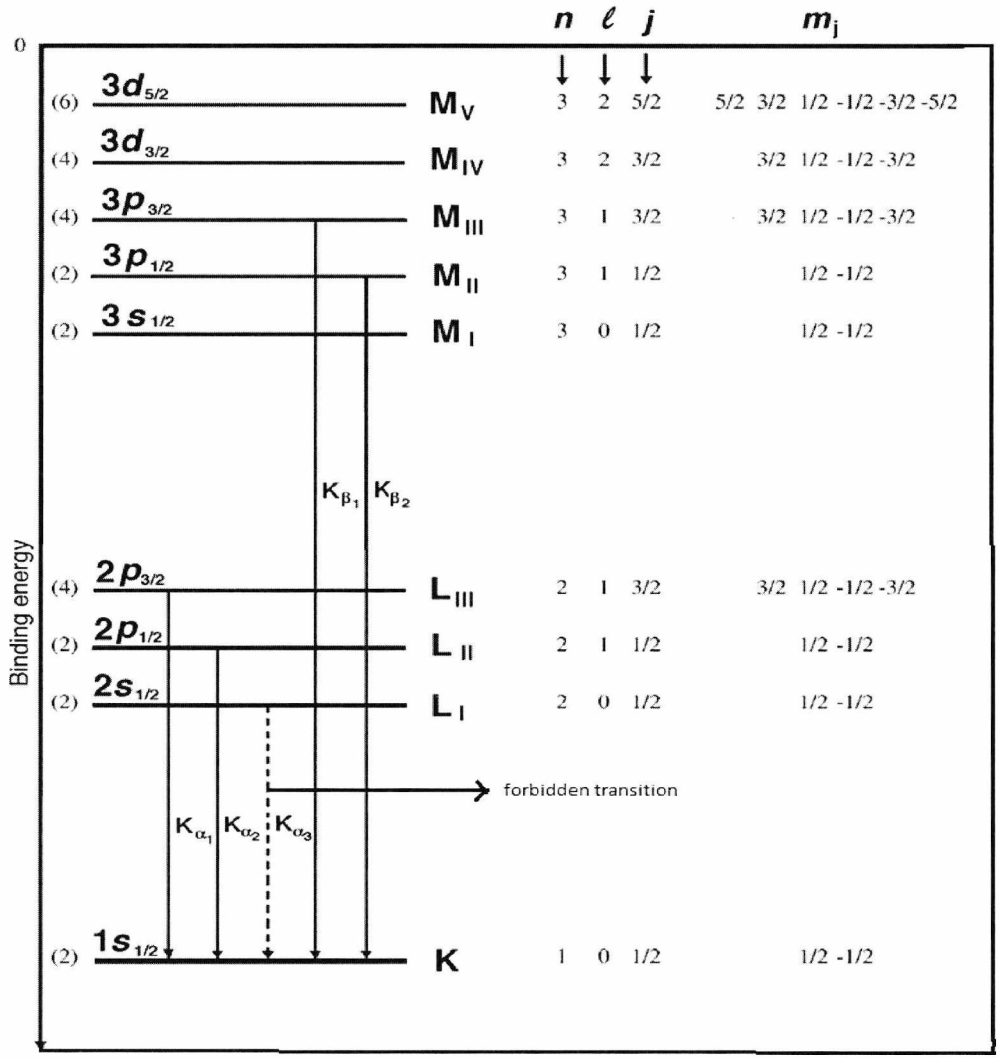

Figure 8: Electron energy levels for an atom

The typical output from an X-ray tube is shown in Figure 9. The highest intensity is in the K_α and K_β lines. In laboratory diffraction experiments it is usual to use filters to remove all but the K_α radiation so that the radiation is truly monochromatic. It is worth noting that there is a broad background radiation from an X-ray tube, the so called 'bremsstrahlung' or braking radiation. This arises from the slowing down of the electrons as they enter the metal cathode. It is possible to use monochromators to tune these X-rays however as can be seen in the figure the intensity is extremely weak.

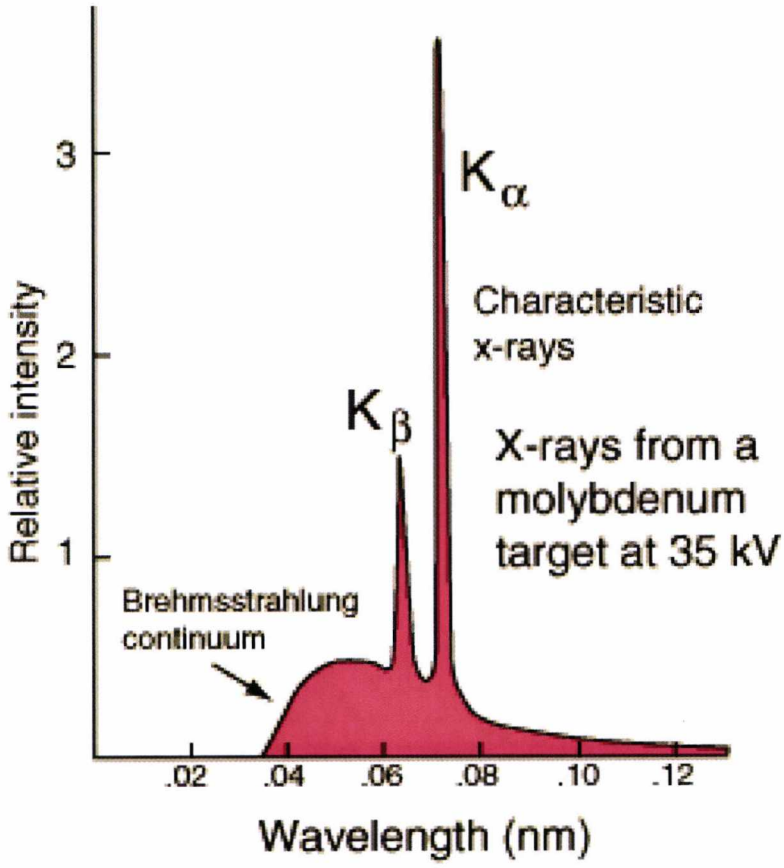

Figure 9: Typical X-ray spectrum from a Mo X-ray tube

II.1.2 Synchrotron Radiation

Synchrotron radiation refers to electromagnetic radiation emitted by charged particles travelling at relativistic velocities following a curved trajectory in free space under the influence of a magnetic field. The phenomenon was first observed in 1947 in synchrotrons (hence the term synchrotron radiation); accelerators that accelerate charged particles in circular orbits to very high relativistic energies. Since the effect occurs under the influence of a magnetic field that keeps the particles in a circular trajectory so they will typically be generated in a storage ring. The advantages of synchrotron radiation are that the beams of radiation produced are very intense, typically a billion times more intense than a laboratory X-ray tube, and the light is 'white', ranging from the microwave to the hard X-ray region. Thus the light can be monochromated and experiments are fast. Up to 1980 synchrotron radiation was produced only when the synchrotron was not being employed in nuclear physics experiments. In 1980 the Daresbury synchrotron was opened as the first machine dedicated to the production of radiation and was termed a second generation light source. There are now many dedicated synchrotrons which are larger, run at higher energies and electron currents (meaning more intense light) and these are termed third generation sources. Examples of these facilities are the European Synchrotron Facility (ESRF) at Grenoble, the Advanced Photon Source in the US and Spring 8 in Japan. In the last three years new facilities have opened; the Diamond Light Source in the UK and Soleil in France.

II.1.3 X-ray Absorption Spectroscopy (XAS)

X-rays have wavelengths of between 0.03 and 1 Å which also happens to be of the same order of magnitude as inter-atomic distances. They have energies of between 1 and 500 keV which also happens to correspond to binding energies of the most tightly bound electrons in atoms. These two properties make X-rays a powerful diagnostic tool when it comes to studying chemical speciation of samples.

An X-ray is absorbed by most materials, when absorbed by an atom the energy is used to promote a core-level electron (K, L, or M shell) out of the atom into the continuum.

The atom is left in an excited state with an empty electronic level referred to as core hole. The electron ejected from the atom is called the photo electron [27]. This type of absorption is called the *photo-electric effect*. The excited core hole will relax eventually to a ground state of the atom. A higher level core electron can then drop into this empty hole which results in a fluorescent X-ray (X-ray with energy equal to the difference between the core levels involved) or Auger electron being emitted (electron from another core level is promoted). The energy of the X-ray must be sufficient to excite the core electron into the continuum.

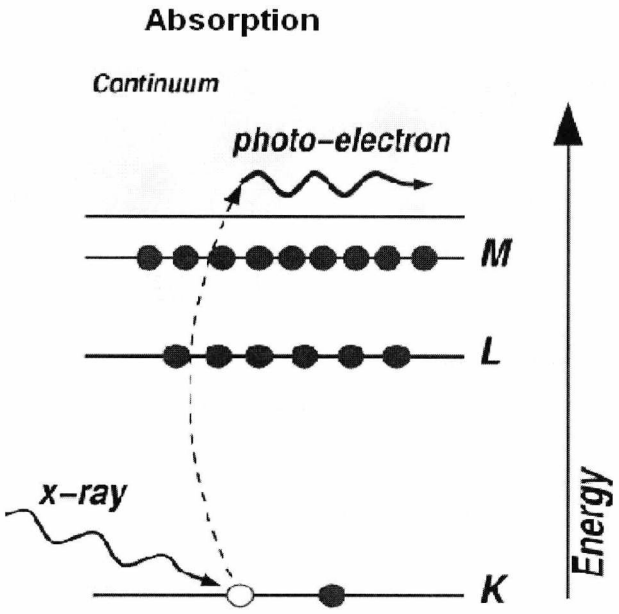

Figure.10: Schematic showing the production of a photoelectron

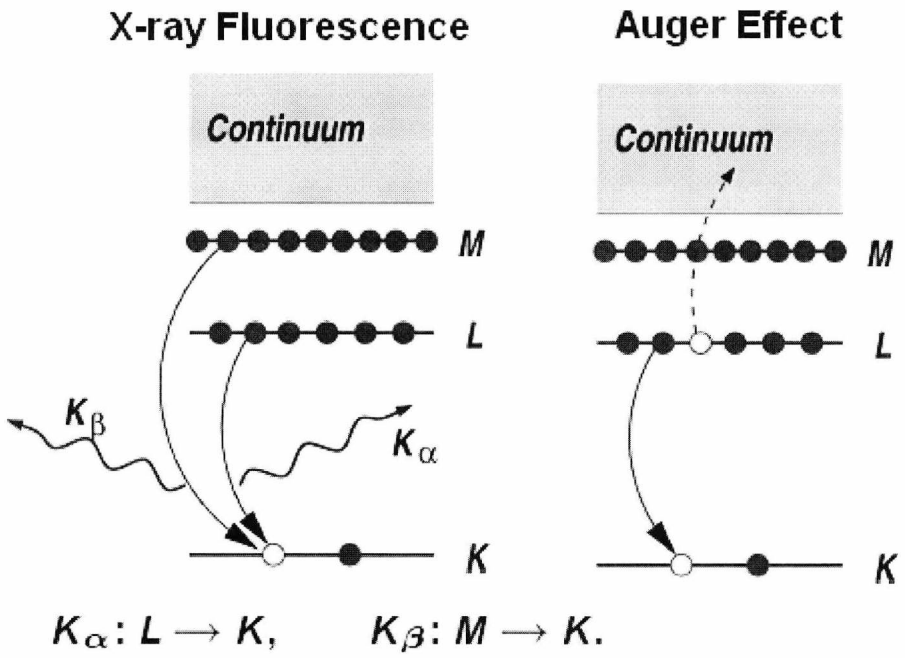

Figure 11: Schematic detailing X-ray fluorescence and the Auger effect.

II.1.4 X-ray Absorption Fine Structure (XAFS)

XAFS is a spectroscopic technique that uses X-rays to probe the physical and chemical structure of matter at an atomic scale. It can provide the local atomic coordination and the oxidation state of the sample under investigation. The X-rays used in XAFS experiments must be tuneable. The earliest experiments used the bremsstrahlung from X-ray tubes; however the low intensity meant that data collection times were extremely long. In modern experiments a synchrotron source is typically used. XAFS is element-specific; X-rays of energies at and above the binding energy of a particular core electronic level of a particular atomic species can be chosen. Because all but the lightest elements have core-level binding energies in the X-ray regime, nearly all elements can be studied with XAFS although difficulties are sometimes encountered when studying lighter elements ($Z < 15$). Unlike X-ray diffraction, XAFS works quite well with amorphous samples and even liquid samples. It also requires only a minimum amount of sample (typically a few mg) and works quite well at low concentrations of the sample under investigation.

In XAFS, the X-ray absorption coefficient μ is modulated at energies near and above an X-ray absorption edge (the energy just sufficient to excite a core electron into the continuum). The absorption coefficient is defined in the usual manner in spectroscopic applications by the Beer-Lambert law, i.e.

$$I_t = I_0 e^{-\mu t}$$

Where I_t is the intensity of the X-ray transmitted through the sample, I_0 is the intensity of the incident X-ray and t is the thickness of the sample.

The absorption coefficient depends strongly on the atomic number, the energy, density of the material and the atomic mass

$$\mu \approx \frac{\rho Z^4}{AE^3}$$

Here Z is the atomic number, E is the X-ray energy, ρ is the density of the material and A is the atomic mass

When an X-ray photon interacts with the sample, the sample begins to absorb the X-ray and the energy is used to produce a photoelectron. When the energy gets close enough to the binding energy of the core electron (1s, 2s... etc), the absorbance shoots up and the energy absorbed is used to eject the core electron (this electron is called a photoelectron). This point is called the *absorption edge*.

This photoelectron will be ejected with energy equal to energy of the incoming photon less its binding energy, when in the core.

This photoelectron will interact with the surrounding atoms. The surrounding atoms can backscatter the photoelectron wave. These backscattered waves can interfere with the forward wave (photoelectron wave) to produce peaks or troughs, which can be seen as a simple picture or as oscillations in an EXAFS plot. The intensity of the oscillations diminishes with increasing photon energy and is typically about one tenth of the magnitude of the step at the edge. A typical XAFS spectrum is shown in Figure 12.

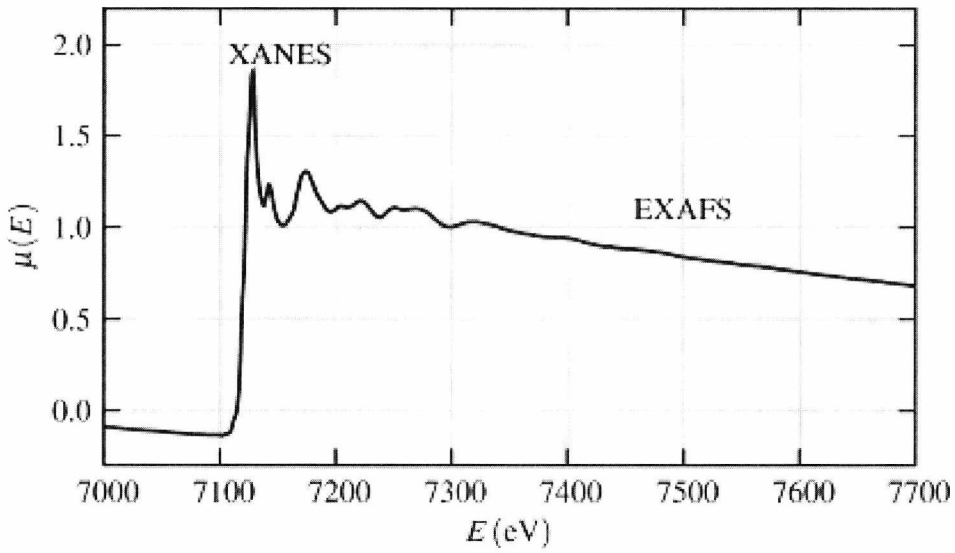

Figure 12: A typical XAFS spectrum taken for an iron foil.

XAFS is broken into two main parts:

X-ray Absorption Near-Edge Spectroscopy **(XANES)** which provides information on:

- Oxidation state
- Unfilled orbitals, symmetry, etc

Extended X-ray Absorption Fine Structure **(EXAFS)** which provides information on:

- The type of atoms surrounding the central absorber atom (the atomic number Z ± 3)
- The number of atoms surrounding the central atom - ± 20%
- The distance between the absorbing atom and scattering atom (± 0.02Å,)
- Some geometrical information via multiple scattering
- The thermal variation in the absorber-scatterer distance (this adds a damping factor to the EXAFS oscillations)
- The energy of the photoelectron - the scattering is a function of the electron energy, and hence of the wave-vector k, which is proportional to the square root of the electron energy [28]

Each scattering atom contributes a damped sine wave to the EXAFS spectrum. The total EXAFS spectrum is the sum of the contributions from all of the atoms surrounding the absorber atom. In highly ordered or crystalline systems, this may include scattering atoms up to 6 Å from the absorber.
The physics of EXAFS is complex; however the oscillations (the normalised EXAFS. $\chi(k)$) can be approximated to the following equation

$$\chi(k) = \sum_j \frac{N_j}{k R_j^2} |f_j(\pi)| \exp(-2\sigma_j^2 k^2) \exp(-2R_j/\lambda) \sin(2kR_j + \psi_j + 2\delta)$$

Here N_j is the number of atoms (all of the same type) in shell j with backscattering factor $f_j(\pi)$ at a distance R_j from the central atom. The other terms in the equation are a Debye-Waller like factor σ_j expressing the mean square variation in R_j, the phase factors δ and ψ_j of the photoelectron wave which depend on the central and scattering atom, and λ the mean free path of the photoelectron. The Fourier transform of $k.\chi(k)$ with respect to $sin(2kR)$ or $exp(-2ikR)$ yields a partial radial distribution function in real space with peak areas proportional to N_j. If the phase factors are known, either from theoretical calculations or model compounds (i.e. fitted from the EXAFS of chemically similar compounds to that under investigation but with known R_j and N_j), then the radial distances can be determined, typically out to 5Å from the target atom. The uncertainty in R_j that can be achieved with EXAFS is about +/- 0.01 Å. The determination of N_j is usually less accurate, about +/- 20%, as it is strongly coupled to the Debye-Waller factor. $f_j(\pi)$ does not vary strongly with atomic number and the identification of the type of atoms in the shells is limited to differentiation between rows of the Periodic Table. The advantages of EXAFS over diffraction methods are that it does not depend on long range order, hence it can be used to study local environments in both crystalline and amorphous solids, and liquids, and it is atom specific and can be sensitive to very low concentrations of the target atom. However, there is one note of caution in that the commonly used XAS is an *average technique*, in that it probes the local environment of all the target atoms in the sample. Thus if the target atom is in more than one local environment the resulting spectrum will be an appropriately weighted average of all the environments.

II.1.5 EXAFS Data Processing

Several packages are available to analyse EXAFS data, which involves fitting to the EXAFS equation in the last section. The fitting uses least-squares routines to fit the spectrum to a structural model, with radial distances, numbers of neighbouring atoms and Debye-Waller factors as variables. Data in this thesis will be processed in the conventional manner using the Daresbury suite of EXAFS programs; EXCALIB, EXBACK and EXCURV98. Phase shifts will be derived from *ab initio* calculations within EXCURV98. This code also includes routines to treat multiple scattering effects in highly symmetric structures. For each spectrum a theoretical fit is obtained by adding shells of atoms around the central excited atom and least-squares iterating the Fermi energy, E_o, the radial distances, RD, and the Debye-Waller type factors, A ($=2\sigma^2$).

This latter factor will contain contributions from both thermal disorder and static variations in RD. The program also allows iteration of the coordination number, CN, The quality of the fit is measured by an R-factor and the errors in RD are approx. ± 0.02 Å and approx. ±20% in A and CN [29].

The steps in the EXAFS fitting using the Daresbury programmes are illustrated in Figure 13.

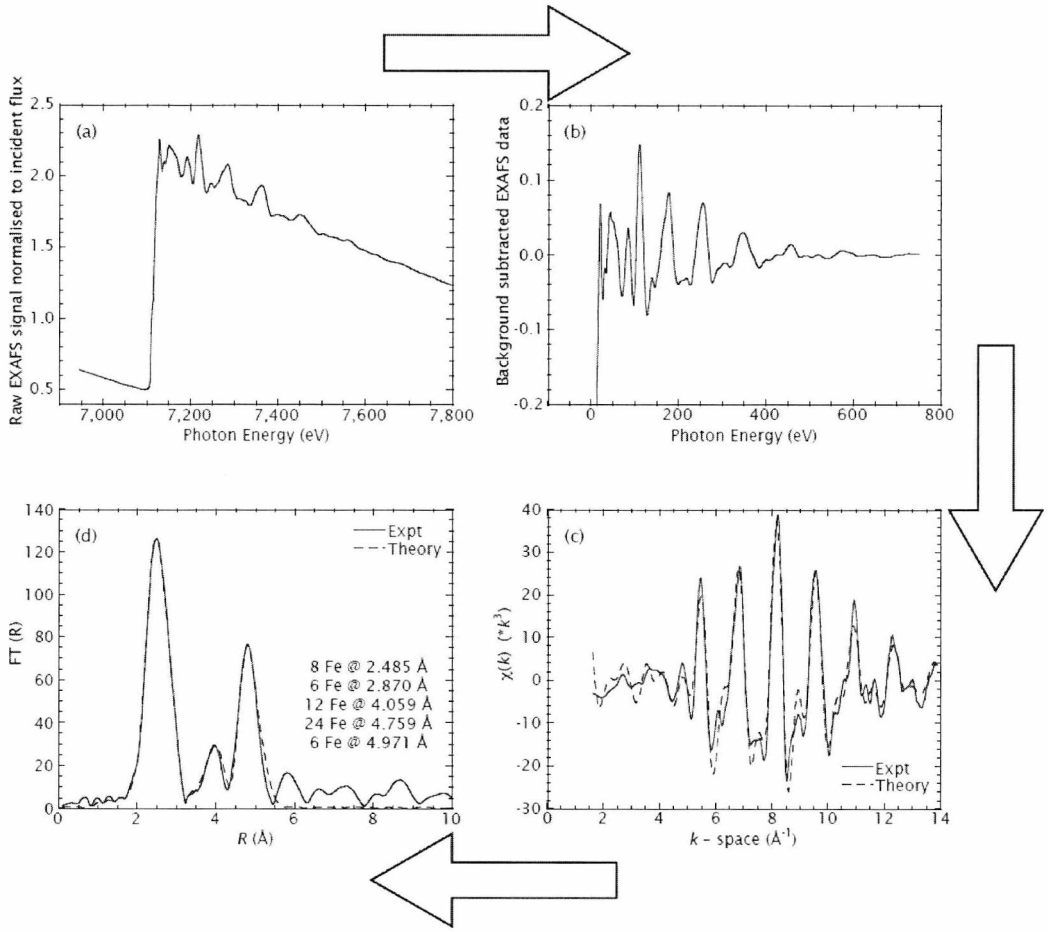

Figure 13: Fe K-edge XAS spectrum of an iron foil. (a) The raw absorption spectrum, (b) the background subtracted spectrum [EXCALIB], (c) the normalised EXAFS spectrum, $\chi(k)$ which has been k^3 weighted to emphasise the oscillations at high k [EXBACK or EXSPLINE], (d) the corresponding Fourier transform corrected with the phase shift of the first shell. The experimental data is the solid line and the best fit is the dotted line [EXCURV98]. The best fit parameters for the EXAFS are given on (d).

II.2 X-ray Absorption Spectroscopy in archaeological science

X-ray absorption spectroscopy (XAS) has been shown to be highly beneficial in the study of archaeological materials in recent times. X-ray methods such as X-ray diffraction (XRD) used to determine crystal structure, and X-ray fluorescence (XRF) used to determine elemental composition are now widely used in archaeological and cultural heritage studies. These are well used and documented analytical techniques easily carried out in laboratories. Equipment used to carry out these analyses are being made portable to increase and improve their use in the field of cultural heritage [30, 31]. This is because most of the artefacts either cannot be moved easily or their value and importance often prohibit them being moved. There is now a drive to increase the spatial resolution of the X-ray probe by reducing the spot size to the order of tens of microns [32, 33] and this is being increasingly pursued at synchrotron sources [34- 39]. The advantage of synchrotron sources is the significantly higher brightness of the radiation beam resulting in more efficient focussing of the X-ray beam into small focal sizes [40].
Archaeological and cultural heritage materials are not always highly crystalline but amorphous. There will quite often also be only small amounts available for analysis and XAS can cope very well with such constraints. XAFS X-ray absorption fine structure has been used in recent times in the study of wooden marine archaeological artefacts and the use of chemical remediation processes in the preservation of the large marine timber artefacts. In studying such artefacts there is normally the need for preservation; XAFS offers non destructive options as there is no need for a vacuum at the experimental station where the sample is analysed. XAFS also have low detection limits, afford high lateral resolution and possesses high chemical sensitivity. The afore mentioned characteristics of XAFS make it highly desirable in the study of rare, precious, heterogeneous and complex materials like marine archaeological wooden artefacts [41].

X-ray absorption near edge spectroscopy (XANES) has been used in the analysis of Fe valency in iron gall inks. Iron gall ink is of great importance in the history of western civilization as a great many manuscripts from Bach scores to those written by Galileo Galilei were penned using iron gall ink.

The ink however causes severe corrosion to these manuscripts and many have been rendered illegible or seriously damaged. The two main contributory factors are acid hydrolysis and oxidation which are characterised by ferrous ions [42, 43]. The process is by the so called Fenton reaction which produces oxyradicals. The production of these oxyradicals is catalysed by the presence and accessibility of Fe^{2+} ions as well as the pH of the environment [44].

$$Fe^{2+} + O_2 + H^+ \rightarrow Fe^{3+} + HOO\bullet$$
$$Fe^{3+} + HOO\bullet + H^+ \rightarrow H_2O_2$$
$$Fe^{2+} + H_2O_2 \rightarrow Fe^{3+} + OH^- + OH\bullet$$
$$OH\bullet + \text{Cellulose} \rightarrow \text{depolymerisation}$$

To determine the risk of further oxidation of cellulose in these manuscripts and to preserve them, the Fe^{2+}/Fe^{3+} and the concentration of Fe^{2+} in these manuscripts must be determined along with the effective removal and/or stabilisation of Fe^{2+} initiated.

There are a number of methods employed in the determination of total Fe^{2+} content and Fe^{2+}/Fe^{3+} but they are all hampered by considerable limitations. XRF and particle induced X-ray emission (PIXE) can offer insight into the spatial distribution of Fe ions in the paper if a micro beam and the scanning technique is used [45-51]. Whilst XRF can provide quantitative information about the Fe ions present; it offers no information about the oxidation states. Mossbauer spectroscopy has been used in the investigation of the Fe^{2+}/Fe^{3+} but its usefulness is limited due to the difficulties in gaining a good signal from the minute amount of iron gall ink present in sample analysed [52-55].

XANES overcomes these limitations by providing the oxidation states of Fe ions present by looking at the energy shifts of the absorption edge and/or at the pre-edge feature; the Fe^{2+}/Fe^{3+} can be determined using linear combinations. The environment of the cation; that is, the atoms surrounding it can be determined from the K-edge profile. Different environments of the cation, especially those with different site symmetries have different K-edge profiles [56-58]. At bright synchrotron sources this technique can be applied to samples with low iron content and in combination with microfocusing, information about the 2-D distribution of Fe^{2+} on parts of the manuscript can

be determined [59-61]. Arcon *et al* [62] used XANES to investigate the concentration of iron and the Fe^{2+} / Fe^{3+} ratio in ancient manuscripts written with iron gall ink. They found that the fraction of Fe^{2+} could be deduced from energy shift of the absorption edge or pre-edge features. They also found a shift of about 4.5 eV between the spectra of the two and three valent iron species which is agreement with previous observations [62]. They observed that shifts in Fe^{3+} edge position are found not only between tetrahedral and octahedral coordinated of Fe^{3+} cations, but also between octahedrally coordinated Fe^{3+} cations with different local coordination geometries in the nearest coordination shells. Tetrahedrally coordinated Fe^{3+} cations in $FePO_4$, lacking an inversion centre, exhibited the characteristic isolated pre-edge peak, which is due to the electron transition from 1s to an unoccupied tetrahedral state $3t_2$, and a shoulder on the edge slope resulting from to the electron transition; $1s \rightarrow 4t_2$ [56-57]. On the other hand, octahedrally coordinated Fe^{3+} sites in $FePO_4 \cdot 2H_2O$, FeOOH, Fe_2O_3, and $Fe_2(SO_4)_3 5H_2O$, that possess an inversion centre, exhibit a different pre-edge feature (two weak resonances), assigned to transitions of 1s electron into anti-bonding orbitals with octahedral symmetry (see Figure 14)

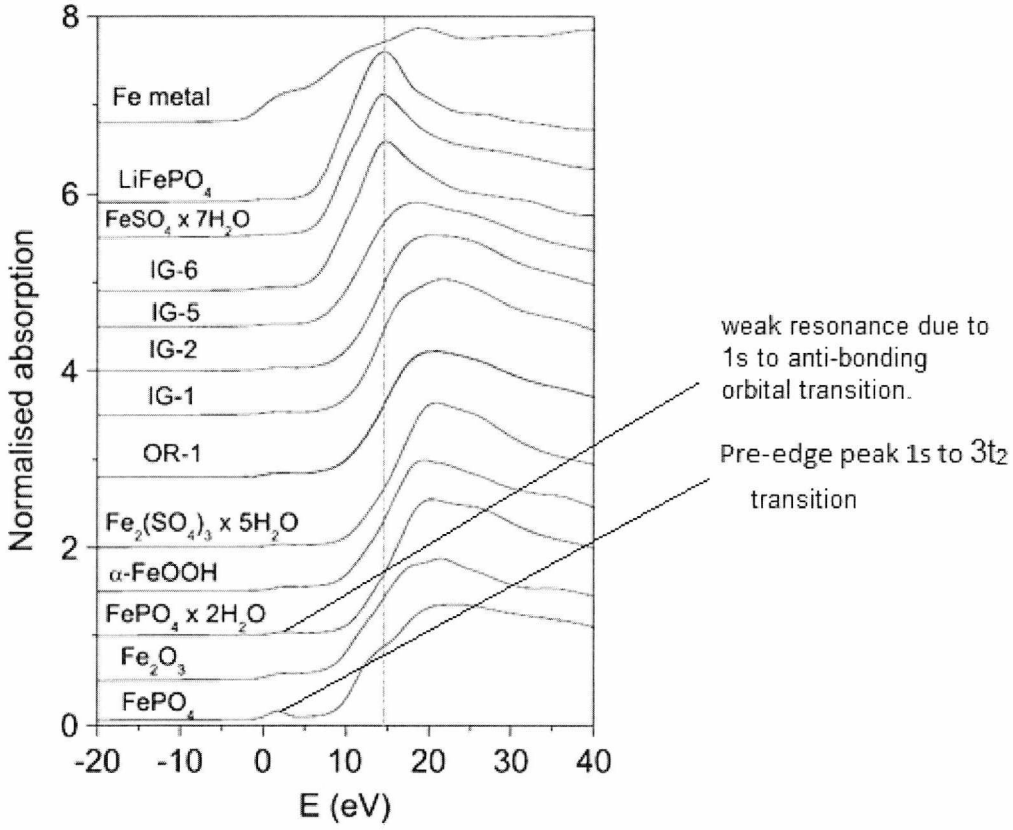

Figure 14: Fe K-edge XANES spectra of representative historic and model Fe gall inks [62]

Micro-XAFS has also been used in the study of oxidation states exhibited by different coloured glazes originating from the early Islamic world. Smith *et al* used fluorescence micro-XAFS able to penetrate the predominantly aluminium and silicon surface layers of these ancient glass (to about 100 Å – 200 Å thick) to probe the glasses beneath [63]. They carried out this investigation to ascertain why some particular pieces of ancient pottery or glass did not reach a metallic shine finish although the potter may have intended for it to possess a metallic patina. This could be a result of full reduction of to copper metal not being achieved. They recorded Cu K-edge EXAFS and found that where there is distinctively good metallic glaze, full reduction to the metal had taken place. The fit of the experimental data to pure copper foil was very good, showing that not only was good reduction obtained in the firing process by the original artist, but the glaze was also able to hold the copper effectively preventing further oxidation through the years.

The varieties of colours observed in glasses are caused by incorporating different metal ions in them [64]. They are usually elements belonging to the transition rows of the Periodic Table. They absorb characteristic frequencies of visible region and the energy used in d-d electronic transitions. Similarly, iron is a key element to understanding the colour of various types of pottery and this kind of information is significant in elucidating ancient manufacturing technique of glass wares and pottery.

Nakai *et al* [65] applied fluorescence XAFS technique successfully in the archaeological study of old glass in the ceramic shards excavated from an archaeological site in Turkey to find elements used to provide their distinct colours and also to characterize the chemical states of iron present in the samples [65]. The samples used were mosaic glasses from Dome of Hagia Sophia built in 537 in Istanbul, Turkey and ceramic shards from Kaman Kalelioyiik, Turkey.

X-ray absorption spectra were measured at Photon Factory (PF) in the National Institute of High Energy Physics, Tsukuba, Japan with a Si(ll1) double crystal monochromator. They carried out a two dimensional chemical state analysis of iron in the ceramic shards at BL-4A using Si(Li) S.S.D. as a detector.

EXAFS data were obtained in the fluorescence mode [66]. The edge energy was defined by a half maximum value of the white line peak of each XANES spectrum. XAFS measurements were carried out at the Fe and Cu K-edges, K-edge XANES were compared with reference samples and EXAFS oscillations obtained from the Fourier transforms of k^3.(k).

The following observations were made:

- Oxidation state of copper in the mosaic glass is monovalent while it is divalent in the Egyptian glass.
- The Cu^+ is d^{10} ion and is not responsible for the green colour which is the colour of divalent copper. Therefore, the origin of the green colour in the mosaic glass could be ascribed to another ion.
- Co^{2+} was responsible for the blue colour of the mosaic glass and Egyptian glass.

XAS studies have also been highly beneficial in the preservation of the Swedish war ship *Vasa.* Built between 1626 and 1628, it was Gustav Adolf's (king of Sweden) effort in increasing his status as major figure in international politics during the Thirty Years War and cement Sweden's place as a major force in Europe. The ship sank on its maiden voyage on august 10^{th} 1628 1500m from the Stockholm harbour in full view of Swedish dignitaries.

It remained on the seabed preserved by silt and the anoxic conditions until it was raised in April 1961. It underwent PEG treatment for several years, gradual air drying and was finally displayed in a museum in Stockholm.

In the year 2000, after a hot summer and a record number of visitors to the *Vasa,* the Relative Humidity (RH) of the museum increased to around 65%. Conservators shortly began to notice yellow and white precipitates which turned out to be acidic. This was later termed the *sulfur problem* (explained earlier).

In an endeavour to understand the mechanisms for the formation of these acidic precipitates, Sandstrom *et al* [66] studied samples taken from the *Vasa* using XAS to determine the sulfur and iron speciation in the *Vasa* timbers.

The accumulation and transformation of reduced sulfur compounds like hydrogen sulfide in organic matter play an important role in the natural sulfur cycle, in particular of the organosulfur compounds in wet partially decomposed (humic) matter. This is the case also in anoxic marine sediments of low iron content, which eventually may end up in fossil fuels such as coal and oil.

When corrosion products of iron are present in sufficient amount, competing reactions with the hydrogen sulfide will also form particles of iron(II) sulfides, e.g. pyrite and pyrrhotite.[8, 9, 12, 66].

Even though sulfur is ubiquitous and biochemically essential, research into sulfur chemistry in natural or environmental samples had only been partially investigated due to the paucity in analytical tools for *in situ* analyses and speciation; that is until the development and applications of spectroscopic methods, in particular sulfur spectroscopy at synchrotron facilities. Sandstrom *et* al used sulfur X-ray absorption spectroscopic methods to decipher the sulfur speciation in wood samples from archaeological wooden artefacts [66].

They had previously used high resolution X-ray fluorescence line scans complemented with elemental analyses and multi-element X-ray photoelectron spectroscopy to study how the total sulfur and iron concentrations vary along cores taken from the *Vasa* [9], *The Mary Rose* [8] and the *Bremen Cog* [9].

Their studies revealed that for *the Mary Rose* the sulfur concentration along all cores fluctuates around 1 mass% S, representing a total of about two tons of sulfur in the approximately 280 tons of oak wood. In the *Vasa's* hull which comprises of more than 1000 tons of oak timbers, the sulfur concentration was found to be normally highest in the first cm or so of the surface layers with a similar total amount of 2 tons S, as in the *Mary Rose* [3, 8, 13]

However, low concentrations were found for the wreck of the *Bremen Cog*, which was preserved in river water. This is because sulfur compounds are not as readily available in rivers as they are in sea water.

Speciation of the sulfur compounds in the core samples from these ships were made possible by means of sulfur K-edge X-ray absorption near edge structure (XANES) spectra measured at the dedicated SSRL beamline 6-2, operated in fluorescence mode and at atmospheric pressure (1 atm He) [2, 8, 13, 40, 66]. Segments of the wooden cores, a few mm in length were filed in inert atmosphere to fine particles, mounted on sulfur-free tape and covered by 4 mm sulfur-free polypropylene film (UltraleneE) [66]. The sensitivity at the SSRL beamline 6-2 was sufficiently high to determine the main sulfur species in a wood sample with a total sulfur concentration of about 300 ppm without radiation damage.

The principle in such experiments is to scan the energy of the incident X-rays over the K-edge. Absorption features are observed in the spectra; this includes pre-edge features and absorption edge features characterised by a huge and sharp rise in the absorption spectra.

The presence of pre-edge peaks or features is due to X-ray induced transitions of S(1s) core electrons to unoccupied valence states localised around the sulfur atom with some sulfur 3p contribution in the molecular valence shell [20,21] The lowest transition energy depends on the formal oxidation number; a higher effective nuclear charge increases the binding energy of the S(1s) orbital, resulting in a large shift of about 13 eV from sulfides(-2) to sulfate(+6) [8, 9, 66]. The unoccupied molecular valence

orbitals are more shielded and less affected, but are also influenced by the covalency of the bonds to the sulfur atom and the coordination geometry, which contribute to the transition energies and intensities. The intensity of the pre-edge peak largely depends on the contribution from the sulfur 1s → 3p dipole allowed transitions, i.e. the overlap integral between the corresponding lowest unoccupied molecular orbitals with some sulfur 3p character. With increasing effective charge on the sulfur atom the overlap integral, and thus the intensity, increases because the 3p orbitals contract more than the 1s [9, 66]

A series of XANES were collected by Sandstrom *et al* [9] on segments of a 20mm core sample from the hull of the *Mary Rose* undergoing PEG treatment; the spectra are in Figure 15.

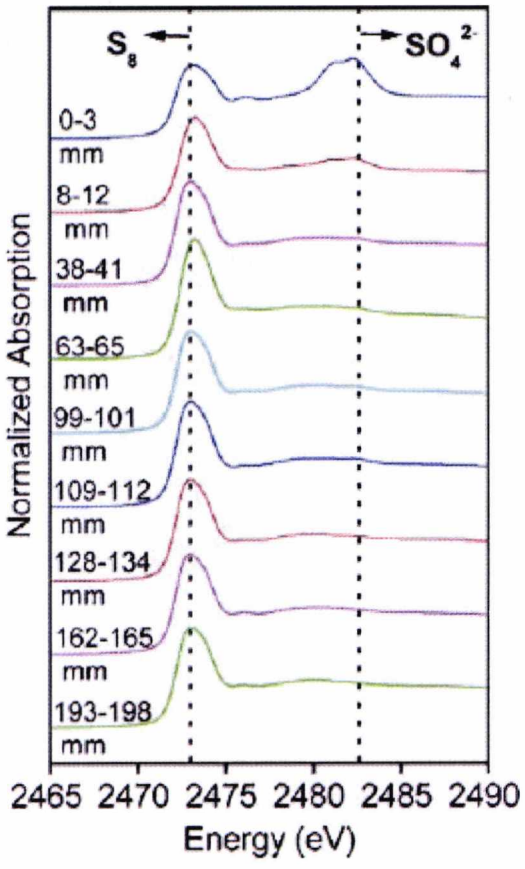

Figure 15: The *Mary Rose*: Normalised sulfur K-edge XANES spectra of powdered core segments from PEG treated hull rider; core 3 (black-brown oak) vs depth from the surface [9].

The main absorption peak corresponds to reduced sulfur in several components. The most common could be characterised by standard spectra of disulfides R–SS–R, thiols R–SH, and elemental orthorhombic sulfur S_8. Oxidised sulfur(VI) compounds in significant amount occur only at the surface. Occasionally, the reduced sulfur peak in some cores also indicates pyrite in varying amount consistent with its occurrence in particles [9].

II.3 X-ray Diffraction

X-rays are part of the electromagnetic spectrum, they occur between gamma rays and ultraviolet and they have wavelengths of about 10^{-10} metres. X-ray diffraction can be used to characterise a material and also determine the structure of crystalline materials. Each material has a distinctive X-ray powder diffraction pattern which can be used for its identification.

The atoms that make up a crystal lattice are arranged in a regular 3-dimensional pattern. When X-rays interact with a regular structure whose repeat distance is about the same as the wavelength of the X-ray, diffraction can occur. In 1912, W.L. Bragg recognized a predictable relationship among factors below.

1. The distance between similar atomic planes in a mineral (the inter-atomic spacing) called the d-spacing and measured in Angstroms.
2. The angle of diffraction called the theta angle and measured in degrees. For practical reasons we measure an angle twice that of the theta angle which is referred to as '2-theta'.
3. The wavelength of the incident X-radiation, symbolized by the Greek letter lambda.

He used this relationship to formulate Bragg's law. For X-ray diffraction to occur, Bragg's law has to be satisfied, i.e.

$$n\lambda = 2d\sin\theta$$

Here n is an integer (1,2,3,4.....etc), λ is the wavelength in Ångstroms, d is the inter-atomic spacing in Ångstroms and θ is the diffraction angle in degrees.

A monochromatic beam of wavelength λ is generated from an X-ray source (and a monochromator) and focused on the sample at angle theta. The rays

in the beam are diffracted by the sample and the diffracted rays are picked up by a monitor [68]. The set-up is shown in Figure 16.

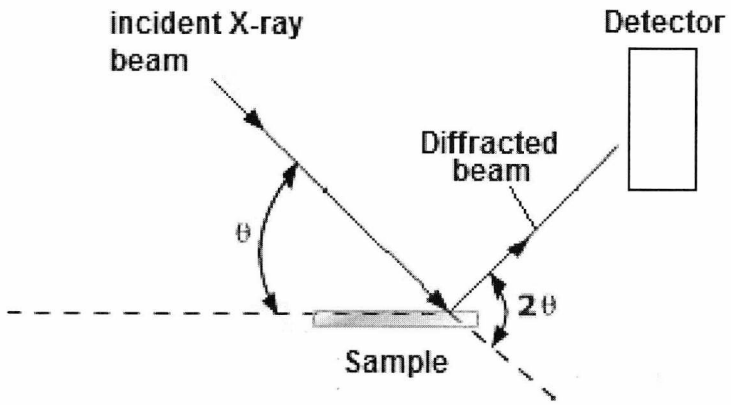

Figure 16: Typical set-up for an X-ray diffraction experiment.

Plotting the angular positions (2θ) and intensities (counts) of the resultant diffracted peaks of radiation produces a pattern, which is characteristic of the sample. The example of NaCl is given in Figure 17.

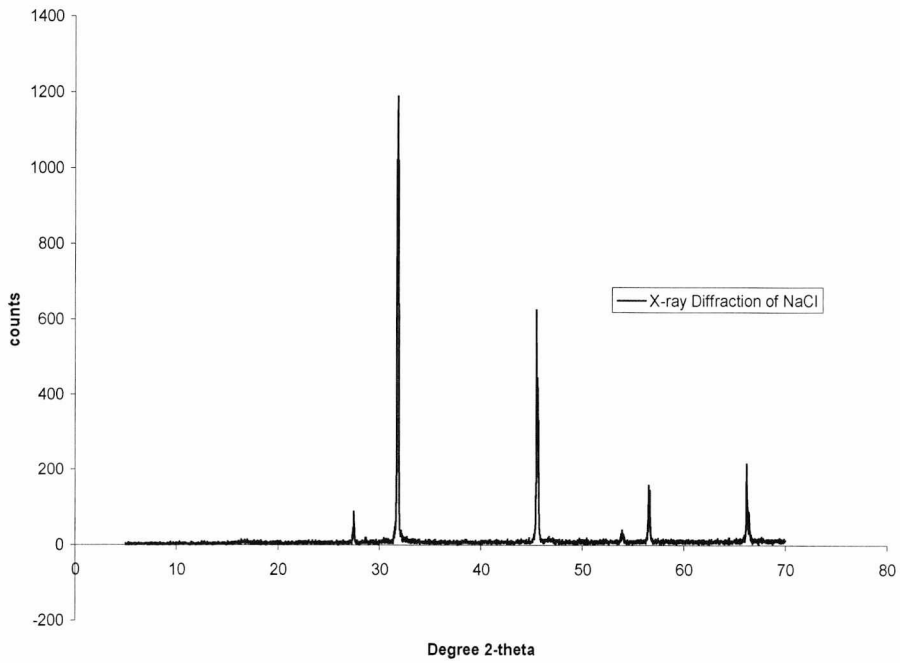

Figure 17: A typical diffraction pattern (intensity versus 2θ): A Berko.

X-ray diffraction studies using synchrotron radiation sources have become popular in recent times. Not only are diffraction experiments carried out at synchrotron sources non destructive, but the high intensity, high collimation and small beam sizes offered by synchrotron radiation makes it possible for analyses to be carried out on small samples.

Young *et al* used high-energy X-ray diffraction measurements performed with a monochromatic 85 keV (λ = 0.015 nm) to study ancient Chinese bronzes [69]. A sample is shown in Figure 18.

The X-ray beam for diffraction had a cross-section with 20×200 μm^2 dimensions for the bronze vessel fragment and 200×200 μm^2 for the dagger-axe. Complete Debye–Scherrer diffraction cones from the crystalline phases present in the diffraction volumes were recorded using an on-line image plate. Additional calibration diffraction cones were produced from a paste composed of vacuum pump grease and pure ceria powder, which was contained in a plastic bag placed on the back surface of each object.

Software program Matlab was utilised in the creation of intensity versus *d*-spacing graphs and Jade was used for phase identification [69].

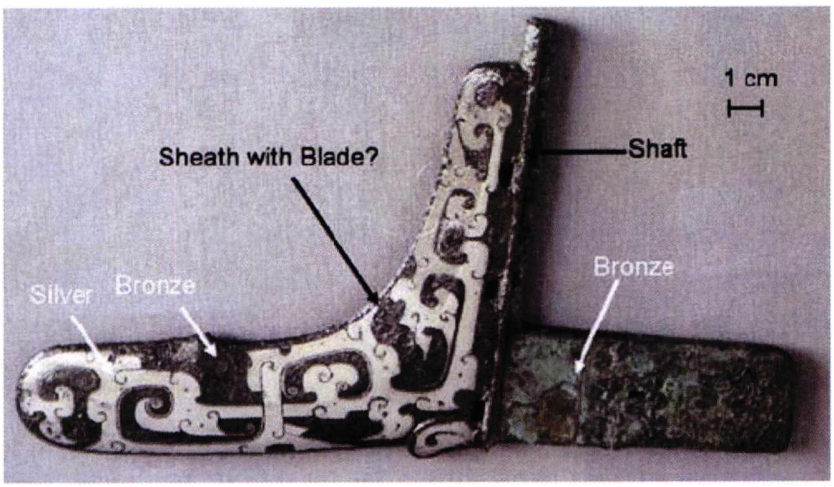

Figure 18: Bronze dagger-axe: Photo courtesy of The Art Institute of Chicago Conservation Laboratory [69].

Observations made from synchrotron X-ray radiography and diffraction provide strong indications that the bronze dagger-axe is a ceremonial object cast in a single block from bronze, and does not contain a bronze blade within a bronze sheath.

Synchrotron X-ray diffraction studies performed on a small fragment area where the metal core of the bronze vessel had been exposed by previous destructive sampling operations, was done with the goal of comparing results with those acquired by Gettens [70, 71] and also their own analytical campaign on excised samples from the same area, to assess the non-destructive effectiveness of the synchrotron technique.

They found the presence of strong peaks for cuprite (Cu_2O) and cassiterite (SnO_2) identified as major phases in the corrosion layer in agreement with findings by Gettens [70, 71]. Other spectra exhibited the presence of these two oxides, together with Cu and $Cu_{41}Sn_{11}$, which can be interpreted as a metallic core with significant amounts of corrosion products, also in agreement with the description by Gettens.

At the deepest positions (>~ 400 μm), the peaks from these corrosion products are very weak, but those from the three metallic phases from the original bronze alloy (Cu, $Cu_{41}Sn_{11}$ and Pb) are preeminent, indicating that the beam is mostly sampling un-corroded material.

High-energy synchrotron X-ray diffraction has also been employed in the study of a bronze fibula originating from the Syrian site of Tell Beydar (3rd millennium B.C.) [73] and more recently ancient brass astrolabes [74, 75].

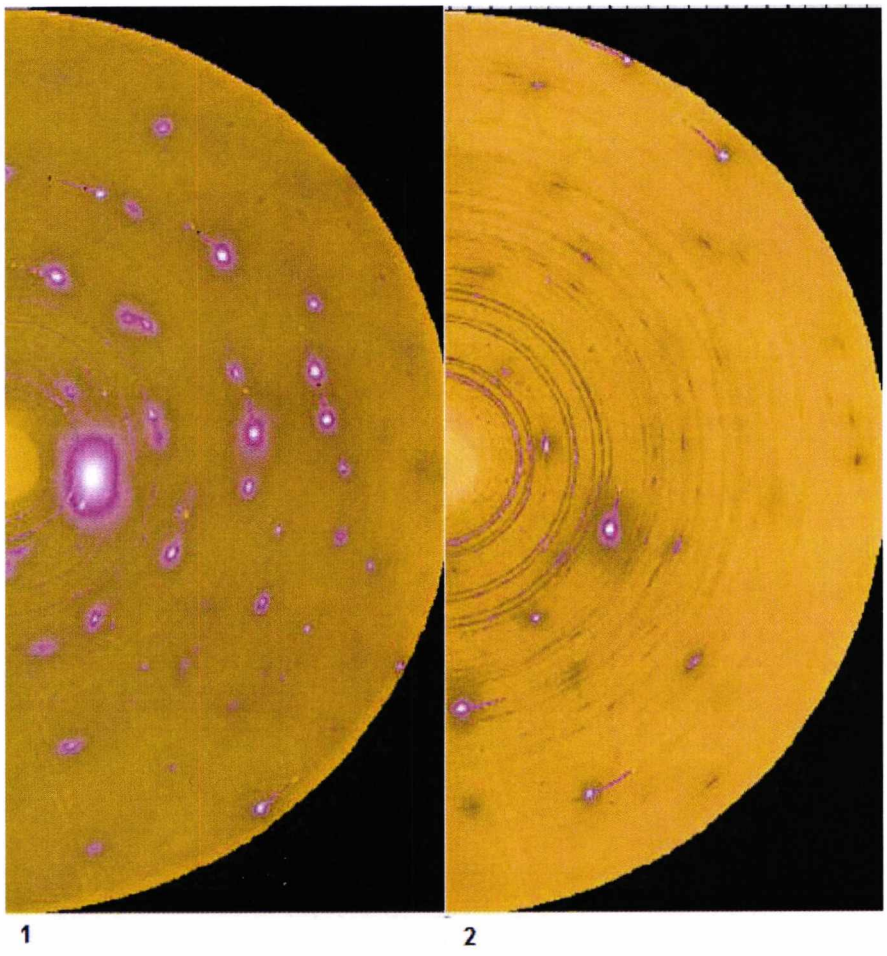

Figure 19: Synchrotron X-ray diffraction patterns collected consisting of (1) predominately bronze with a small amount of surface corrosion and no silver inlay and (2) a combination of bronze, corrosion layers, and silver inlay [69].

II.4 X-ray Fluorescence

The use of X-ray fluorescence (XRF) in the characterisation of archaeological materials is becoming more popular in recent years due to the development of micro-focus X-ray fluorescence. The use of this technique in the elemental characterisation of works of art has been well known for a while. This technique has been used to study artefacts like paintings by Van Gogh and timber samples from 16th century warships.

X-ray fluorescence spectroscopy is a fast and non destructive technique which provides qualitative and quantitative information of elements in samples being analysed [76-79] and meets a number of the criteria outlined by Lahanier *et al* for analytical methods suitable for the study of objects of

artistic, historic or archaeological importance [77]. They summarised that an ideal analytical technique for such samples would be:

- Non-destructive
- Fast
- Universal (that is a single instrument may be used to analyse samples of various shapes and dimensions with little or no sample pre-treatment)
- Versatile (allowing with the same technique, average compositional information to be gained along with local information of micro areas from heterogeneous materials)
- Sensitive
- Multi-elemental

In XRF experiments the sample under investigation is irradiated with X-rays with energies high enough to excite a K or L electron into a continuum; that is eject it from the target atom leaving behind a core hole (figure 11). An electron from a higher energy shell can fall and fill this empty shell emitting excess energy as fluorescence which can be detected and plotted as peaks.
There two types of K peaks; K_{α}, which is when an L electron falls into a vacant K orbital and K_{β} which is when an M electron fall into an empty K orbital. There are also L (an electron from the M or N shell "jumps in" to occupy the vacancy created by the excitation of an L electron) and M peaks (an electron from an N shell falls into a vacant M shell) which occur at lower energies and have lower intensities that K peaks. The energies of K, L and M peaks are characteristic of elements and can be used to identify the elements present in a sample being analysed. These transitions are shown in Figure 20.
The intensity of the peaks can also be used to determine the amount of these elements present thus providing qualitative as well as quantitative information.
Many XRF instruments can detect elements heavier than sodium with a few detecting elements as light as boron. This makes X-ray fluorescence spectrometry a useful tool in analysing inorganic materials, organic materials and metals [76]. A typical XRF plot, counts versus energy, is shown in Figure 21.

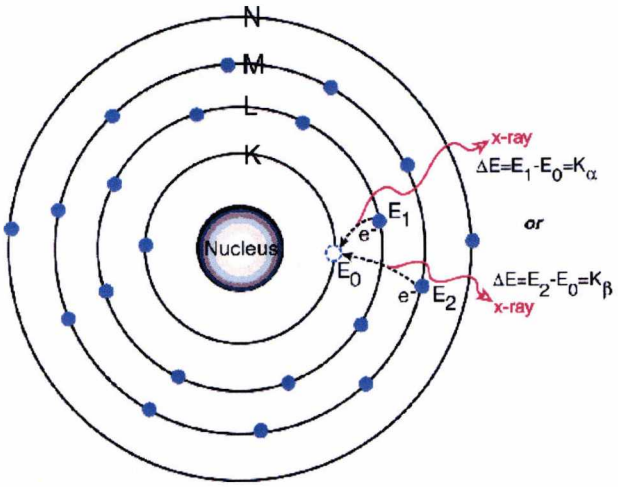

Figure 20: Energy level diagram of XRF transitions.

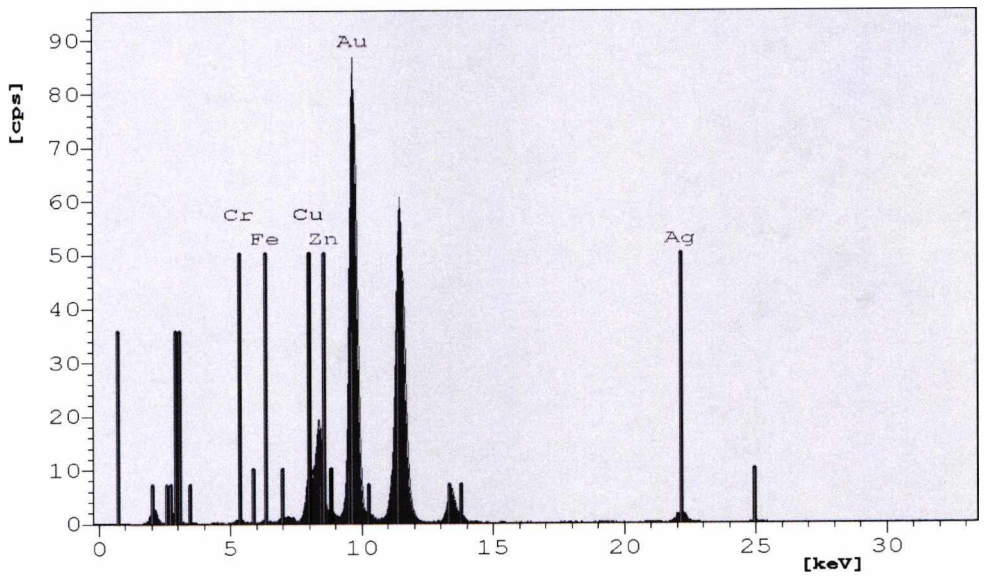

Figure 21: Plot of XRF analysis of gold coin from the *Mary Rose* ship; analyses carried out by author.

II.5 Micro-focus X-ray techniques

The use of conventional XRF and XAFS for quantitative and qualitative analysis of distinct features and chemical composition of small areas is difficult because the area irradiated is usually large and this makes detailed analysis challenging. This limitation can be surmounted by employing X-ray beams of small diameters. Synchrotron micro-focus X-rays with parts per million (ppm) detectability can be used for quantitative fingerprint analysis of materials in order to investigate chemical composition at cell level in archaeological wood, origins of artefacts and processes that change the surface composition of materials [78, 79].

The layout in outline of a typical microfocus spectroscopy beamline, in this case station I18 situated at the Diamond Light Source in the United Kingdom is shown in Figure 22 with a detailed schematic of experimental hatch set up shown in Figure 23.

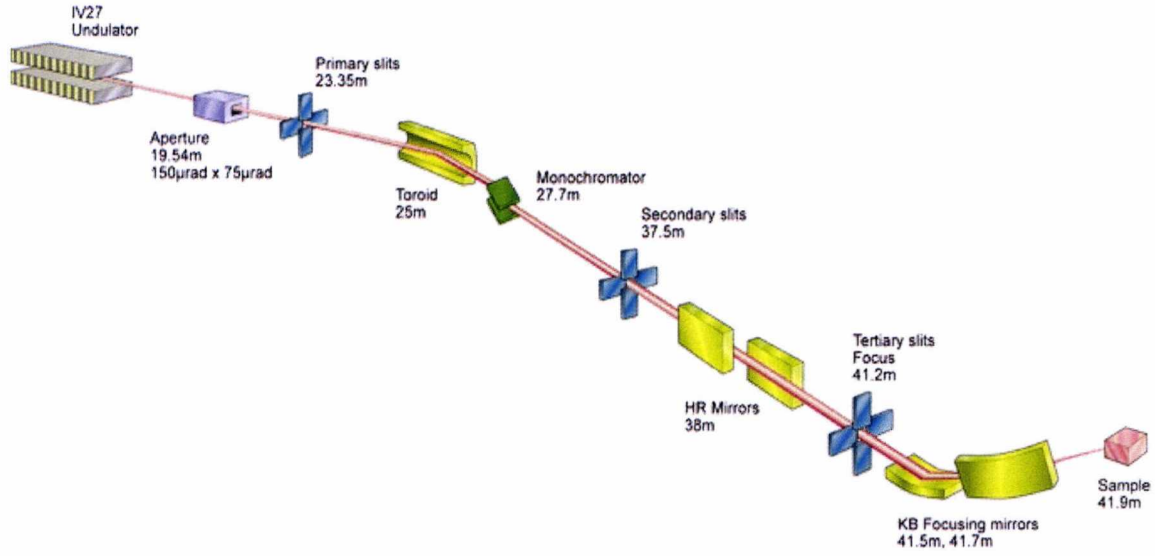

Figure 22: The set-up of the optics microfocus station I18 at the Diamond Light Source [diagram used with permission of station I18 Diamond Light Source].

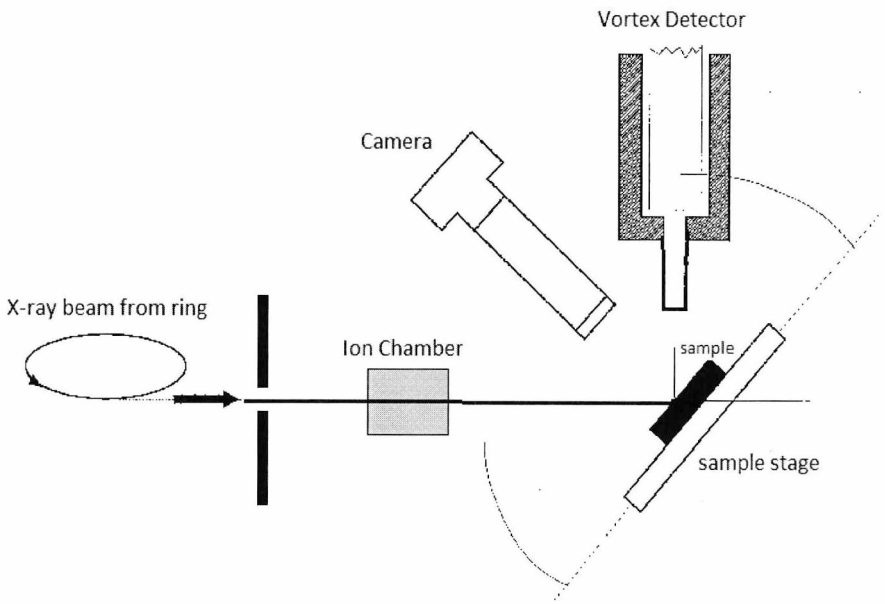

Figure 23: The set-up of the hutch for XRF runs on microfocus station I18 at the Diamond Light Source.

II.5.1 The source

X-rays used in microfocus spectroscopic experiments are generated very much in the same way as X-rays from synchrotron X-ray sources. The instrumentation used for focusing in micro focus experiments are however different.

On a third generation synchrotron there are three types of magnetic devices that are used to produce the X-rays used on a medium energy X-ray beamline; there are bending magnets which are the devices that keep the electrons circulating around the synchrotron; there are multipole wigglers that have a very high magnetic field which shifts the peak flux to much higher energy than available from the bending magnets, and there are undulators - these are a series of periodic magnets which give an output that is gap dependent, consisting of discrete regions of high intensity where there is constructive interference and a background of much lower intensity.

The use of an undulator for a microfocus beamline is advantageous because of the shape of the undulator output. For peak intensities the outputs are in a narrow cone with a small divergence. This allows for a larger percentage of the output to be retained upon refocusing the beam to a very small spot size at the sample and thus a higher intensity is normally achieved.

II.5.2 Focusing

On a microfocus beamline often a toroidal mirror is used as one of the first optical elements to refocus the X-ray beam from the source onto a pair of beam defining slits to produce a virtual source which is then imaged by the final demagnifying optics. This optical layout offers a simple way to adjust the beam size at the sample without altering the focus of the final focusing device. Changing the size of the virtual source using the slits can alter the image size at the focus.

There are a variety of ways of producing the final focused beam and the method depends on a number of variables, such as the required beam energy, the final spot size, the focal length, the degree of monochromacity and, for an XAS experiment, the energy range to be scanned.

There are three main techniques employed in the focusing of beams [40]. Kirkpatrick–Baez (KB) mirrors [80, 81] are widely used as focusing devices as they allow the focal distance to be maintained when the energy is scanned, which is a requirement for XAS experiments for both the XANES and EXAFS regions. KB systems can readily produce spot sizes in the micrometer range and to move into the sub-micrometer regime requires very high quality mirrors [82].

Fresnel zone plates (FZP) used in X-ray microscopy can be used to resolve features as small as 30 nm [83] and spot sizes as small as 1 nm appear to be possible in the future using novel adaptations of the technique [84-86]. FZPs tend to be used at energies less than 13 keV and the shift in focal length with beam energy restricts the use in XAS to the XANES region. Tapered glass capillaries offer a third method of beam focusing by squeezing the beam [85, 86]. However the minimum spot size with current technology is around 10 microns. This can be improved and the system made more efficient by using

a FZP to pre-focus the beam prior to entry to the capillary [82] and spot sizes as small as 0.25 micron have been reported [83]. In terms of spectroscopy these systems allow coverage of the XANES region [82].

On most spectroscopic microfocus beamlines two (KB) mirrors are used to produce the small spot required. They are typically 100 - 200 mm in length and they focus (and reflect) the beam in orthogonal planes to the same spot. The focal length from the second (downstream) mirror of a typical KB mirror pair on a microfocus beamline is between 100 and 200 mm

Energy selection at microfocus spectroscopy beamline is achieved by a fixed-exit double crystal monochromator (Figure 22). This is often cooled cryogenically to offset the high temperatures produced by the X-rays.

Silicon or germanium detectors are normally used to detect fluorescent X-rays coming from the sample. Germanium detectors are better above 15 keV, whilst silicon-based detectors are often better below 4 keV. The energy resolution of each device is between 150-250 eV and they can typically count at rates of several hundred kHz per channel.

II.5.3 Examples of microfocus experiments in archaeology

Micro-focus X-ray analyses have been employed in the investigation and study of materials of archaeological or historic importance [40].
Studies using micro-focus XAS and XRF have been carried out to determine the copper speciation in mediaeval glass using beamline 10.3.2 at the Advanced Light Source (ALS) with a spot size of 5 × 5 micron [87].
The use of copper compounds as colouring agents or pigments has been widespread through the ages. Divalent copper ions, Cu(II) produces a sky blue to green colouration [88, 89] whereas monovalent copper ions, Cu(I) is colourless. These colours are due to the *d*-electron configuration of the Cu ions and crystal field effects [90]. Cuprite, $Cu(I)_2O$ is red, due to it being a semiconductor with an appropriate band gap [91], and in the past red glass has qualitatively been ascribed to inclusions of this compound (see, for example [92]).

More recent work and studies into the use of nanoparticles in such applications has shown that the glass colour depends on the size of the cuprite nanoparticles, which itself is determined by composition and thermal history, and can be red, green, orange or yellow [93]. Speciation work has shown that nanoparticles of metallic copper, Cu(0), can produce bright red colours in many artefacts [94-97]. In this case the colour is due to Mie scattering and the colour depends on both the size and shape of the particles; round for red and oblate for blue. From the above it is clear that measurements of the copper speciation are integral to understanding the origin of the colour of ancient glass.

The work done at the ALS focused on three samples of 13th and 14th century red flashed stain glasses from the Saint Gatien cathedral in Tours which is situated in the French Loire valley. The surfaces of these glasses have undergone severe weathering [87]. Red stained glass are classified as four types [88] and the Tours glass consists of two of these types; type II which is composed of a thin layer of feuilleté (flashed glass) that is deposited on a much thicker, pale-green glassy substrate (dated in the 13th and 14th centuries), and type III (known as plaqué) composed of a homogeneously red glass layer inserted between two colourless layers of glass.

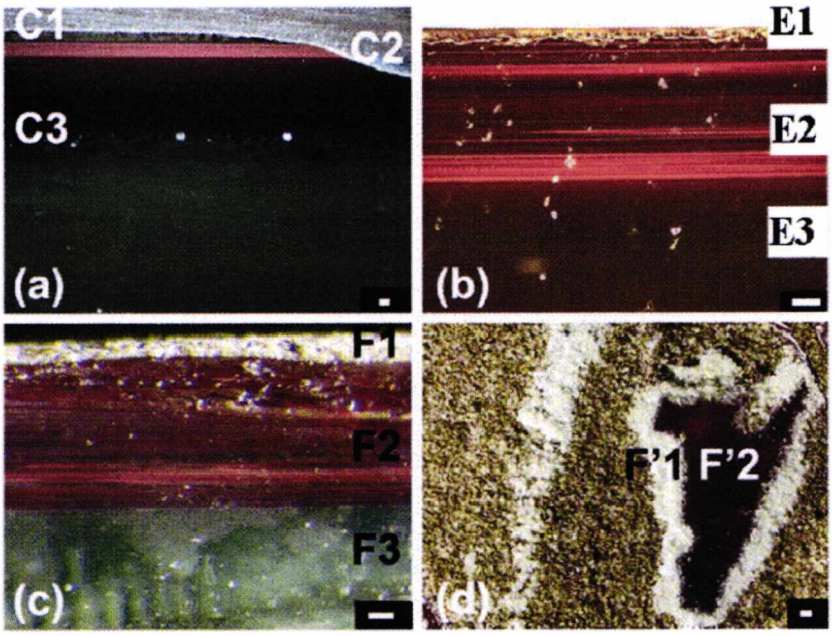

Figure 24: Optical micrographs of the glass samples [87]

Glasses E and F are type II containing a thick red layer (~1.5 mm on average). This layer is composed of a complex intercalation of micron size "sub-layers" of red and greenish glass (see a cross section in Figure 24b and c). Above this red layer, a variably thick corrosion layer is sometimes observed (Figure 24 c). In glass F, this layer is usually a few microns thick. The corrosion layer in glass E is less developed and of sub-micron thickness. Glass C is type III with a relatively thinner (~0.1 mm thick on the average) red layer and appears homogeneous under optical and electronic microscopes (see a cross section in Figure 24a).

High resolution Cu K-edge XANES spectra were collected through the polished sections of the C, E and F glasses, and compared to samples of Cu_2O (cuprite), turquoise Cu(II) and native Cu. The spectra are shown in Figure 25.

The absence of feature A in the pre-edge region (shown in Figure 24), and the high intensity for feature B is indicative of large amounts of Cu(I) in these three glasses (>90 atomic percent). Features C', D, E and E' observed only for glass (C) are similar to those measured in native Cu.

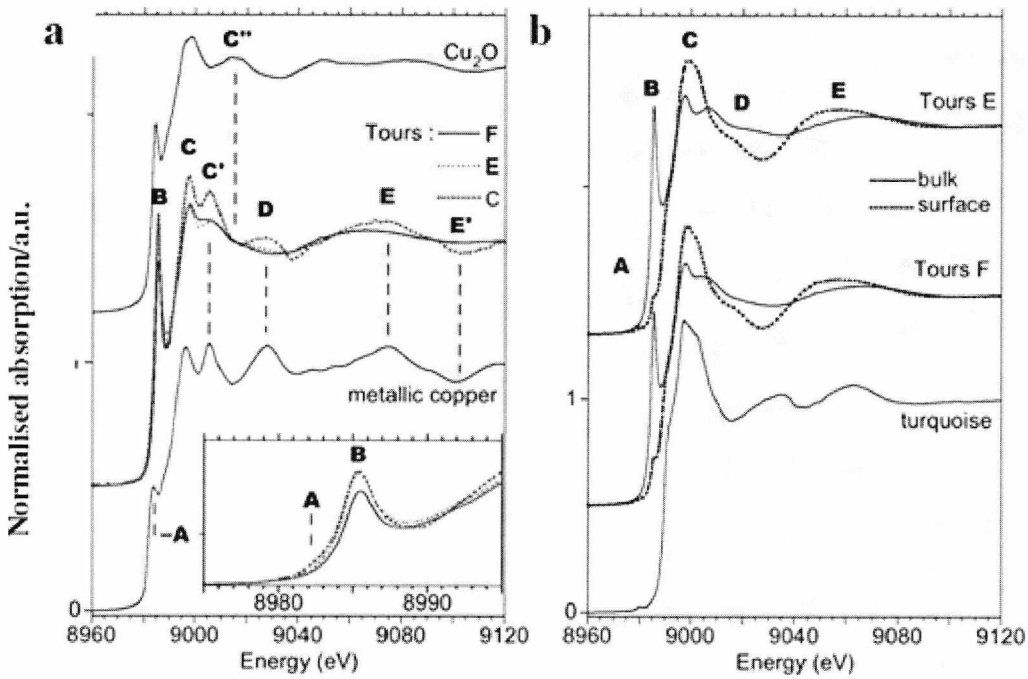

Figure 25: High resolution microfocus XANES of Tours glass [87]

The pre-edge area shows a shoulder on the low energy side of feature B attributed to the presence of metallic Cu in the sample. Features D and E' are not observed for glasses E and F (feuilletés), in contrast to feature C'.

It was concluded that this feature is also attributed to the presence of metallic Cu as sub-nanometer inclusions. In that case, it was hypothesized that the metallic clusters are so small and disordered that they appear only in the near edge region (where the intensity of features is reduced less by disorder). This was confirmed by examination of the Cu K-edge XANES spectra collected of nanoparticles of metallic Cu, which show a dark red colour [97, 98] and feature C' can be assigned to nanocrystalline Cu metal in these glasses. Comparative XANES studies were carried out with cuprite and results showed that there was no evidence for significant amounts of Cu as cuprite in any of the glasses from Tours. Among these three glasses, sample F shows the least metallic clusters. Glass E has a Cu speciation that is in between that for glass F and that for glass C.

Linear combination between nanocrystalline Cu and the standards suggests that 10 to 15 atomic percent of the total Cu are present as metallic

nanoclusters in glass E and F, respectively (25 atomic percent in glass C). Spectra are shown in Figure 26 of the glass C.

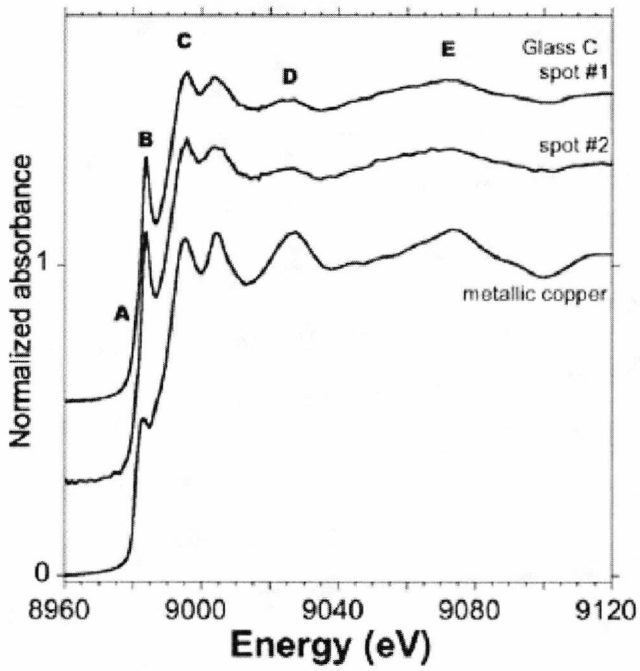

Figure 26: High resolution microfocus XANES of Tours glass C [87]

The speciation in glass C was confirmed by microfocus Cu K-edge XAS measurements. Copper rich spherical spots in this glass were identified by XRF scans that were probably less than 1 micron diameter and the XAS spectra from two of these spots are shown in Figure 26. The XANES data, Figure 25 appear to be a combination of Cu(0) and Cu(I), there is no evidence of feature A and a sharp feature B.

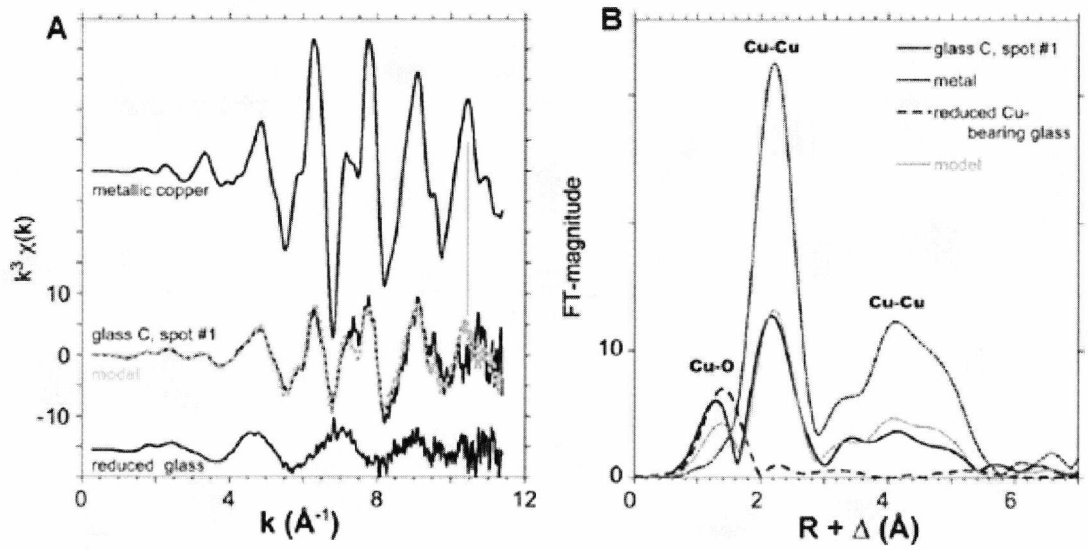

Figure 27: Microfocus XAS and Fourier transform of Tours glass C [87]

The normalised EXAFS and the Fourier transform from one of the spots are shown in Figure 27A and 27B, respectively. Also shown are the corresponding plots for metallic Cu and a reduced red Murano glass, which contains Cu(I). The Fourier transform of the spot shows peaks at ~1.2 and 2.2 Å, corresponding to Cu-O and Cu-Cu correlations. A linear combination of the two standards gave a best fit with 70% Cu(I) and 30% Cu(0), with an error of 5% which are close to the values from the bulk XANES.

The presence of sub-micron copper nanoparticles within the red coloured layer of the glass would not have been detected with electron microscopy as most of the particles are buried in the glass matrix.

Microfocus XRF measurements showed that glass E has a complex series of micron-scale red layers with greenish layer insertions and a corroded surface. The deepness of the red colour depends on the copper concentration. The microfocus Cu K-edge XANES for five spots were collected in the various areas of interest of the glass E and are shown in Figure 28.

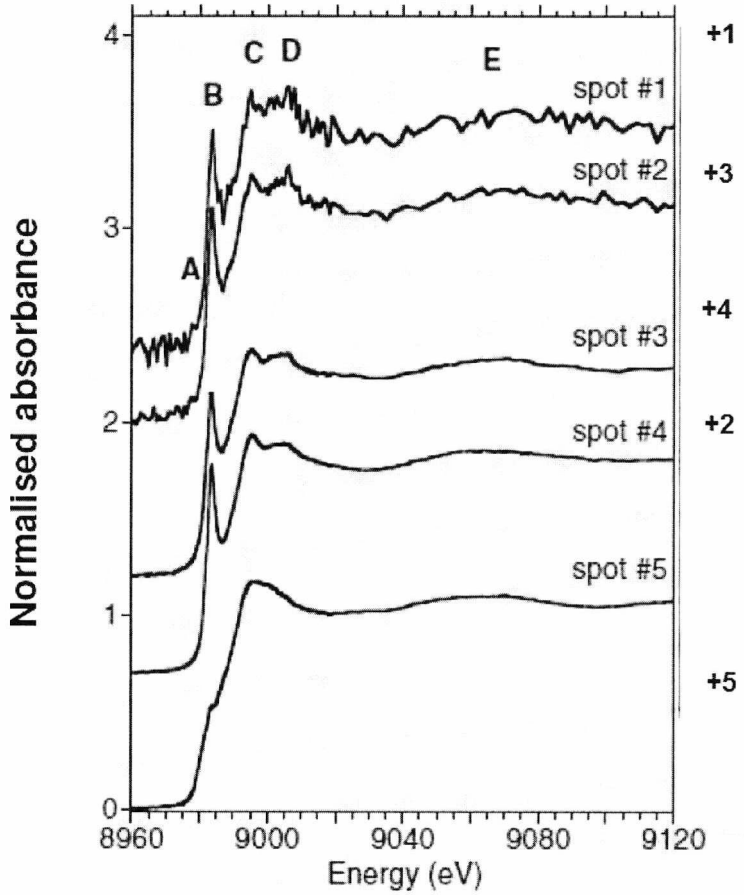

Figure 28: Microfocus XAS and Fourier transform of Tours glass [87]

The XANES from four of the spots are predominately of Cu(I) with a small amount (5 %) of Cu(0). However, the XANES for spot #5, at the glass surface, is typical of Cu(II). The microfocus Cu K-edge EXAFS of spots #4 and #5 are shown in Figure 28. The Fourier transform for spot #4 shows a single peak at ~ 1.4 Å due to a Cu–O bond. In contrast, the Cu–O peak for spot #5 is a doublet, located at longer distances (centred near 1.5 and 2.2 Å) typical of distorted Jahn–Teller units around Cu(II), as in copper acetate [99].

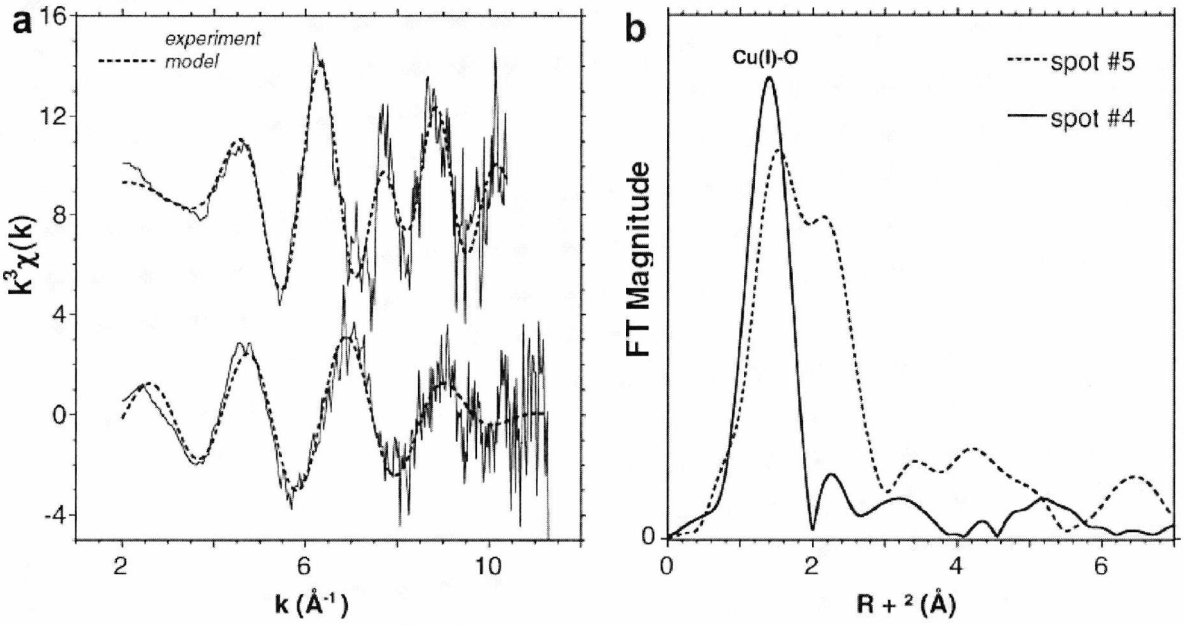

Figure 29: Microfocus XAS and Fourier transform of Tours glass F [87]

Similar experiments for glass F showed that the central regions of the glass contained predominantly Cu(I). However, the highly corroded surface gave a Cu K-edge XANES that was predominantly Cu(II) and compared favourably with that for chalcanthite ($CuSO_4.5H_2O$). The XAS are shown in Figure 29.

This study of the Tours cathedral glass emphasises the power of the microfocus techniques. It unravelled the complex copper speciation of the red glass, in some samples showing that copper was present as nanoparticles which would not be detected by electron microscopy. In addition, the experiments showed that in some samples the surface corrosion led to the formation of an amorphous copper sulfate, rather than the expected copper acetate which is a common ingredient of verdigris, the patina formed on weathered copper.

II.6 Chemical techniques

II.6.1 Chelation Chemistry

A ligand is an ion or a molecule that donates a pair of electrons to a metal in forming a coordination complex. Ligands generally act as Lewis bases. The site that donates the electrons on such a molecule is called the binding site. The formation of complexes between ligands and metal ions is referred to as chelation. A chelate is a complex in which a ligand uses two or more binding sites to coordinate a metal. Ligands with two or more coordination sites are referred to as chelating agents. The more coordination sites there are the more stable the resulting complex is so polydentate ligands form more stable complexes compared to complexes formed by monodentate ligands. This is referred to as the chelate effect. This effect is generally due to an increase in entropy that accompanies chelation. The stability of a chelate is also related to the number of atoms in the chelate ring. Monodentate ligands contain one coordinating site and are easily broken apart by other chemical processes; polydentate chelators, contain multiple binding site (coordination sites) and upon binding with a metal ion, the resulting complex is more stable compared to complexes formed by monodentate ligands. There are many know ligands that complex metal ions (for example iron) and render them soluble in water. The complexes formed though soluble are stable and allow this phenomenon to be used in many applications for example, the transport of iron in plants and in the treatment of metal poisoning in humans and animals.

There is a vast literature on chelating agents due to their clinical applications [100]. Here the focus will be on the agents used in this work, namely, Ethylenediaminetetraacetic acid (EDTA), Diethylenetriaminepentaacetic acid (DTPA), calcium phytate, (Cal. Phy) and ammonium citrate (Am. Cit.).

EDTA and DTPA are common synthetic chelating agents for iron with a range of industrial applications [101] and the structures are shown in Figure 30. Phytic acid (inositol hexaphosphate) is a naturally occurring compound (in wheat and pulse husks) which strongly binds metal cations and is also an antioxidant [102, 103]. High phytate levels in a diet can cause health problems by locking up metal ions essential to the body [103]. Citric acid,

another natural compound which is found in citrus fruits is a good binding compound for metal cations [104].

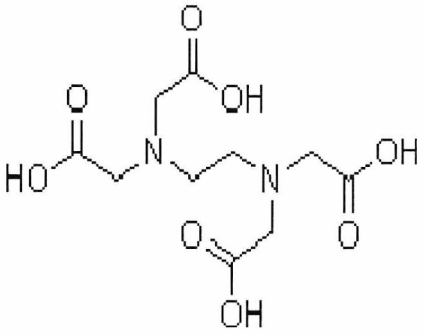

EDTA

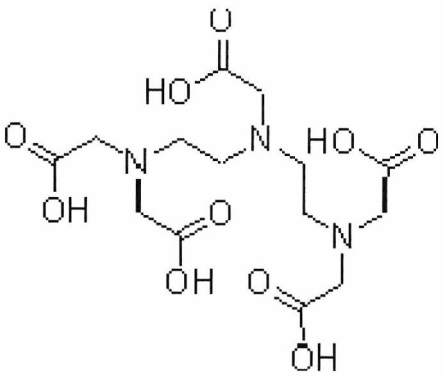

DTPA

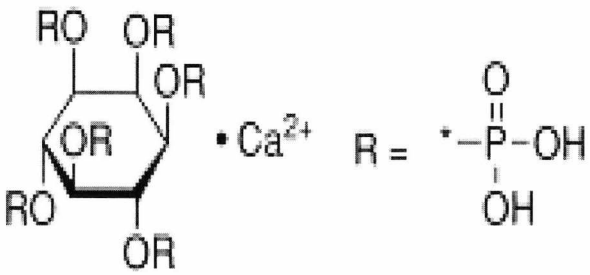

Calcium phytate

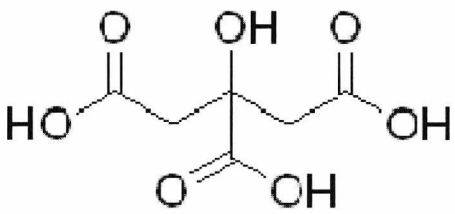

Citric acid

Figure 30: The structures of the chelating agents used in this work.

II.6.2 Titrimetric Methods of analysis

Titrimetric analysis is the quantitative analysis of a solution. It provides information like the number of moles or percentage composition of a substance in solution. This is achieved by adding the solution under investigation (the titrand) volumetrically, with a glass or automatic burette to a standard solution of known concentration and volume (titrant). An indicator is normally added to the standard solution to help determine the end point (the end point is when the stoichiometry of the titrand is equivalent to the standard solution (titrant)). The end point is typically accompanied by a colour change. In experiments where a suitable indicator is not found the redox potential can be used to determine the end point. In this instance the the will be a sharp rise in the e.m.f. at the end point.

Titrimetric methods of analysis have the virtue of being like gravimetric methods, absolute in that the concentration of the substance in question is determined from the basic principles of chemistry, and no calibration curves are required.

II.7 Scanning electron microscopy (SEM)

The scanning electron microscope creates magnified images by using electrons. It can create detailed images of samples at much higher magnification than is possible in optical microscopes. Electrons are emitted from a cathode by an electron gun under vacuum, accelerated using an electric field towards the specimen. The electrons are focused using metal apertures and magnetic lenses into a thin monochromatic beam which then collides with the sample [105]. The electrons which typically have energies of up to 40 keV are focused on the sample and scanned along parallel lines. When these electrons interact with the sample, they lose energy due to energy exchange. These interactions and energy exchange results in the emission of electrons referred to as secondary electrons with energy levels of a few tens of eV [106]. These secondary electrons along with high energy electrons backscattered by the sample and characteristic X-rays and collected to form a 3-dimensional image of the sample surface. Therefore there is both structural and elemental composition information, the latter from energy dispersive X-ray spectroscopy (EDX) of the emitted X-rays. This technique can be used to determine the extent of degradation in the *Mary Rose* timbers. It can also be used to determine where in the wood sulfur crystals tend to be collected [9] (see Figure 31)

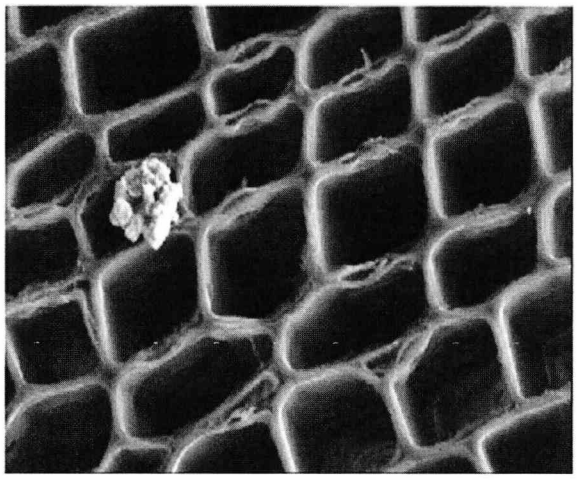

Figure 31: Scanning electron microscopy transverse cross-section of a marine archaeological wood (oak) showing sulfur crystals [9].

III. EXPERIMENTAL

III.1 Samples

Samples from different part of the *Mary Rose* were analysed along with some recently recovered wood from the wreck site believed to be part of the *Mary Rose*. Some samples from Newport wreck site were also analysed in preliminary studies for comparison. Fresh oak was also used in the study on the effects of chelating agent solutions of wood constituents.

List of Samples

Sample ID	Sample Description
MRT04	*Mary Rose* timber recovered in 2004
MRT05	*Mary Rose* timber recovered in 2005
MRT03_0074	*Mary Rose* timber recovered in 2003 batch 0074
MRT04_NBH	*Mary Rose* timber recovered in 2004 sample taken near bolt hole
MRT03_T0022	*Mary Rose* timber recovered in 2003 batch T0022
MRSPU04	*Mary Rose* stem post unit raised in 2004
MR06_WS	Timber raised from wreck site in 2006
MR_Arrow Tip	Tip of arrow used by *Mary Rose* archers
MRCS_PEG	*Mary Rose* Core sample taken in 2010. PEG treated for several years
CS_UL	Core sample from upper level of the *Mary Rose* PEG treated
CS_LL	Core sample from lower level of the *Mary Rose* PEG treated
MRT06	*Mary Rose* timber recovered in 2006
MRT MD	*Mary Rose* sample taken from main deck
NE Fe	Sample from Newport bay wreck, high in Fe
SL03	Sample from Somerset Level recovered in 2003
MR SFK	*Mary Rose* sample recovery date unknown

III.2 Iron Extraction

The following chelating agents were used in this project:

DTPA: Diethylenetriaminepentaacetic acid

EDTA: Ethylenediaminetetraacetic acid

Cal Phy: Calcium Phytate

Am Cit: Ammonium Citrate

Cit Ac: Citric Acid

All these materials were purchased from Aldrich Ltd.

III.2.1 Preparation of solutions of chelating agents

0.2M EDTA.Na_2 Solution

EDTA.Na_2 (18.61g - 0.05moles) was dissolved in 100ml of water with stirring. The pH was adjusted to about 7 by adding NaOH pellets. The EDTA.Na_2 did not dissolve completely until the pH reached about 6. With careful addition of NaOH, pH levels were maintained around pH 7 for most of the solutions made. The resulting solution was made up to 250ml by adding distilled water.

0.2M DTPA Solution

DTPA (19.67g - 0.05moles) was dissolved in 100ml of water with stirring. The pH was adjusted to about 7 by adding NaOH pellets. The DTPA did not dissolve completely until the pH was about 5. The solution was the made up to 250ml by the addition of distilled water. With careful addition of NaOH, the pH level can be maintained around pH 7

0.2M Ammonium citrate Solution

Ammonium citrate (11.31g - 0.05moles) was dissolved in 100ml of distilled water. The pH was adjusted to about 6.4 by adding NaOH pellets. The resulting solution was made up 250ml by adding distilled water.

0.2M Citric acid Solution

Citric acid (9.61g - 0.05moles) was dissolved in 100ml of distilled water with stirring. The pH was adjusted to about 7 by adding NaOH pellets. The resulting solution was the made up to 250ml by adding distilled water.

0.2M Calcium phytate Solution

Calcium phytate (34.9g - 0.05moles) purchased from Aldrich was dissolved in 100ml of distilled water with stirring. The pH was adjusted to about 7 by adding NaOH pellets. The resulting solution was the made up to 250ml by adding distilled water.

A second set of solutions (termed 'in-house') were prepared by adding phytic acid (50% w/w from Aldrich) to calcium carbonate. Ammonium hydroxide was added to adjust the pH to 7.

Lower concentrations of the above solutions were obtained by further diluting some of the original solutions.

III.2.2 Treatment of samples

Samples were cut into 6cm sections and in most cases halved longitudinally. One half of each of the samples was then treated with 200ml of various concentrations of the chelating solutions for 6 weeks. Where necessary (due to heavy iron encrustation) the solutions were replaced with fresh ones every week to aid iron extraction. The other halves were kept for comparative analyses.

III.3 XAS Experiments

III.3.1 Bulk XAS Experiments at the Daresbury SRS

Bulk XAFS measurements were taken on station 16.5 at the Daresbury SRS, a second-generation source operating at 2 GeV. This station was especially designed [107] to perform XAS experiments on ultradilute materials, i.e. down to ppm levels for some elements. Station 16.5 uses a double crystal Si(220) monochromator with sagittal focus up to 27keV and a 30-element germanium solid-state detector with high count-rate electronics; measurements were made at room temperature. The sagittal focusing allows the station to overcome the constraint of not being able to adjust mirror angles to optimise harmonic rejection at the scanning energy which is desirable for a station scanning over such a wide range of energies. This is so because such an operation is not possible when the mirror also performs the function of horizontal focusing, as the ground-in sagittal curvature requires it to operate at a fixed angle of incidence [107].

Sagittal focus, harmonic rejection and correction for crystal twist are all adjusted dynamically during scanning. In order to maintain beam intensity and constant higher harmonic rejection a servo system operates on the pitch axis. This is implemented in software and operates after the motor moves for each data point are complete. Once the required tolerance (measured-reference) is reached, data acquisition commences. No further adjustments are made during this period. A tolerance of ±0.5% is used. A smaller tolerance results in increased dead-time with no improvement in the signal-to-noise ratio. During scanning there is an additional dead-time penalty of approximately 2.5 s per data point compared with the unfocused mode. This penalty is however offset by the substantial gains in flux which are typically a factor of ten or more, depending on sample size. This means scan times are often long, typical time for a single EXAFS scan is 30–50 min in total [107].

Between 4 and 8 scans were collected for each sample. Edge calibration was done with reference to an iron foil transmission measurement.

During our analyses of *Mary Rose* samples at station 16.5, the intensity of the incident beam and the detection geometry were kept constant where possible to allow a quantitative comparison of the Fe content from the XAS edge step. This was done by capturing images of samples mounted in

sample holders and measuring distances from the detectors. The set up is shown in Figure 32.

Figure 32: The sample arrangement used on station 16.5. The position of the beam was 'spotted' with a laser beam and photographed. This allowed the spot to be re-located in future experiments.

Data analysis used EXCALIB and EXSPLINE for calibration, summing and background subtraction, whilst EXCURV98 was used for *ab initio* calculation of the phase-shift corrections and for curve-fitting analysis of EXAFS data [29], as described in Section II.1.5..

Two pieces of recently recovered timber (MR03-T0022 and MRT04) from the *Mary Rose* were cut into 6cm long sections, as shown in Figure 33.

EXAFS was collected at the Fe K-edge from these before and after six weeks treatment with solutions (200ml) of various chelating agents. Additionally a third piece (MR03-0074) which was very heavily discoloured with orange iron corrosion products was also measured and treated. These have been labelled in the figures with a sample reference number: (AB1) MR03-T0022, treated with

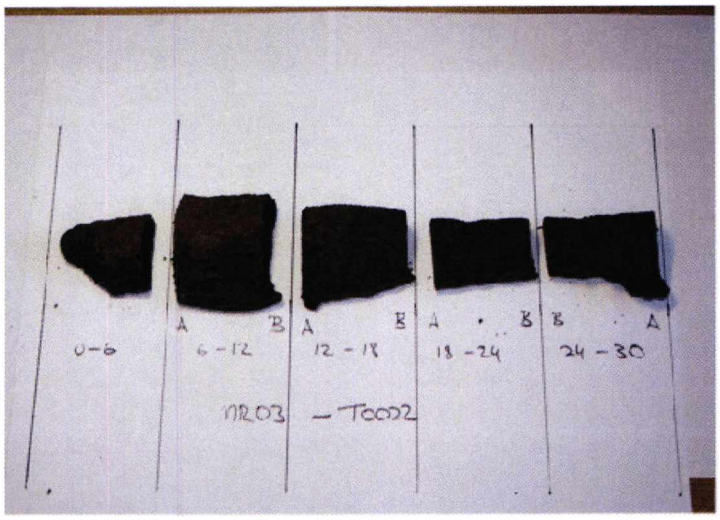

Figure 33: Picture of MR03-T0022 cut into 6cm strips.

0.1M calcium phytate; (AB2) MR03-T0022, treated with 0.1M DTPA; (AB3) MR03-T0022, treated with 0.1M EDTA; (AB4) MR03-T0022, treated with 0.05M EDTA; (AB5) MR03-T0022, untreated only; (AB6) MRT04, treated with 0.05M calcium phytate; (AB7) MRT04, treated with 0.1M ammonium citrate; (AB8) MR03-0074 treated with 0.05M DTPA. The wood samples had been kept in a moist condition since excavation and were measured in air and hydrated, wrapping them in thin polymer sheet to prevent drying.

After the first measurements the samples were treated with solutions of chelating agents (200ml) for 6 weeks and XAFS measurements taken duplicating incident beam and the detection geometry from the first experiment wherever possible.

List of samples used and their identification names are listed in table below.

Table 1: List of treatments of the *Mary Rose* timbers for bulk XAS experiments.

Sample		Treatment
ID	**Name**	
AB1	MR03-T0022(0-6cm)	0.1M calcium phytate
AB2	MR03-T0022(6-12cm)	0.1M DTPA
AB3	MR03-T0022(12-18cm)	0.1M EDTA
AB4	MR03-T0022(18-24cm)	0.05M EDTA
AB5	MR03-T0022(24-30cm)	Not treated
AB6	MRT04(0-6cm)	0.05M calcium phytate
AB7	MRT04(6-12cm)	0.1M ammonium citrate
AB8	MR03-0074	0.05M DTPA

III.3.2 Bulk XAS at Soleil station SAMBA

Some additional Fe bulk XAS measurements were collected at station SAMBA on the French synchrotron, Soleil. This station is the standard XAS station at Soleil and is basically equivalent to station 16.5 at the Daresbury SRS. The energy range for SAMBA is 4 to 40 keV and there is sagittal focussing to improve the beam intensity. To collect Fe XAS a Si(111) monochromator is used. The station can collect XAS in transmission mode with ion chamber detectors and for fluorescence mode a VORTEX silicon drift detector is employed (similar to the one on Diamond station I18). In this run three different samples from the *Mary Rose* were used; a description of which is found in Table 2 below. The aim of the experiment was to investigate the effectiveness of solutions of DTPA and Cal Phy in the extraction of iron species from PEG treated samples compared with non PEG treated sample. XAS measurements were taken of the samples pre-treatment and post-treatment and results analysed and compared.

Table 2: List of samples and corresponding treatments of the *Mary Rose* timbers for bulk XAS experiments at Samba.

Sample ID	Description	Treatment
AB1U	*Mary Rose* sample recovered in 2004	Untreated
AB1T	*Mary Rose* sample recovered in 2004	Treated with 0.1M DTPA
AB2U	*Mary Rose* sample recovered in 2004	Untreated
AB2T	*Mary Rose* sample recovered in 2004	Treated with 0.05M Calcium Phytate
CS_UL	Core sample from upper level of the *Mary Rose*, PEG treated	Untreated
CS_LL	Core sample from lower level of the *Mary Rose*, PEG treated	untreated
CS_ULT	Core sample from upper level of the *Mary Rose*, PEG treated	Treated with 0.1M DTPA
CS_LLT	Core sample from lower level of the *Mary Rose*, PEG treated	Treated with 0.05M Calcium Phytate

III.3.3 Microfocus (XAS and XRF scans on Diamond station I18)

Measurements were undertaken on the microfocus station I18 at the Diamond Light Source. The principles of this station were described in Section II.5 and more detail can be found in reference [108]. Several runs were undertaken and the details of the runs are described below.

III.3.3.1 First Run

Samples from the *Mary Rose* were cut into 6cm sections and halved longitudinally. These samples were then treated with 200ml various concentrations of the chelating solutions for 6 weeks. The following chelating agents were used: diethylenetriaminepentaacetic acid (DTPA), ethylenediaminetetraacetic acid (EDTA), calcium phytate (Cal Phy).

In some cases the solutions had to be replaced to aid iron extraction due to high levels of high levels of iron contamination. The other halves were wrapped in cling film and sealed to keep them from drying out and also cut down on oxidation of iron and sulfur species present.

A day before the XAS measurements at station I18 at the Diamond Light Source, the samples were removed from solutions and rinsed with de-ionised water thoroughly and wrapped in Cling film and sealed (making sure they were kept moist and did not dry out).

I18 is a microfocus beamline [108] which operates an optical scheme based on three mirrors and a liquid nitrogen-cooled double crystal monochromator. The first device is 25 m from the source, and is a water-cooled Rh-coated Silicon toroidal mirror. This is used to focus the beam in the horizontal plane at 37.5 m from the source, and adjusts it in the vertical direction. The second is a fixed-exit monochromator which has two sets of crystals available Si(111) and Si(311). The angular range of the monochromator is such that it can cover from 2 – 20 keV on the Si(111) set, though the Si(311) set will give better resolution and is likely to be used for most work above about 15 keV. For the sulfur K-edge runs the sample and external optics and detectors were surrounded by a helium filled plastic bag to eliminate air absorption of the beam.
The third device is two pairs of mirrors situated in the experimental hutch. First there is a pair of plane mirrors, which is used for harmonic rejection and the Kirkpatrick-Baez focusing mirrors. These are non-chromatic and thus allow the station to run energy scanning applications like EXAFS. Energy calibrations were checked at regular intervals using Fe metal strips.
A high rate 9 element germanium solid state fluorescence detector system optimised for energies above 5 keV was used in this run.

XRF (X-ray mapping) scans were also carried out on the samples during this run at energies of 7124 eV (for Fe^{2+}), 7300 eV (for Fe^{3+}), 2473.2 eV (for elemental sulfur/organosulfur), 2482 eV (Sulfate) and 2600 eV (for total sulfur content)

The aims of the experimental run were to determine:

a) The correlation of the sulfur and iron speciation as a function of position in the timber using XRF and Fe and S K-edge XANES mapping.

b) The correlation of the degree of degradation of the wood cells with the sulfur and iron species present using diffraction mapping..

c) The chemical nature of the mineral inclusions using Fe and S K-edge EXAFS mapping.

III.3.3.2 Second Run

A second set of analyses was carried out on samples from the *Mary Rose* at station I18 at the Diamond light source in January 2009. The first run gave a better understanding of the chemical speciation within the timbers and also the way the hardware and software at the station work. The experimental set-up was the same as in the first run with one exception; some of the XRF maps were collected without the harmonic rejection mirrors in the optics. This allowed higher energies to be scanned through the higher harmonics, i.e. two times, three times, etc. the energy of the fundamental beam. As the fluorescence X-rays are collected in a multichannel analyser it was possible to collect maps for both sulfur and iron in the same scan. Hence there is a better correlation for the positions of the iron and sulfur species in the samples.

In this experiment, timbers from the *Mary Rose* were cut into 6cm strips and halved longitudinally. One half of each sample was kept moist and stored and the other half treated in a 200ml solution of a chelating agent for four weeks. A table of samples and the treatments used are in the Table 3 below.

On the day of the experiment, 1-2 mm strips were taken from each sample and mounted on sample holders covered by Mylar to stop them from drying and shrinking during the experiment. Optical micrographs of the mounted samples were captured before the runs to help with beam positioning and navigating around the sample once mounted in the experimental station. The holder used on I18 is shown below in Figure 34.

Thin timber section mounted in the polycarbonate in-situ treatment cell (white circular object) and mounted on the I18 beamline. X-rays come from the right and the photograph taken from the position of the X-ray fluorescence detector used to collect the spectroscopic data.

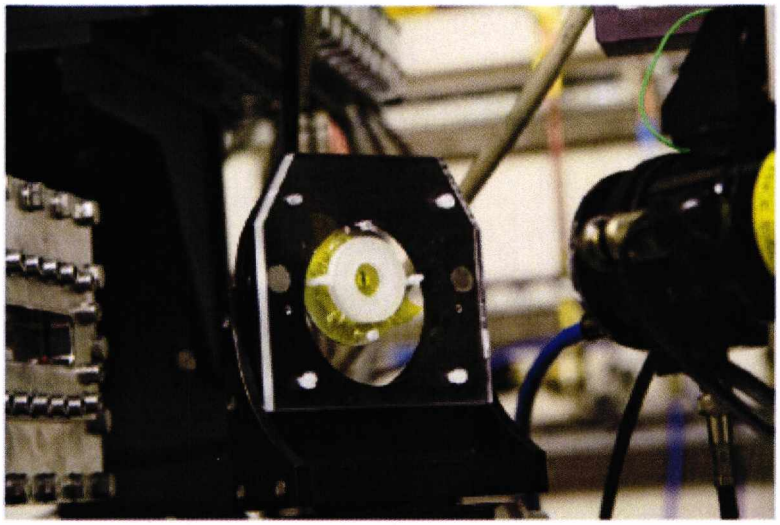

Figure 34: Sample set-up on Station I18.

Table 3: List of treatments of the *Mary Rose* timbers for microfocus XAS experiments.

Sample ID	Description	Treatment
MRT04_AB1U	*Mary Rose* sample recovered in 2004	Untreated
MRT04_AB2U	*Mary Rose* sample recovered in 2004	Untreated
MRT04_AB3U	*Mary Rose* sample recovered in 2004	Untreated
MRT04_AB4U	*Mary Rose* sample recovered in 2004	Untreated
MRT03_AB5U	*Mary Rose* sample recovered in 2003	Untreated
MR(A002)_AB6U	*Mary Rose* sample batch A002	Untreated
MRT04_AB1T	*Mary Rose* sample recovered in 2004	0.5M Cal. Phy.
MRT04_AB2T	*Mary Rose* sample recovered in 2004	0.25M Cal. Phy.
MRT04_AB3T	*Mary Rose* sample recovered in 2004	0.45M Cal. Phy. (made in house)
MRT04_AB4T	*Mary* Rose sample recovered in 2004	0.03M Cal. Phy. (Made in house)
MRT03_AB5T	*Mary Rose* sample recovered in 2003	0.1M DTPA
MR(A002)_AB6T	*Mary Rose* sample batch A002	0.05M DTPA

Iron and sulfur microfocus XANES and EXAFS were collected in fluorescence mode at various points on each sample (treated and untreated) to provide a better idea of the iron speciation across a given sample. Beam size was around 5 microns. The detector was moved backwards or forwards to avoid detector saturation and provide better counts respectively. XANES of standard iron and sulfur compounds were also collected for comparison and to allow the oxidation/coordination of iron and sulfur species in the samples to be deduced. XRF scans were also taken at specific energies to allow the deduction of Fe^{2+}/ Fe^{3+} ratio and also total iron content. The same was done to deduce the sulfate/elemental sulfur ratio along with the total sulfur content in the samples. Rough XRF scans were first taken using step sizes of around 10-20 µm over large areas to allow us to determine iron or sulfur rich areas of samples and then detailed scans over these areas were carried out using much smaller step sizes (around 5µm)

The focus was on collecting data on fewer chelating agents at various concentrations during this experiment to allow us to repeat experiments if need be to provide higher quality data albeit fewer.

III.3.3.3 Third Run

The third run on I18 focused on a specially selected sample; an arrowhead artefact from the *Mary Rose*. The sample studied was from the tip of an arrow, which would originally have been sheathed by the iron arrow head, which had been completely corroded during its exposure to seawater. This artefact had been washed and treated with PEG immediately after it being recovered from the sea. These included treatment with grades PEG400 and PEG4000, before freeze drying. Therefore, compared to the timber samples, it had a relatively short exposure to the normal atmospheric influences, i.e. oxygen and moisture. The experiments involved taking small sections of the artefact, recording microfocus XAS measurements, treating with chelating agent and re-recording the microfocus XAS.

Additional information for this sample were scanning electron microscope (SEM) images that were collected of the thin section after X-ray analysis using a Hitachi TM3000 tabletop microscope. These pictures were kindly taken by Dr A.D. Smith (STFC, Daresbury Laboratory).

III.4 XRD Experiments

Powder X-ray diffraction patterns for some samples were collected on a conventional laboratory machine in the School of Physical Sciences. The instrument is a Phillips PW1720 instrument using a Cu K_α tube operating at 35 kV and 20 mA.

III.5 XRF Experiments

X-ray fluorescence spectra were collected for some samples using a Fischerscope® instrument associated with station I18 at the Diamond Light Source. This is a conventional bench-top instrument with a tungsten source. The source operates at 30 kV, self-focuses the beam and produces a spot size of 600 microns. Calibration was performed using pure samples of elements and internal library information.

III.6 SEM Experiments

Samples from the *Mary Rose* and other archaeological marine wooden samples were analysed using a Philips Scanning Electron Microscope series 525. Core samples from the *Mary Rose* were vacuum dried. Five centimetre square samples from Somerset levels were also taken and vacuum dried. Splinters from fresh oak were taken freeze dried and then coated with gold. Samples were mounted on aluminium plates using Leit-C-Plast (carbon based cement) from Agar Scientific. Elemental maps of the samples were taken along with EDX spectra.

IV RESULTS AND DISCUSSION

IV.1 Chemical treatments

For DTPA solutions, there is instant discolouration of solution when samples containing iron species is immersed in solutions with concentrations equal to or greater than 0.1M. For solutions with concentrations 0.05M and 0.025M, it takes several minutes for discoloration to take place. The discoloration is also more intense in higher concentration solutions after the same length of treatment time. This was done visually but proper quantification using UV-Vis would be preferable. This indicates that more iron is removed in solutions containing higher concentrations of DTPA compared to lower concentrations, something that was expected. However, it was found in some cases that above a certain concentration (≈ 0.5M) the difference in the time iron extraction begins upon immersion (time it takes for orange discoloration to appear) and the intensity of the discoloration after several weeks of treatment was negligible. Samples undergoing treatment are shown in Figure 35.

This was the same for EDTA solutions except that for EDTA solutions with concentration 0.05M the time it took for iron extraction to begin was longer than for DTPA solutions with the same concentration.

Calcium phytate solutions show little or no discolouration upon immersion of samples containing iron ions but on occasion there is a white precipitate after several days of treatment. This precipitate contains high concentrations of iron and when filtered, the filtrate contains very little or no iron at all.

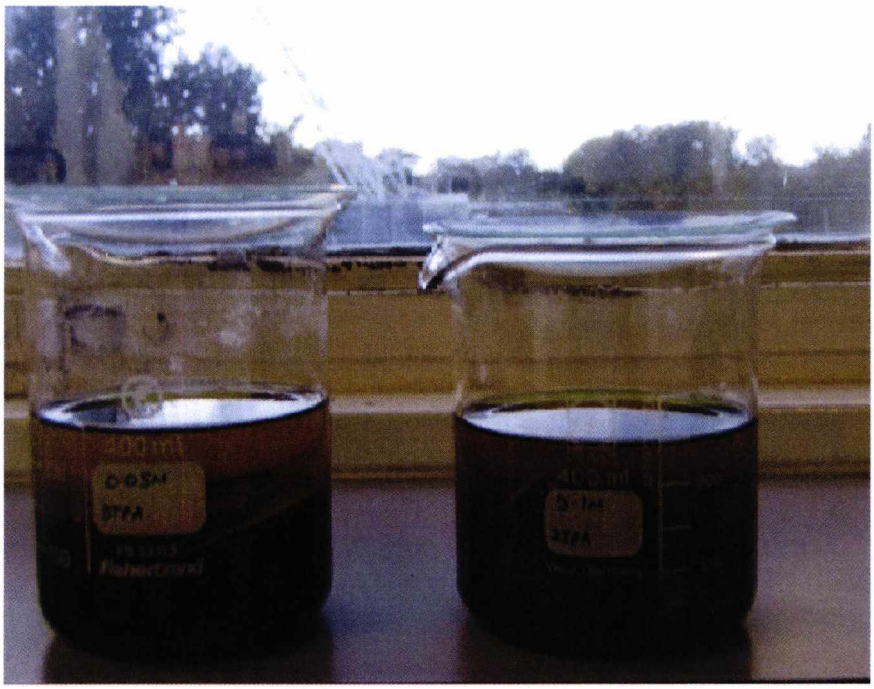

Figure 35: *Mary Rose* Sample undergoing treatment with chelating solutions of DTPA. 0.1M solution shows a more intense discoloration compared to 0.05M solution.

IV.2 Bulk XAS measurements

IV.2.1 16.5 Results

The results shown here are analysed data collected for *Mary Rose* samples at station 16.5 at the Daresbury SRS. Figure 36 shows the Fe K-edge XANES and EXAFS data collected from the samples (8 in total) prior to treatment. Figure 37 shows Fe K-edge EXAFS data for the same samples and the Fourier transform along with the best fits. The corresponding data after treatment for 1 month in solutions of various chelating agent (see Table 1) are shown in Figures 38 and 39. Each chelating agent had solutions of two different concentrations; typically 0.05M and 0.1M.

All spectra show a weak pre-edge feature (A) (Figure 36) which can be related to octahedral coordination around the central iron atoms. Tetrahedral coordination has a much stronger pre-edge feature [109]. This octahedral geometry is seen in the EXAFS as producing a primary oscillation corresponding to Fe-O shell at about 2Å. This shell can be split into 2 sub shells, each of 3 oxygens and with bond lengths of 1.934Å – 1.979Å and 2.007Å – 2.092Å, with errors of ±0.02Å for each shell fitted. The expected octahedral symmetry from the pre-edge feature was used to scale the EXAFS to take account of self-absorption effects in the measurements.

For most samples, edge position lies in the range 7124.1eV – 7125.8eV, which shows Fe^{3+} valency. The exceptions to this are the untreated samples (AB1), (AB6), (AB7) and both treated and untreated sample (AB8). These have edges in the range 7120.3eV – 7122.7eV which is closer to Fe^{2+} oxidation state. The EXAFS of these samples is also different and shows additional structure at a bond length of ~3Å. This was fitted by reference to model compound data for goethite (FeO(OH) – sample (AB9) in Figure 39), which has additional Fe-Fe shells at 3.04Å and 3.40Å, although pure goethite is Fe^{3+}.

Some of these samples exhibited heavy orange discolouration from iron corrosion products, particularly (AB8). Treatment in the first three cases, by calcium phytate (0.1M and 0.05M) and ammonium citrate (0.1M) has clearly been effective in breaking down the more complex iron oxide structure and has left the remaining iron in the timber as Fe^{3+}. Whilst sample (AB8) has

not been completely treated by soaking in 0.05M DTPA, the heavy initial contamination indicates that a longer treatment time might be necessary in such cases.

Two of the treated samples show additional features in the EXAFS and both exhibit a pronounced feature at the absorption edge (C). Without a good *priori* model to fit to the EXAFS, an understanding of the chemical structure responsible remains uncertain. However, it does suggest an Fe-O shell at approximately 2.86Å with a further shell at 4.26Å. Refinement gives a slight preference for this to be a Fe-O shell of high occupancy (9±3) rather than an Fe-Fe shell of lower occupancy (1.5±0.8). There is a suggestion that this structure is also present in the treated (AB3) and (AB4) and untreated (AB4) and (AB5) samples, indicating that it may be a second iron speciation within untreated timber and that the effect of the DTPA and ammonium citrate has been to preferentially remove other iron chemicals. These samples also show a broadening of the principal XANES line with a post-edge 'shoulder' at (C).

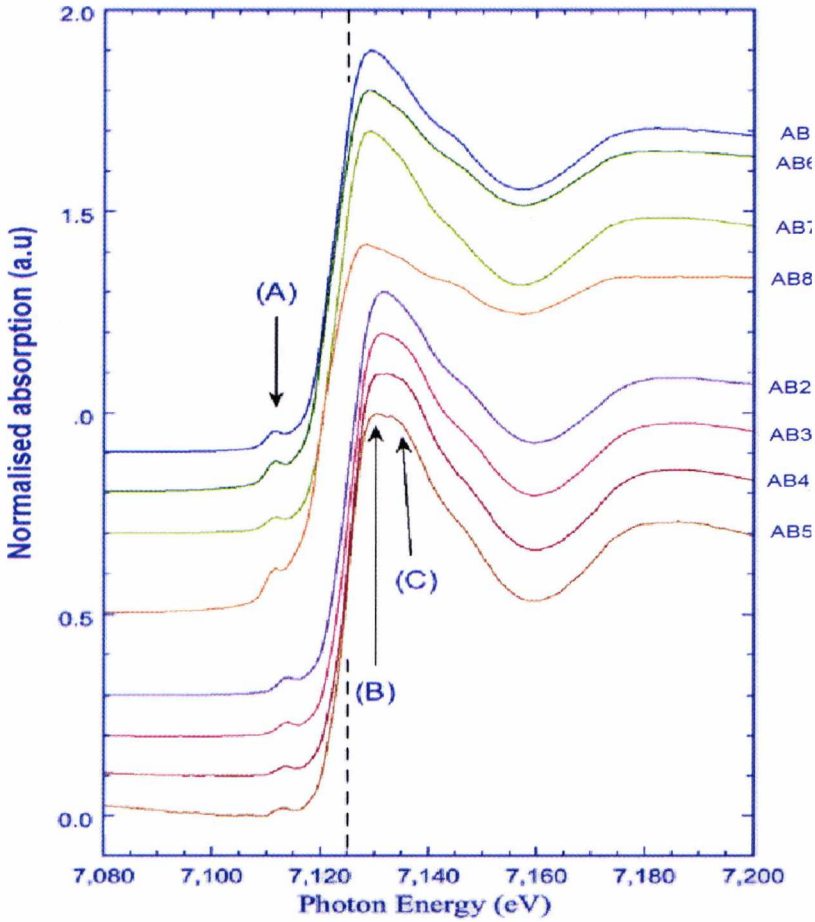

Figure 36: Fe K-edge XANES of untreated *Mary Rose* timbers. Individual plots have been shifted in the vertical for clarity. Dashed line at 7125eV indicates the position of the Fe^{3+} edge.

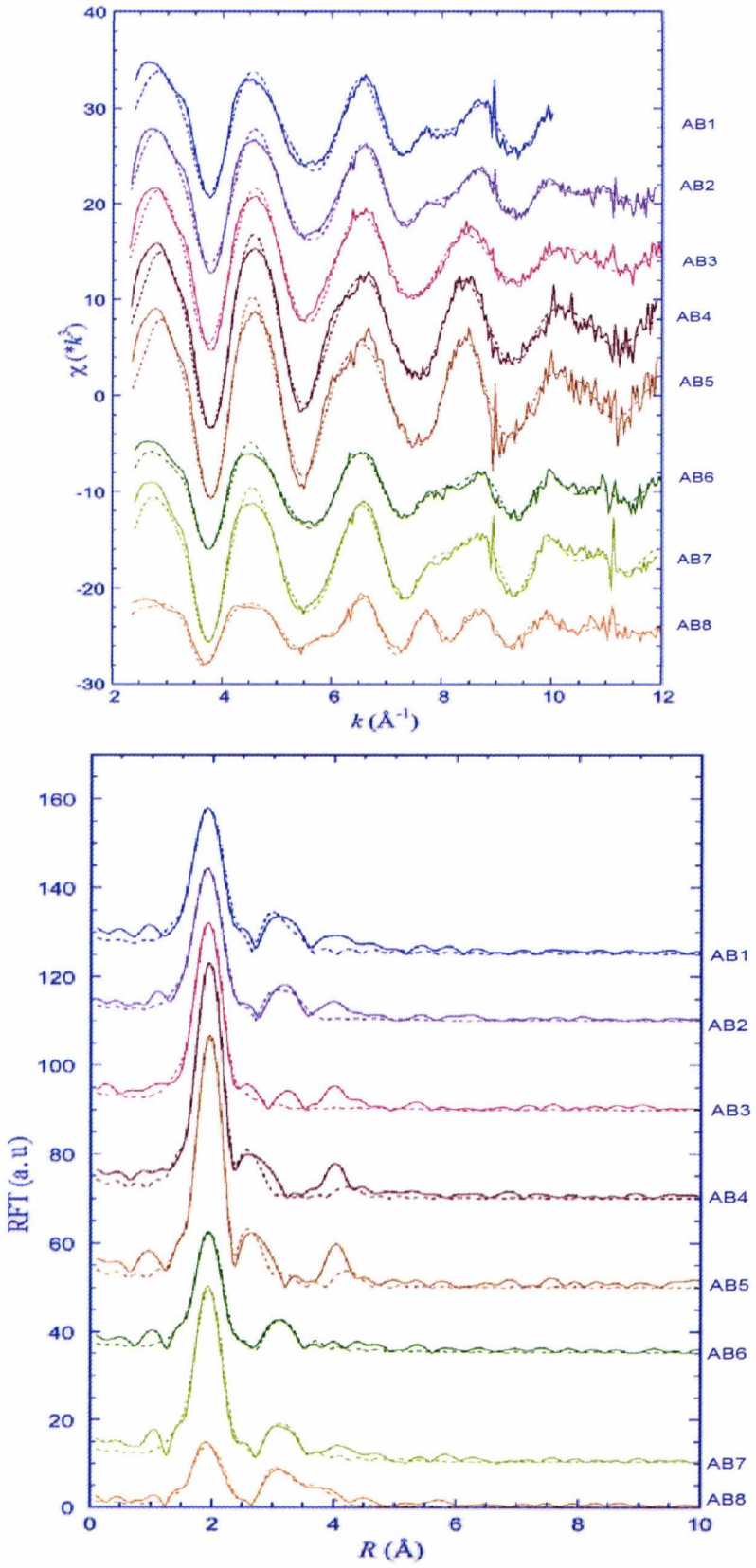

Figure 37: EXAFS of untreated *Mary Rose* timbers. Individual plots have been shifted in the vertical for clarity. Solid lines are experimental data and dashed lines represent EXAFS modelling data.

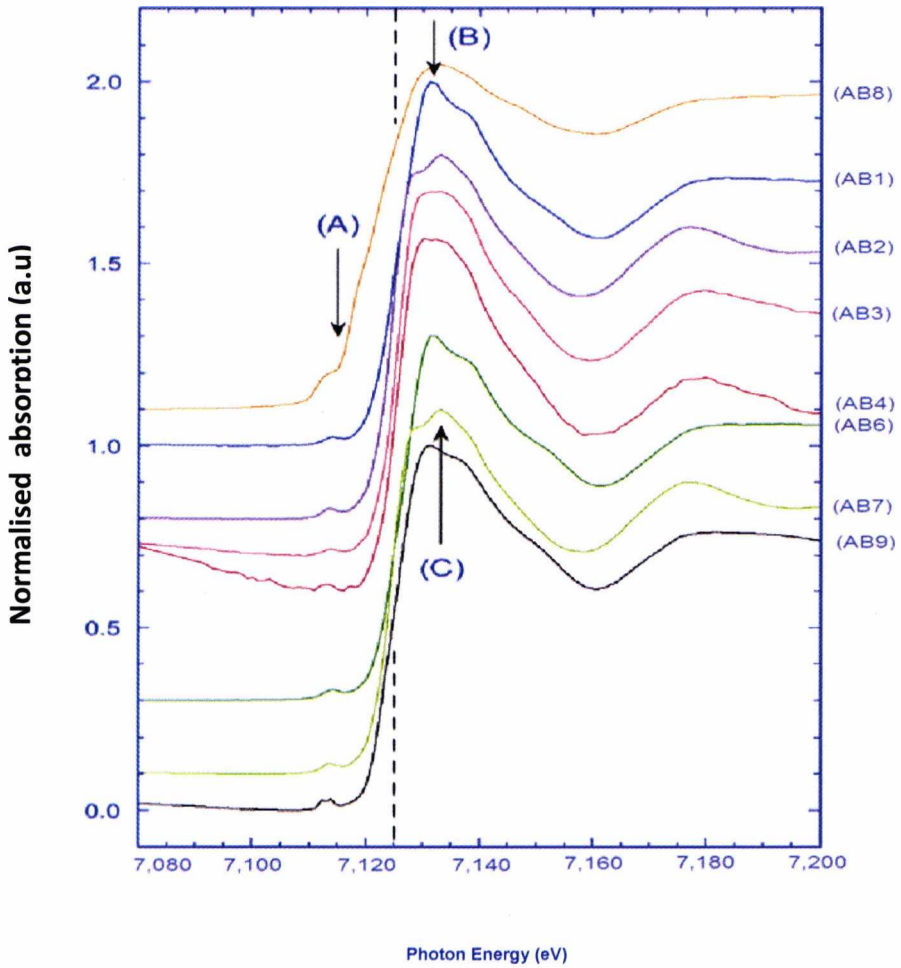

Figure 38: Fe K-edge XANES of the same samples as shown in Figure 36 after treatment by a number of different chelating agents. Dashed line at 7125eV indicates the position of the Fe^{3+} edge.

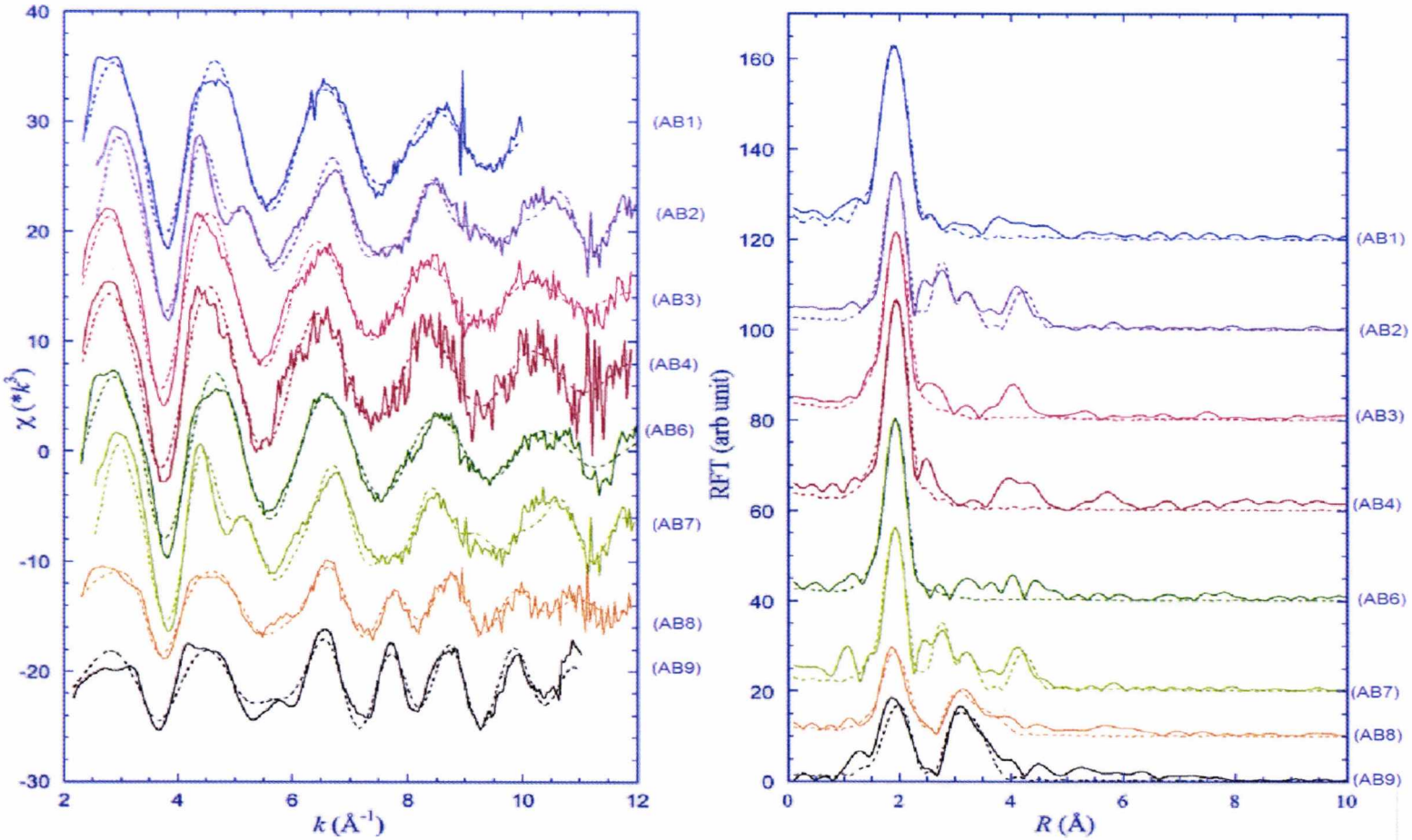

Figure 39: EXAFS of the same samples as shown in Figure 37 after treatment by a number of different chelating agents. Sample (AB9) is model compound; goethite data. Solid lines are experimental data with the EXAFS modelling shown as dashed lines.

By keeping the detection geometry constant for the XAS experiments before and after treatment, it was possible in some instances to use the edge step to do quantitative comparison of Fe content before and after treatment in the timbers. The edge step is a direct measure of the total iron content; the X-ray absorption depends on concentration of iron *via* Beer-Lambert law. For the samples treated with DTPA and EDTA, a drop in the edge step was noticed pointing to the reduction in iron content after treatment. A higher concentration of EDTA (0.1M) used gave a lower drop in edge step compared to a DTPA (0.05M). This was consistent with our observations in the laboratory. For DTPA the orange colouration that accompanies iron extraction is observed in a matter of a few seconds even when using low concentrations (~0.05M) but for EDTA higher concentration (0.2M) have to be used to observe the same rate of extraction. Examples are shown in Figures 40 and 41.

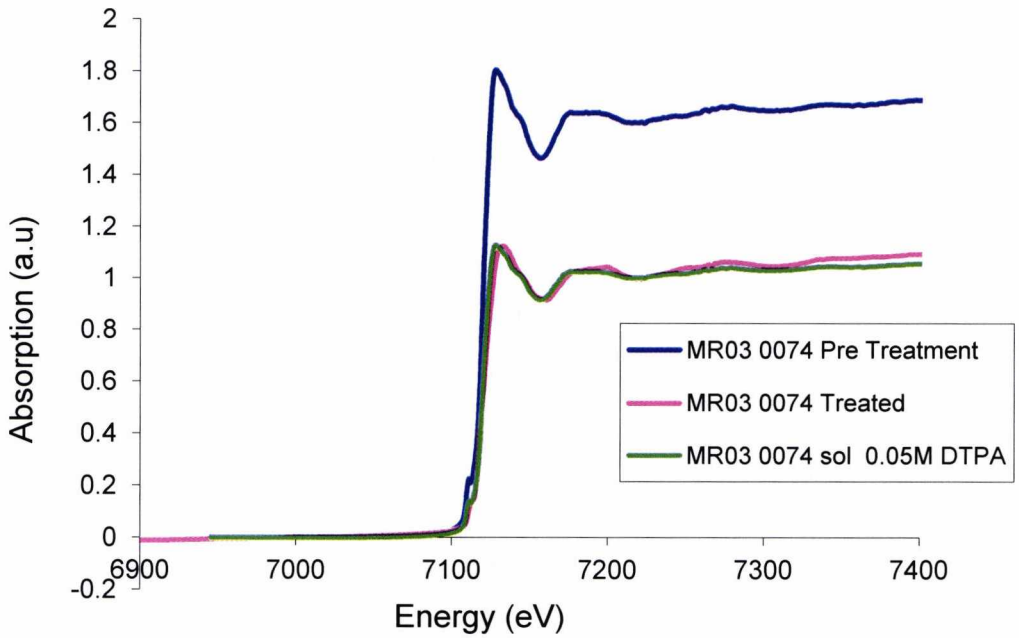

Figure 40: Fe K-edge XAS spectra before and after treatment with DTPA. The spectra were collected with the same geometry; hence the edge step depends directly on Fe concentration.

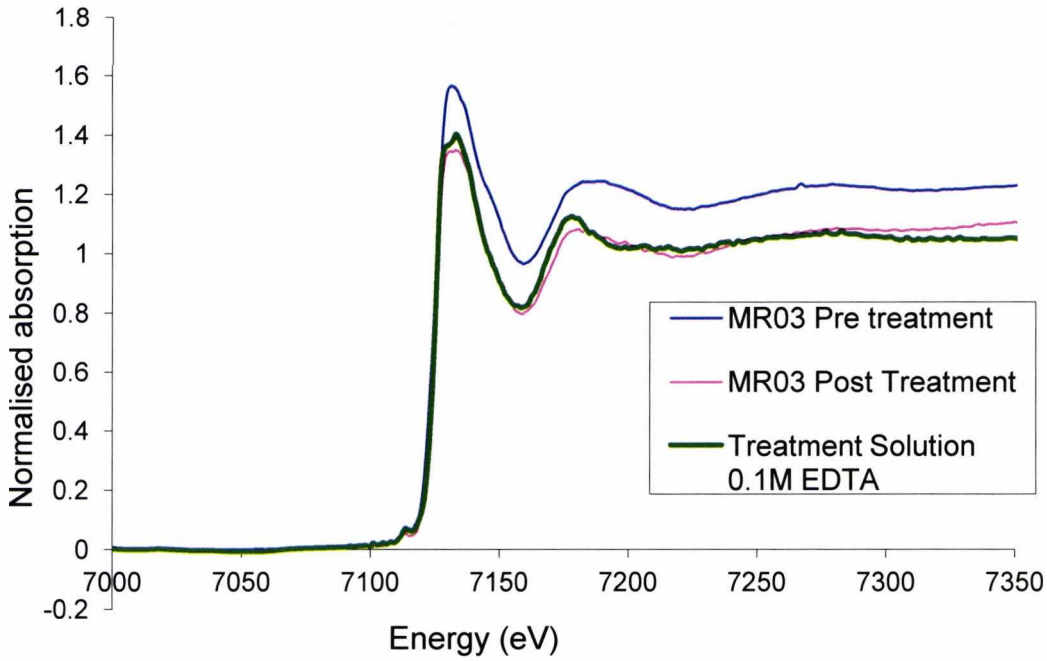

Figure 41: Fe K-edge XAS spectra before and after treatment with EDTA. The spectra were collected with the same geometry; hence the edge step depends on Fe concentration.

It is not always possible to maintain a constant geometry due to the need to optimise the fluorescence signal. For example, the detector needs to be moved further away from the sample for high concentrations to avoid saturation and moved closer at low concentrations to increase the count rate and improve the signal to noise ratio. This meant it was not possible to use the edge step to carry quantitative analysis for all the samples.

IV.3 Microfocus X-ray Experiments

IV.3.1 First Run at I18

The X-ray microprobe instrumentation at station I18 does not offer high enough spatial resolution to probe individual cells; however this is convenient for the examination of larger areas of timber samples. Additionally, it has been designed for extended range XAS studies, allowing more detailed atomic structures to be determined. Figure 42 shows a series of X-ray fluorescence images, combined with an optical microscope image of a vessel in a sample of oak timber recently raised (2004) from the *Mary Rose*. In the optical micrograph, iron mineralisation can be seen in the interior walls of the vessel and in neighbouring cells and has a characteristic orange colour. Although the spatial resolution offered by I18 is not high enough to probe individual cells, iron and sulfur concentrations and speciation can be identified over broader regions. Exploiting the technique of imaging at specific energies, characteristic of individual oxidation states (Fe^{2+}/Fe^{3+} and sulfur/sulfate) it was possible to determine the location and relative concentrations of Fe^{2+}/Fe^{3+} and sulfur/sulfate.

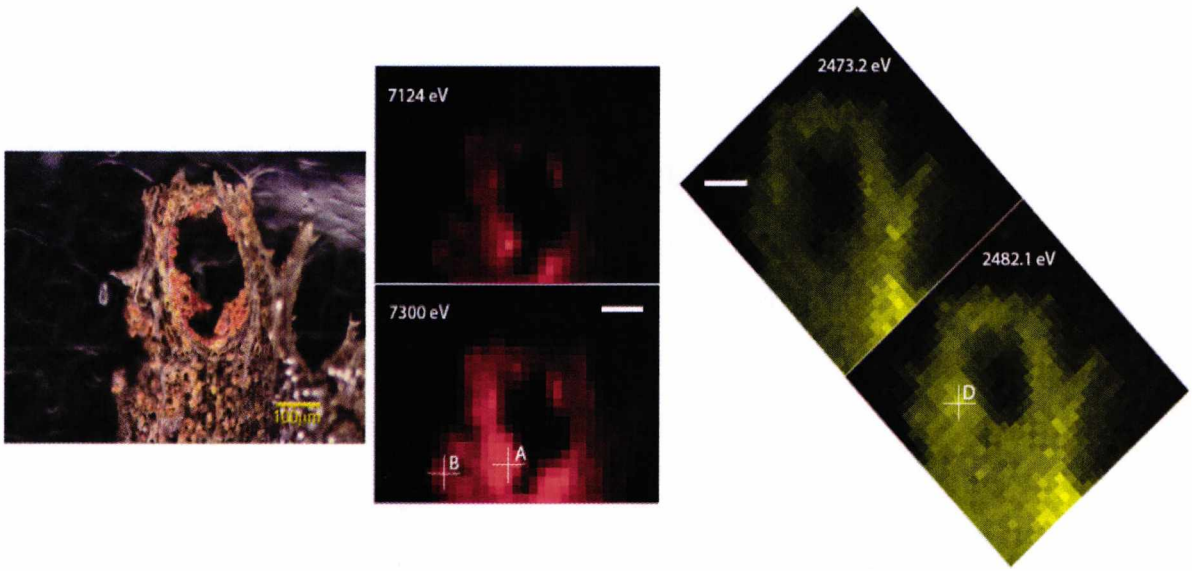

Figure 42: Optical micrograph of MRT04 (left) alongside iron (centre) and sulfur (right) X-ray fluorescence maps of same sample. The top iron map (7124 eV) shows only Fe^{2+}, whilst the lower map (7330 eV) is total Fe. Similarly the top sulfur map shows elemental S and the lower map all sulfur.

The iron present in this sample (MRT04) is clustered in the orange coloured areas observed in the optical micrograph (the inverted bottle-shaped hole is clearly visible in all the maps and was used as a marker) and is mainly of Fe (III) valency. The sulfur valency maps show that in the region of iron mineralisation the sulfur is principally sulfate, whereas in the iron free areas it is reduced sulfur. This was the first time that the co-location of iron minerals and sulfate had been confirmed in waterlogged archaeological wood.

This is confirmed by the XANES analysis on the sample and this is consistent with the expected results for a timber sample that has been for long periods in a moist oxidising environment.

Fe XANES from locations 'A' & 'B' in MRT04 (see Figure 42) were compared to standard iron oxide spectra, and this is shown in Figure 43. A visual inspection of the XANES spectra suggests a goethite like structure. Most of the iron species present are in the +3 oxidation state with the Fe species detected in spot A having a mixture of Fe^{2+} / Fe^{3+} oxidation states. A weak pre-edge feature at 7115eV is characteristic of the atomic coordination; strong feature is indicative of tetrahedral; small (weak) pre-edge feature found here suggests octahedral coordination around the Fe atom.

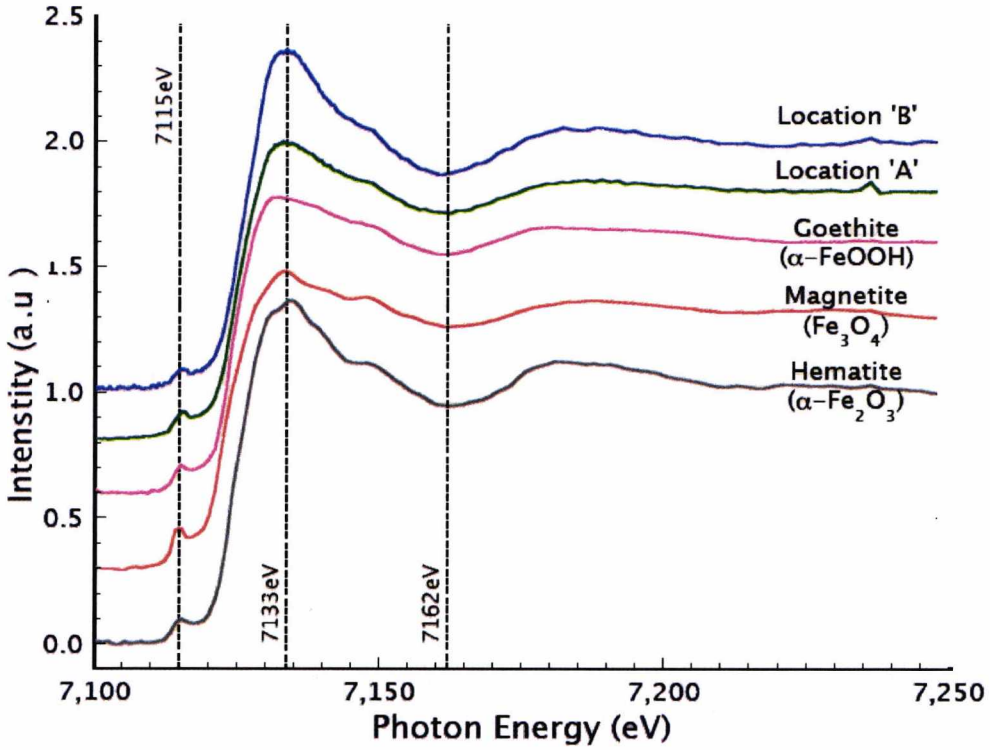

Figure 43: Stacked XANES plot of MRT04 at two different locations (A&B) compared with some standards.

Analysis of the Fe K-edge EXAFS data of the iron in the mineralised region can be fitted to a goethite like structure (α-$Fe^{3+}O(OH)$). Data from locations A and B were combined (to get a better understanding of the iron speciation across the sample) and compared with model compound data collected from beamline 16.5 at the SRS and the predicted theory for goethite. The results of this are summarised in Figure 44 and Table 4 and show a good fit. Figure 44 shows the Fourier transform of the results and Table 4 presents the best fits from EXCURV98. It was impossible to fit the oxygen expected at 3.209A. This is due to the limited scattering expected from this single oxygen atom and the dominance of the Fe shells at a similar distance. The Debye Waller factor was set at 0.01Å for the *Mary Rose* sample MRT04 and not refined to allow for a better representation of fit.

Analysis of the *Mary Rose* sample also shows a noticeable reduction in the number of iron atoms at radial distances of ~3.3Å and beyond. This could reflect a lack of longer range organisation in the iron oxidation that has

developed in the wood vessel; similar effects have been reported elsewhere in the literature for iron hydroxide growths [109].

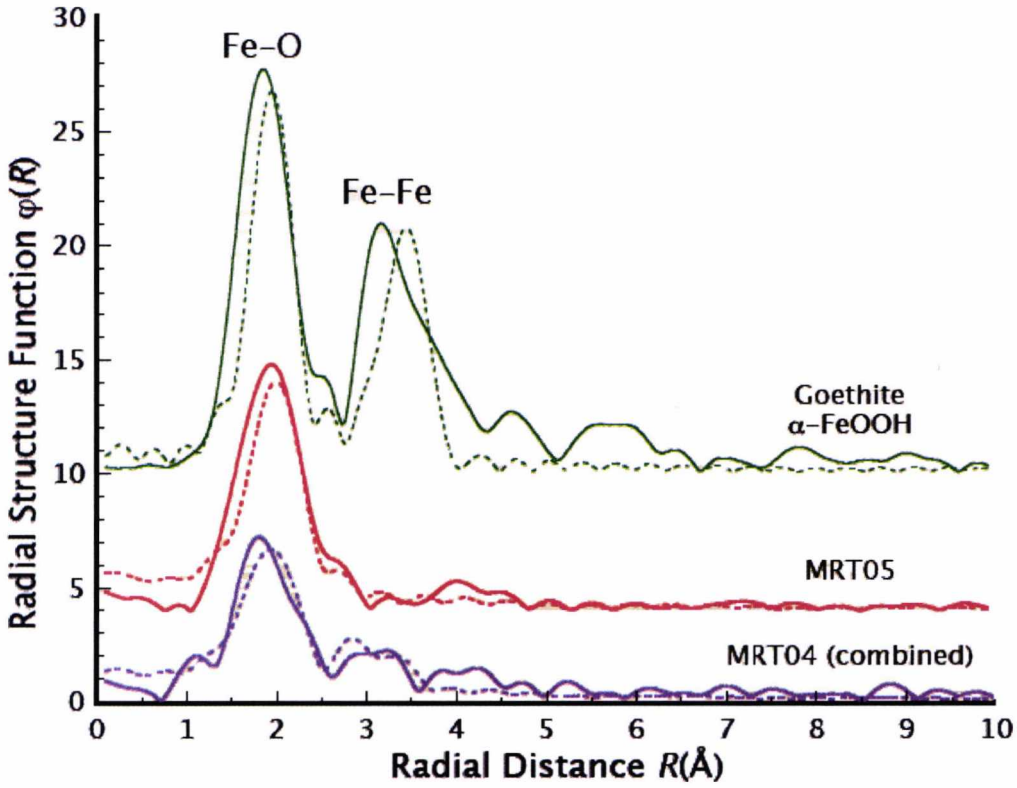

Figure 44: Fourier transform of goethite model and standard compared with MRT05 and MRT04 spot A and B combined. The solid lines are the raw data and the dotted lines are the best fits with parameters given in Table 4.

Table 4: Fits to the results of the Fe K-edge EXAFS.

	Goethite model (XRD)		Goethite standard			*Mary Rose* MRT04 (A+B)		
Atom	**CN**	**RD/Å**	**CN**	**RD/Å**	**A/Å^2**	**CN**	**RD/Å**	**A/Å^2**
O	3	1.956	3	1.951	0.01	3	1.927	0.01
O	3	2.106	3	2.095	0.01	3	2.089	0.01
Fe	2	3.018	2	3.022	0.01	2	3.017	0.01
O	1	3.209	1	3.671	0.02		–	-
Fe	2	3.311	2	3.273	0.01	1.3±0.7	3.39	0.01
Fe	4	3.438	4	3.427	0.01			
			R = 32.03			**R = 34.20**		

CN: coordination number; RD: radial distance; A: Debye Waller factor. R is percentage error on overall fitting.

Sulfur XANES collected on the sample revealed an elemental sulfur peak at 2472.2 eV and the results are shown in Figure 45. This was slightly shifted above this energy possibly due slight oxidation. There is also a sulfate peak observed at 2482.1 eV for spot D and also a slight sulfate peak was observed for spot C. This sulfate peak at spot D coincides with the Fe^{3+} for the same spot in the iron XANES. As mentioned before this is the first time such a clear correlation has been observed in marine archaeological wood samples. This lends weight to the theory of the iron catalysed oxidation of sulfur species into sulfuric acid.

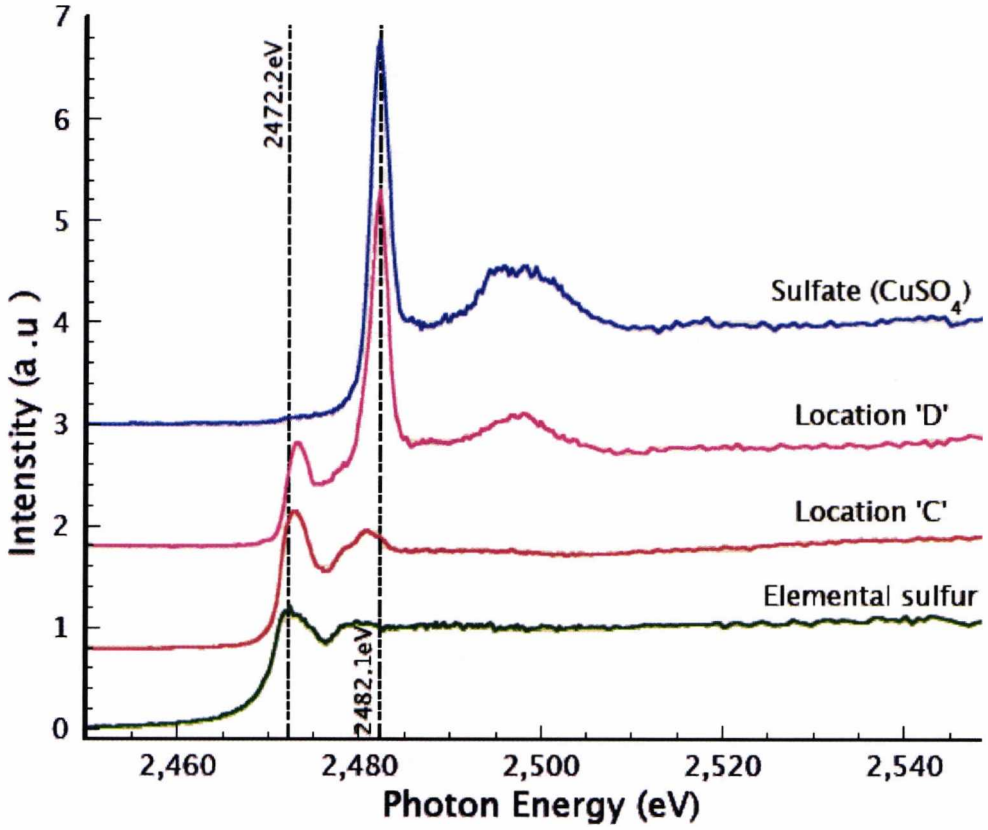

Figure 45: Sulfur XANES of MTR04 compared with elemental sulfur and copper sulfate.

It was not possible to take XAS measurements for treated samples due to time constraints but measurement of the treatment solutions were taken and analysed. Results of these compared to iron standards are found on Figure 46. 0.05M DTPA, 0.1M DTPA and 0.1M Am Cit all lie between the Fe^{2+} and Fe^{3+} edge positions showing the extraction of a mixture of Fe^{2+} and Fe^{3+} into solution by these chelating agents. 0.1M phytic acid lies on the Fe^{3+} edge position showing a possible preferential extraction of Fe^{3+} species from the samples. This may also be due to the oxidation of iron once complexed by phytic acid.

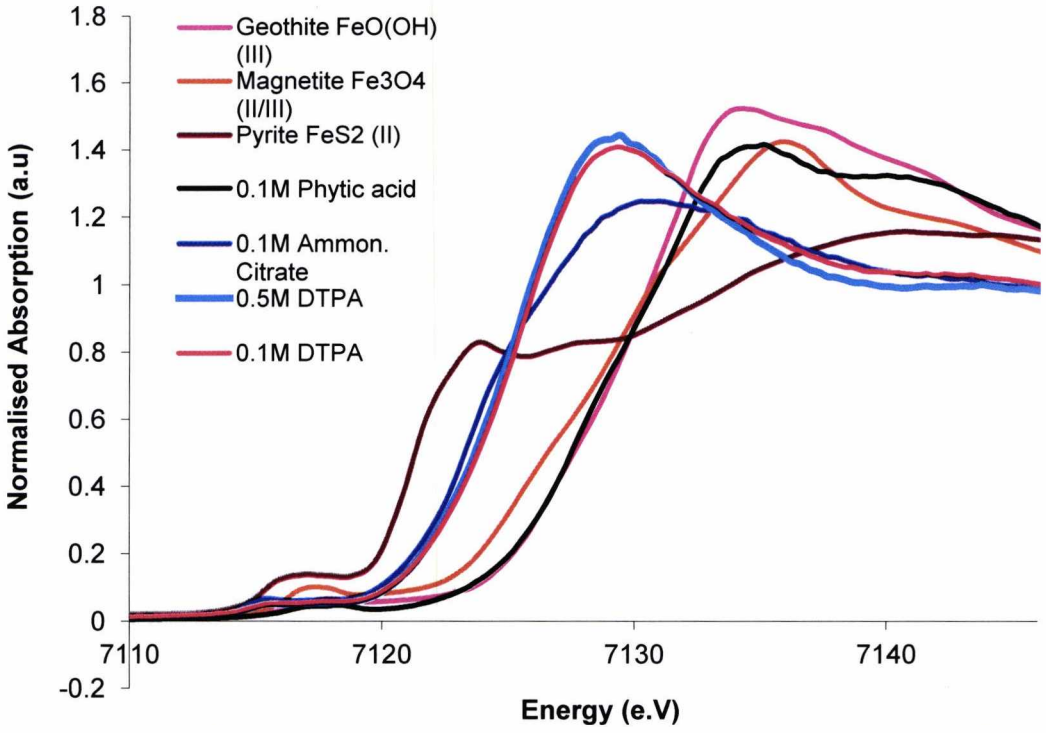

Figure 46: XANES of iron standards and treatment solutions of chelating agents.

IV.3.2 Second Run at I18

The aim of these experiments was to compare untreated timbers with matching timbers that had been treated in a solution of a chelating agent for four weeks. A table of samples and the treatments used are given in Table 3. The samples were mostly MRT04, a port side plank raised in 2004, and were similar in composition. An optical micrograph of a typical sample is shown in Figure 47. The experiments were concentrated on timbers that had been treated with calcium phytate solution or with diethylenetriaminepentaacetic acid (DTPA), a standard chelating agent used widely to complex iron. Data were collected for samples before and after treatment.

Sulfur XANES were collected and the results are shown in Figure 48. In this figure the plots have been normalised to the same edge step. Analyses showed that the sulfur species present in sample MRT04 were mainly sulfates with some elemental sulfur (slightly oxidised). There is clear elemental sulfur peak around 2475 eV and a small sulfate peak around 2484 eV for both the treated and untreated samples (see Figure 48). Untreated

MRT04_AB1 showed a pre-edge feature around 2473 eV which disappears after treatment with 0.05M calcium phytate. However, the XANES showed no major change in the sulfur content after the treatment. S K-edge XANES analyses of iron rich areas of MRT04_AB1, shown in the XRF map in Figure 49 gave similar results but with higher sulfate peaks for points D and E. Sulfur speciation at point A is mainly elemental sulfur, as seen in Figure 50.

XAFS data and valency maps were also collected from different timbers from the *Mary Rose* at the iron K-edge. Both calcium phytate and DTPA treatments were effective in removing iron from the samples, the latter being the more efficient. This was obvious from the chemical analysis conducted at Kent and from the reduction of the Fe K-edge XAS signal after treatment.

The results presented here are for timber MRT04_AB2. The optical micrograph of a sample from this timber used in the iron analysis is shown in Figure 51. This sample had been treated with an aqueous solution of 0.25M calcium phytate. This treatment did remove the orange encrustations that are commonly found in the samples. X-ray fluorescence (XRF) maps of the same sample are shown in Figure 52. Maps were collected at two incident X-ray energies; at 7124 eV which reveals the Fe(II) in the sample, and at 7300 eV which reveals the total Fe(II) and Fe(III)in the sample. The maps shown in Figure 52 have been treated to show the individual Fe(II) and Fe(III) maps. It can be seen that the bulk of the iron is present as Fe(III), which would be expected from this sample as it was taken from near the surface of the timber and had been exposed to air and moisture.

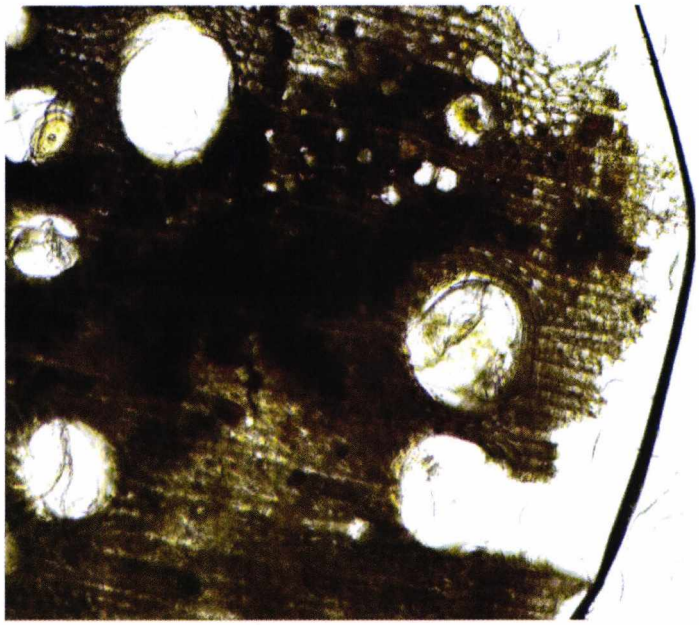

Figure 47: An optical micrograph of MRT04_AB1U

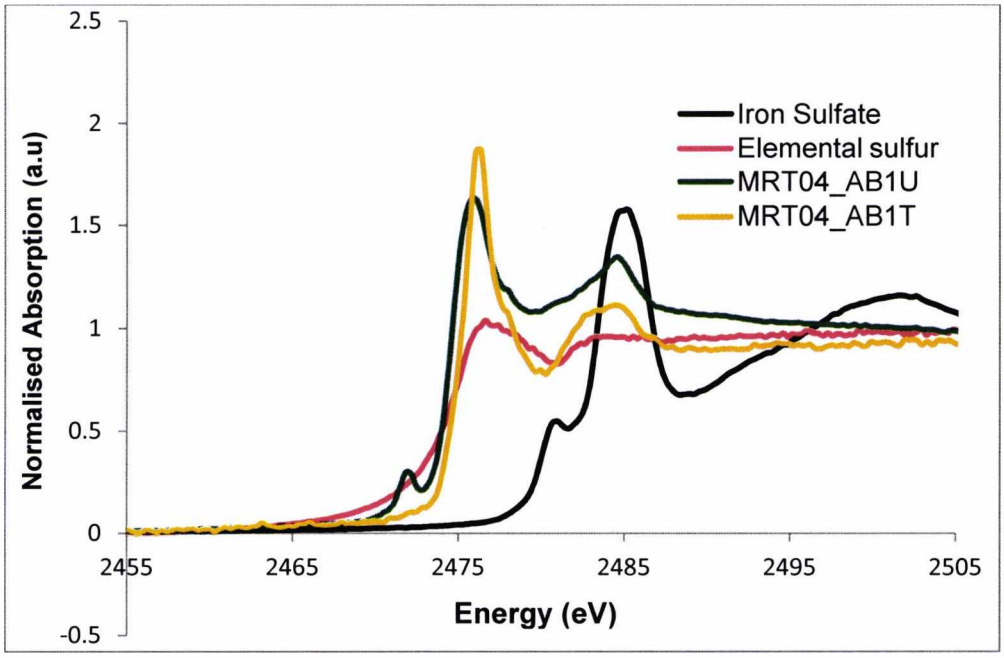

Figure 48: Sulfur K-edge XANES of MRT04_AB1 treated and untreated compared with standards.

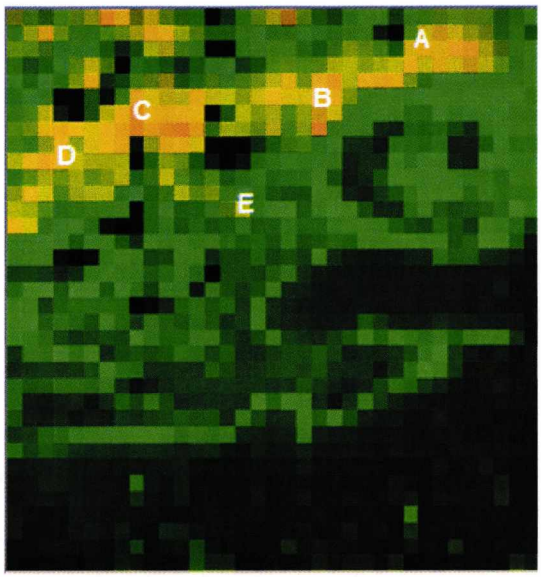

Figure 49: XRF Map showing total sulfur content of MRT04_AB1U (yellow spots show iron rich area)

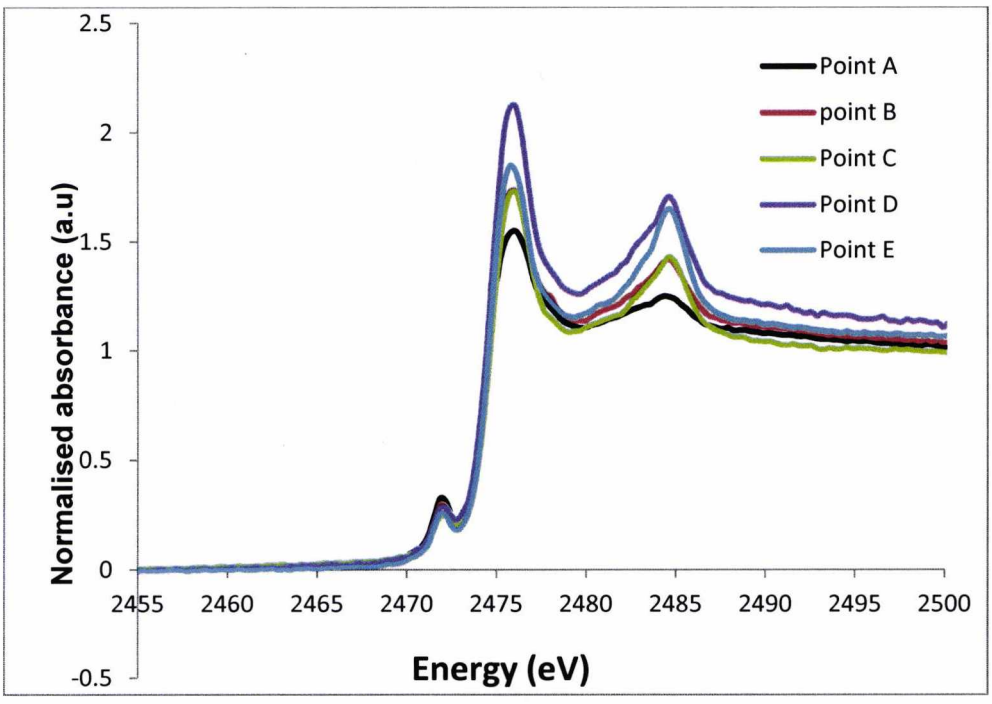

Figure 50: Sulfur XANES of MRT 04 AB1U at different points (see Figure 49).

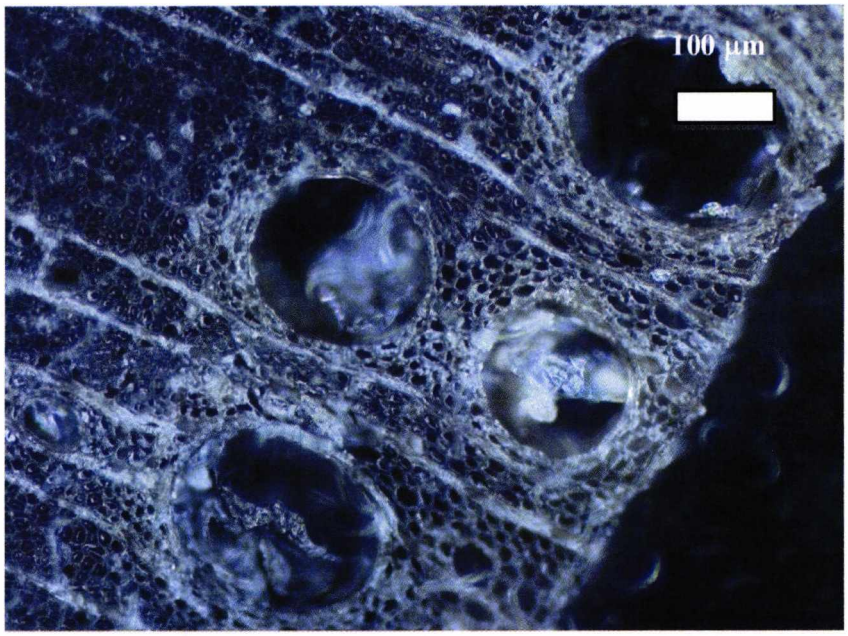

Figure 51: An optical micrograph of a wood sample after treatment with an aqueous solution of 0.25 M calcium phytate.

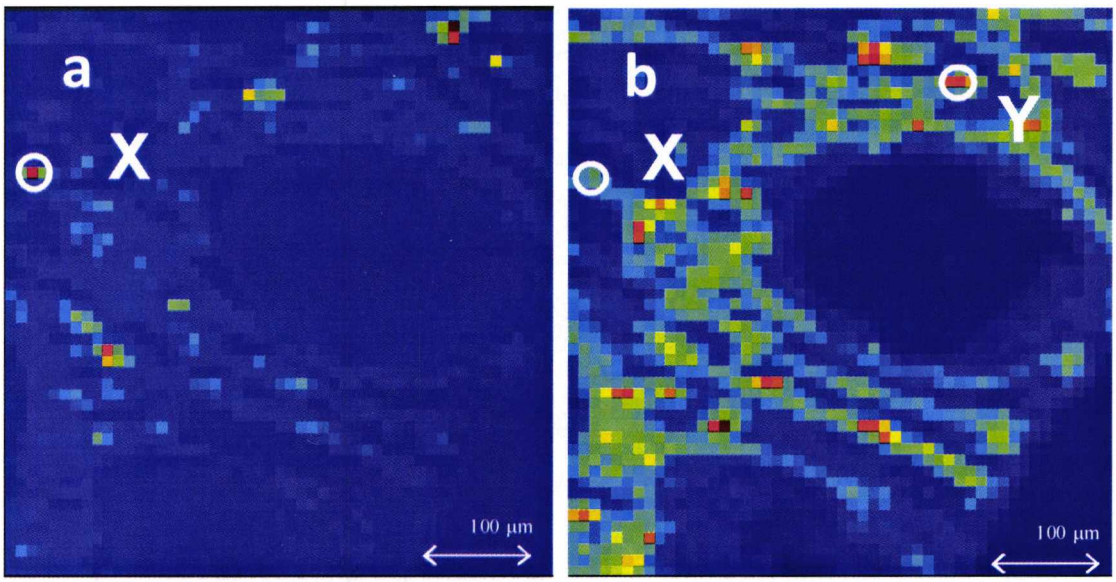

Figure 52: XRF maps of the sample shown in Figure 51; (a) map for the Fe(II) content and (b) map for Fe (III) content. (Blue is low concentration and red is high concentration.)

Fe K-edge XAS scans were collected at several points across the sample. The region being probed in a scan is ~5 × 5 microns. The points were selected based on the Fe content and position in the structure (cell wall, mid lamella, etc.). Figures 53 shows the XAS data at points X and Y in the sample and the positions are indicated in Figure 52. Point X is a region where there is a high concentration of Fe(II), whereas point Y has a high concentration of Fe(III). The differences in the concentrations of Fe are clear in the spectra, Y>X. .What is not clear from the figure is that there is a difference between the XANES regions. However, a detailed analysis shows that point X is rich in Fe(II) and point Y is rich in Fe(III). The normalised absorption plots for the spectra in Figure 53 are shown in Figure 54. In both cases the plots show only a single dominant sine wave oscillation. The Fourier transforms (not shown) gave only a single shell at ~ 2 Å due to an octahedron of O atoms.

Similar results to those described above (i.e. optical micrographs, XRF and XAS maps) were obtained for a number of samples (before and after treatment) and at Fe and S K-edges. Fe K-edge XAS spectra were also collected for the solutions used in the treatment of the wood. The results can be summarised as:-

- The bulk of the Fe in the untreated samples is present as Fe(III) with small inclusions of Fe(II).
- The bulk of the S in the untreated samples is present as sulfate (i.e. S(VI)).
- Both DTPA and calcium phytate are effective in removing Fe from the wood, the former being the more efficient.
- The Fe species, both Fe(II) and Fe(III) are in an octahedral environment with a shell of six O atoms at ~ 2 Å.

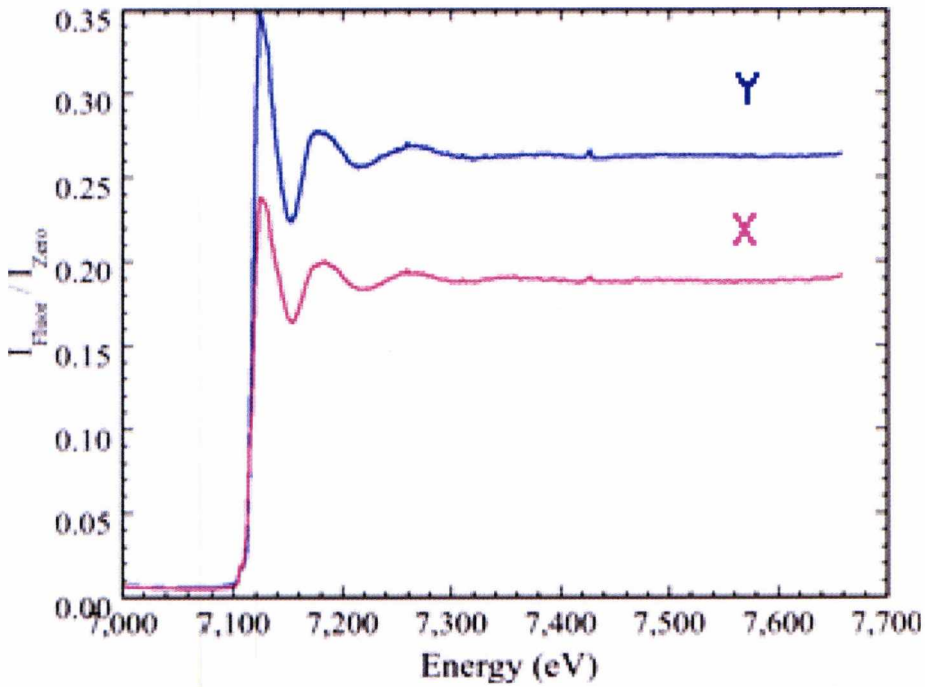

Figure 53: Raw fluorescence Fe K-edge XAS spectra from points X and Y on Figure 52.

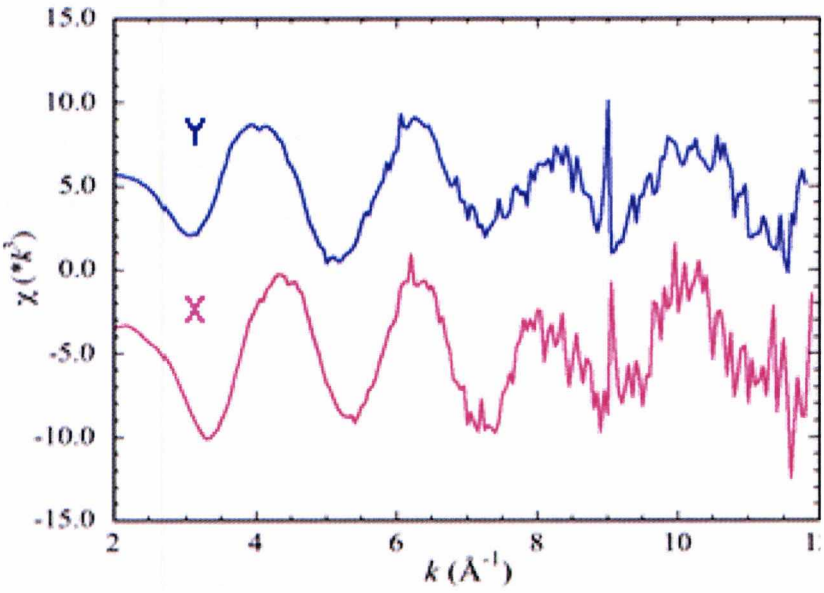

Figure 54: Normalised absorption from points X and Y on Figure 52.

During this run at Diamond laboratory XRF measurements of the samples were also carried out before and after treatment with the solutions of the chelating agents. The measurements were carried out at I18 Diamond Light Source on a Fischerscope® X-ray fluorescent system. Measurements were taken from three different locations on each sample and the average counts used. All the samples used were treated with various concentrations of calcium phytate.

The optical image of the sample in the Fischerscope is shown in Figure 55.

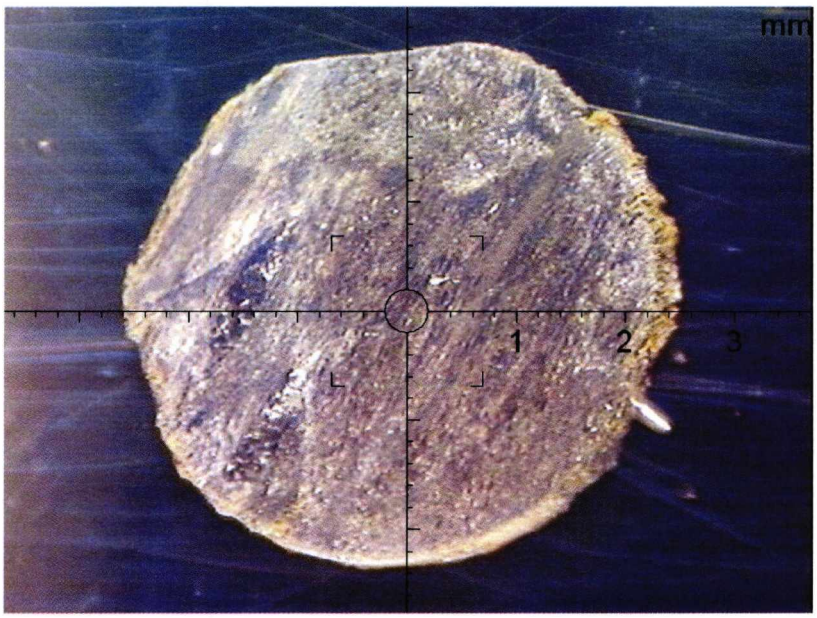

Figure 55: Sample of *Mary Rose* timber undergoing XRF analysis in a Fisherscope X-ray fluorescence machine.

The results are listed in Table 5 below. The results show a clear reduction in the total iron counts in the treated samples compared to measurements taken prior to treatment. For sample MRT04_AB1 treated with 0.5M calcium phytate, there was a drop in average iron count from 154.0 (before treatment) to 57.4 (after treatment) a drop of 62.7%. Sample MRT04_AB2 was treated with 0.25M calcium phytate and showed a reduction of average iron count from 214.4 (before treatment) to 91.1(after treatment), which is a drop of 57.5%. Sample MRT04_AB3 was treated with 0.45M calcium phytate and gave a reduction in average iron count from 1274.0 (before treatment) to 248.0 (after treatment), an 80.5% reduction. Since the number of counts is directly proportional to the concentration of iron in the sample, it can be safely deduced that the calcium phytate solutions are effectively removing iron from the samples. The results are summarised in Table 5 and Figure 56.

Table 5: Laboratory XRF results before and after treatment with calcium phytate.

Sample	Average number of counts/sec		% drop	Treatment solution
	Before Treatment	After treatment		
MRT04_AB1	154.0	57.4	62.7	0.5M Cal. Phy.
MRT04_AB2	214.4	91.1	57.5	0.25M Cal. Phy.
MRT04_AB3	1274.0	248.0	80.5	0.45M Cal. Phy.

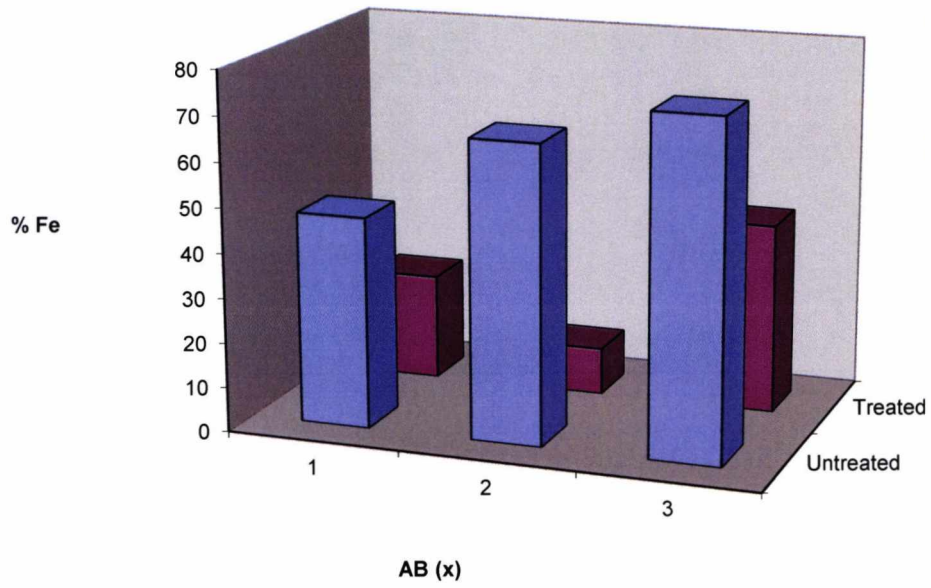

Figure 56: The percentage iron contents of pre treatment and post treatment of *Mary Rose* samples with calcium phytate.

IV.3.3 Third Run at I18

The focus of this run was the arrowhead described in the experimental Section III.3.3.

SEM and optical microscopy images were collected of thin sections of the arrowhead wood after microfocus X-ray experiments. These are shown in Figures 57 and 58, respectively. The SEM image shows large clusterings of pyrite nanoparticles, which can be seen to be collecting particularly on the walls of the larger vessels in this section. Close inspection of the optical image showed the gunmetal grey colouration of pyrite clusterings along with a few small patches of an orange coloured iron corrosion phase. There is no evidence of the cellular voids being filled with PEG, although it should be noted that core sections of oak, taken from the ship's hull only shows PEG filling cell voids if there is an open pathway (e.g. a crack) into the body of the timber through which the PEG can flow in sufficient quantities to fill the cells completely [110].

As on previous XAS runs model spectra of a variety of iron compounds were collected and they are shown in Figure 59. This shows a shift towards higher photon energy of the absorption edge (the steep rising edge in the absorption spectrum) with increasing valency. Iron metal; Fe(0) has the left-most edge with an absorption edge, defined as the maximum in the gradient of the rising edge, of 7114.6 eV. The Fe^{2+} species, such as wustite (FeO) and the iron sulfides, pyrite (FeS_2) and marcasite (FeS_2) have a leading edge at about 7120.8 eV, whilst the Fe^{3+} oxides (hematite (Fe_2O_3), geothite (FeO.OH)) have edges at approximately 7129.0 eV. Magnetite (Fe_3O_4) has mixed $Fe^{2+;3+}$ valency, the Fe^{3+} dominates the edge, but a lower energy shoulder can be seen due to the Fe^{2+} contribution. Key features to note are the peak of the Fe^{2+} resonance which is marked with an A in the figure at 7120 eV, this contrasts with the Fe^{3+} feature marked with a B (7137.0 eV). It can be seen that the various model Fe^{3+} oxide species show distinctly different features on this peak, these arise because the model compounds are of well defined oxide species with specific local atomic structures. Iron oxides species seen in the *Mary Rose* timbers do not usually show this degree of fine structure.

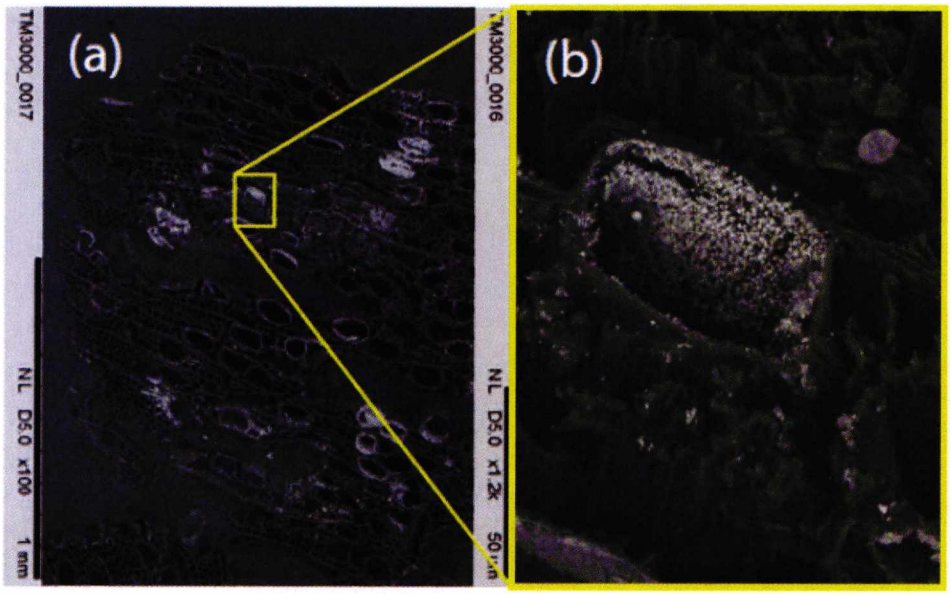

Figure 57: SEM images of thin section of arrow tip from the *Mary Rose*. (a) low magnification image of section, (b) high magnification close up showing pyrite nanoparticles lining the walls of a vessel.

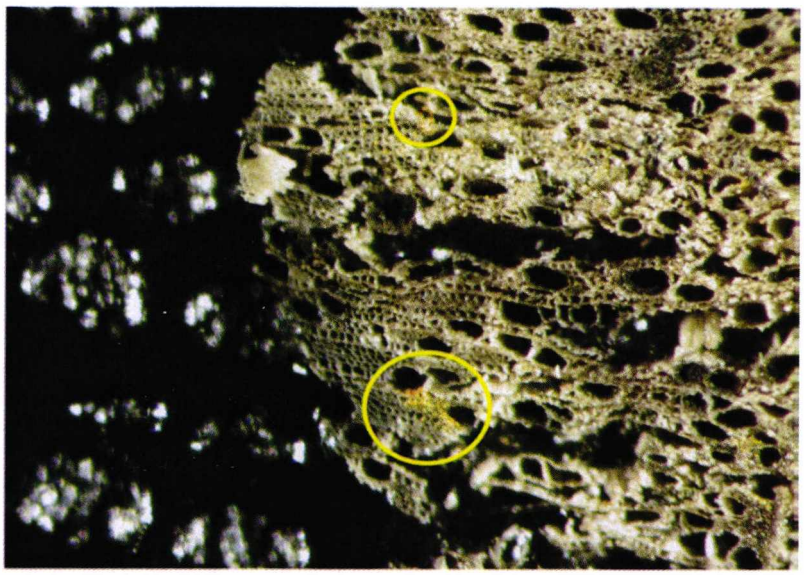

Figure 58: Optical micrograph of the section. Iron corrosion products typically have an orange colour are only seen in moderation in this section (circled).

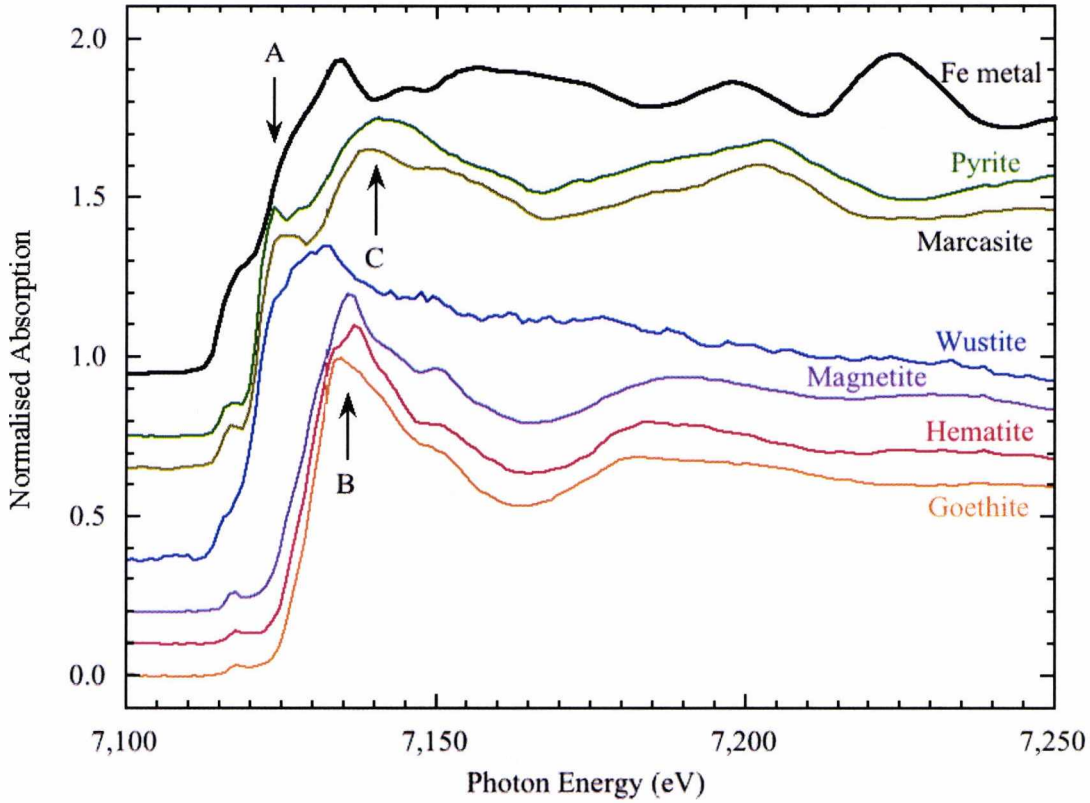

Figure 59: A selection of Fe K-edge XANES spectra of iron standards.

It suggests that they are less well formed in the timbers than model compound, a point that was discussed earlier in the attempts to fit the EXAFS of iron oxide in the timber to the goethite structure. This peak does not coincide with the broader hump seen at around 7140 eV (C) in the two iron sulfide spectra.

Figure 60 shows a selection of Fe K-edge XANES spectra taken of the conserved arrow tip, but prior to treatment with DTPA. This shows a significant fraction of pyrite like structures, particularly at point (1) which gives a spectrum very similar to the model compound iron sulfide data of Figure 59, although locations (4) to (7) also show a feature at about 7120 eV (A) which is related to the sulfide Fe^{2+} signature seen in Figure 59. Measurements from (6) and (7) show maxima at 7133 eV, which corresponds more to an Fe^{3+} oxide and occurs at a slightly lower energy than the maxima seen at (1),(4) and (5), suggesting that spectra from these latter locations is dominated by sulfide content, whereas (6) and(7) represent a more mixed

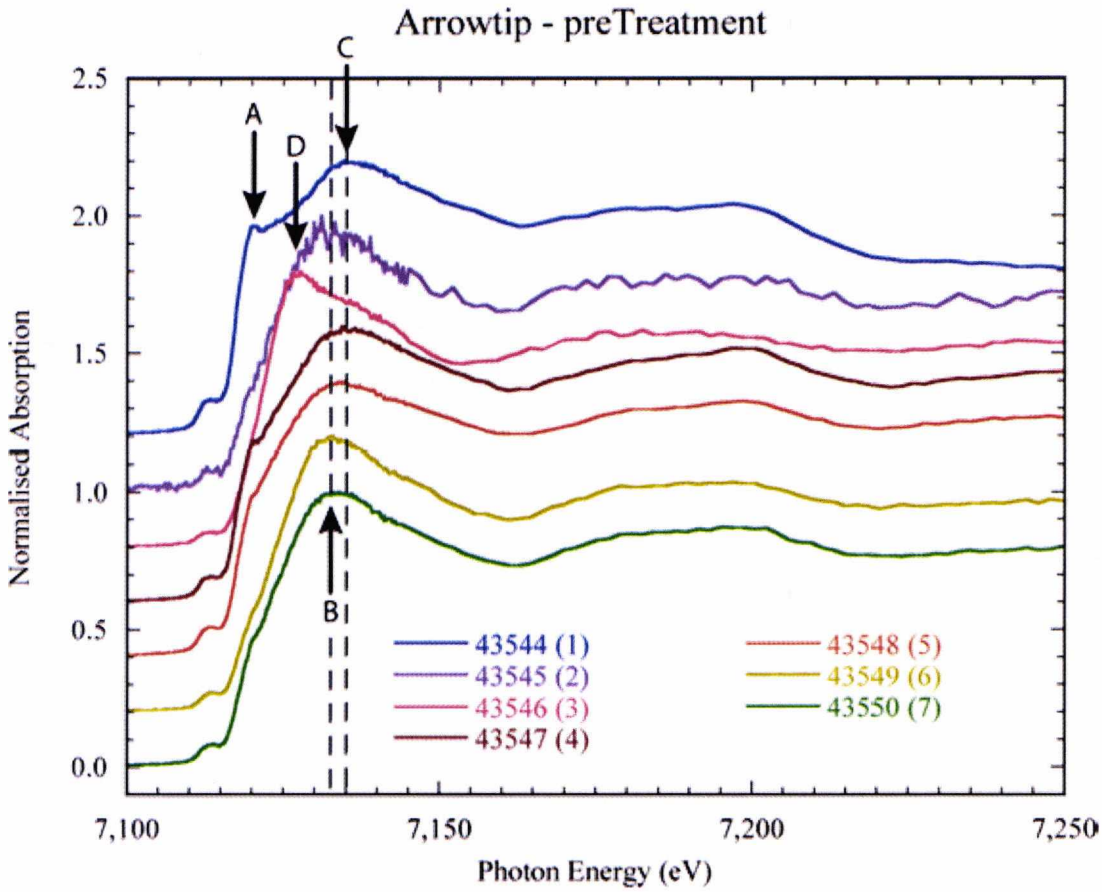

Figure 60: Fe K-edge XANES spectra from seven locations within the section of the arrow tip, taken before treatment with DTPA.

environment of iron sulfide and oxide. Spectra from locations (2) and (3) do not show any sulfide like structures and appear more oxide like, although (7) represents a more mixed environment of iron sulfide and oxide. Spectra from locations (2) and (3) do not show any sulfide like structures and appear more oxide like, although of different types. Spectrum (2) has a maximum at 7133 eV and is predominately Fe^{3+}, whereas spectrum (3) has a maximum at 7127 eV (D) which implies a Fe^{2+} valency.

The XRF map area of the sample is shown in Figure 61. This was collected at 7300 eV and reveals the total iron concentrations in the region. An optical image of the sample is shown in Figure 62 and like the SEM image in Figure 57 it shows that the sample contains some areas with heavy concentrations of pyrite nanoparticles. Near the edges of the sample, a higher proportion of iron oxide is seen.

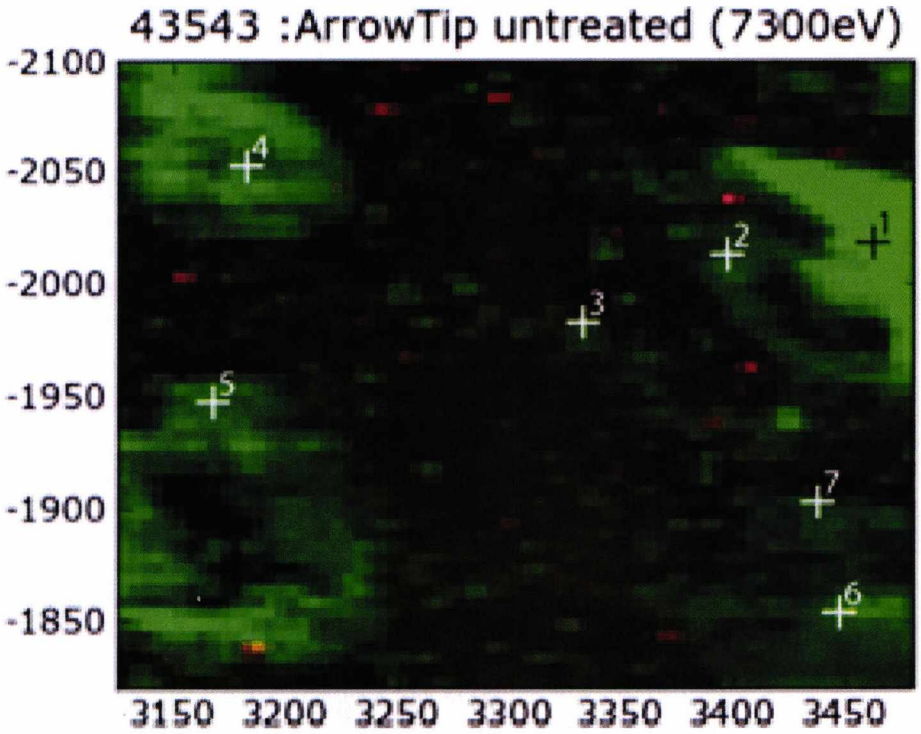

Figure 61: A Fe XRF map collected at photon energy of 7300 eV of the iron content in an area 275 µm by 350 µm, marked with the locations from which the individual XANES spectra were collected.

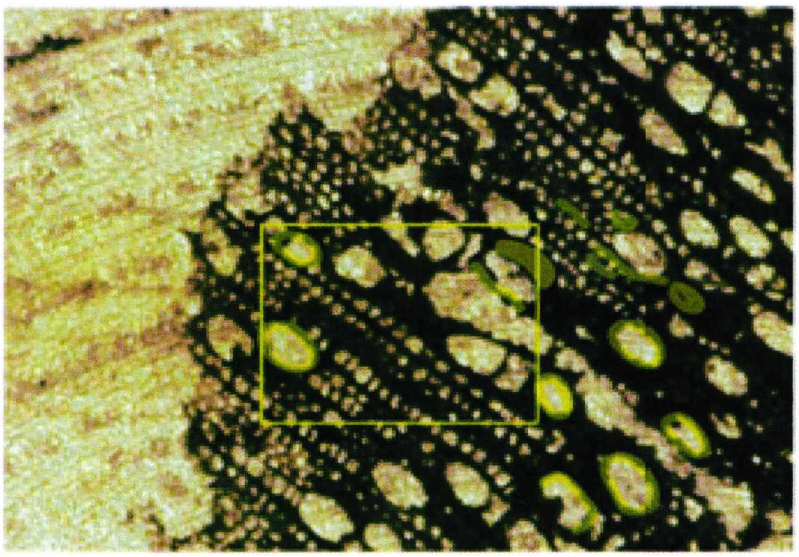

Figure 62: An optical micrograph of a section of the arrowhead. Areas of high pyrite concentration as seen in the SEM images of Figure 57 are highlighted in yellow.

The thin section was then soaked in a solution of 0.1 M DTPA overnight. This did not induce much change in the iron content of the sample, neither did there appear to be significant uptake of iron by the solution; i.e. there was no obvious colour change of the solution. Treatment of a PEG treated core sample from the ship's hull timbers produced a similar, unchanging response. In contrast, as reported earlier, other timber samples from the *Mary Rose* which had not been PEG treated produced strong and rapid changes, indicating that DTPA is normally effective in removing iron from waterlogged archaeological marine timbers.

Figure 63 shows Fe K-edge spectra taken from a range of locations, in approximately the same area as before. The iron XRF map is shown in Figure 64 and a SEM image of the region is shown in Figure 65. An attempt was made to correlate the areas studied with those seen in the SEM, bearing in mind the slight changes in topography due to sample movement between the two measurements. The iron fluorescence signal is approximately unchanged, indicating that the DTPA has not been effective in removing iron from this sample (removal rates of between 40% and >99% are observed in non-PEG treated samples; see the SAMBA results in the next section). With the exception of location (6) (which appears to be an Fe^{3+} oxide) the spectra all show close similarities to that of the iron sulfide model compounds.

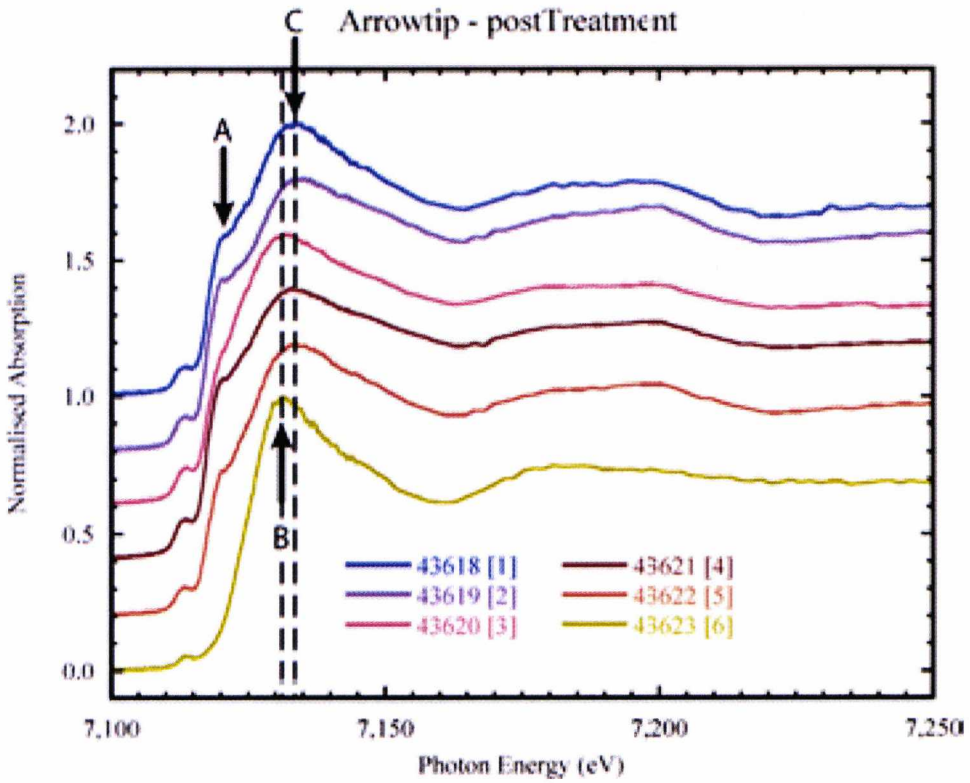

Figure 63: Fe K-edge spectra from six locations within the section of the arrow tip, taken after treatment with DTPA.

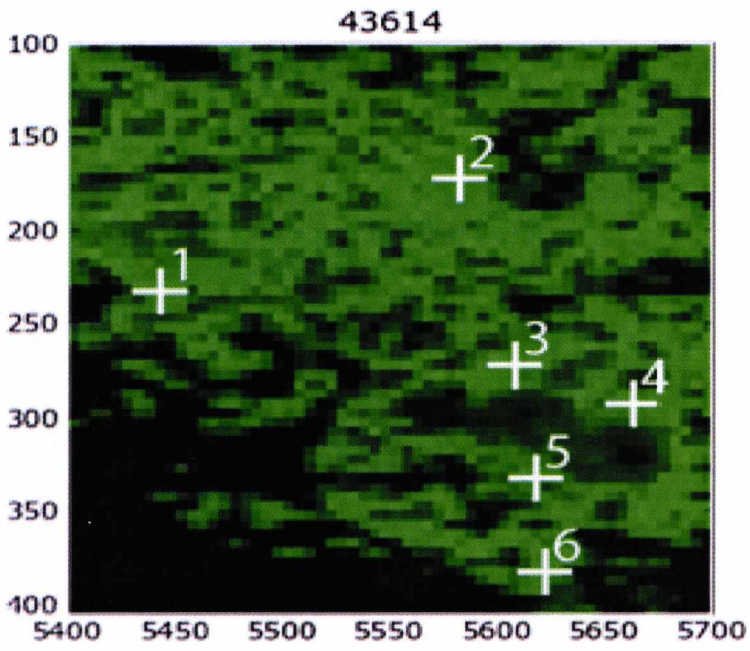

Figure 64: An XRF map collected at photon energy of 7300 eV of the iron content in an area 300 µm by 300 µm, after treatment with DTPA. The locations are marked from which the Fe K-edge XANES individual spectra were collected.

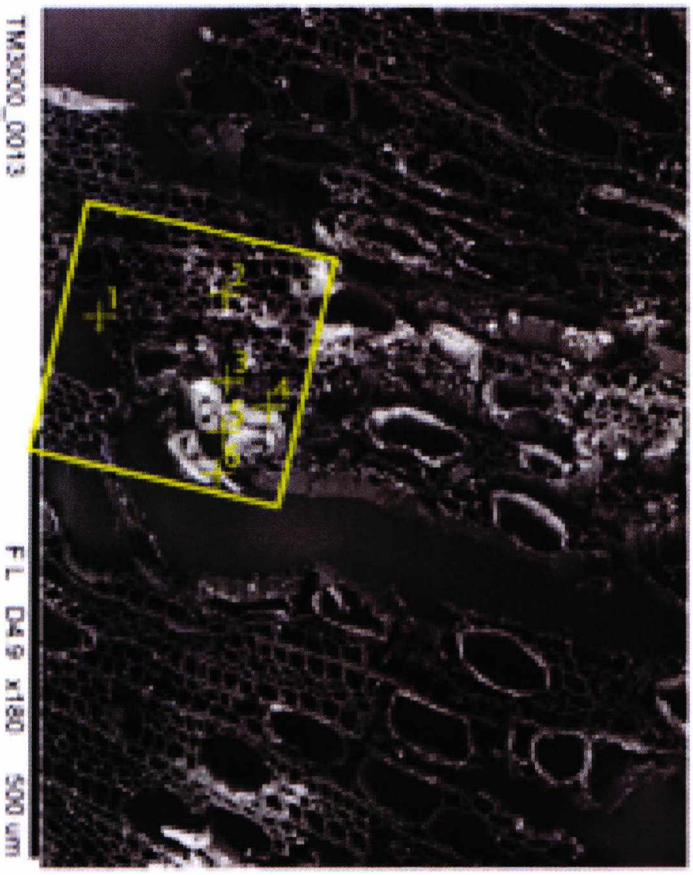

Figure 65: The corresponding area of the XRF map (Figure 64) on an SEM micrograph.

Switching the beamline to operate at the sulfur K-edge allowed data to be collected on the sulfur speciation within the section, however due to the complexities in changing the beamline operation, it was only possible to measure the sulfur after the treatment with DTPA. Figure 66 shows spectra collected from 6 locations within a map area of 300 μm by 200 μm. Three XRF maps were collected, at incident photon energies of 2469.5 eV, 2473 eV and 2482 eV and these are shown in Figure 67. These correspond to the sulfide, organo-sulfur/elemental sulfur and sulfate resonances, respectively and in principle allow strong variations in these chemical speciation to be distinguished. Due to the ability of the beamline to transmit higher order radiation, it proved possible to map for sulfur and iron content at the same time.

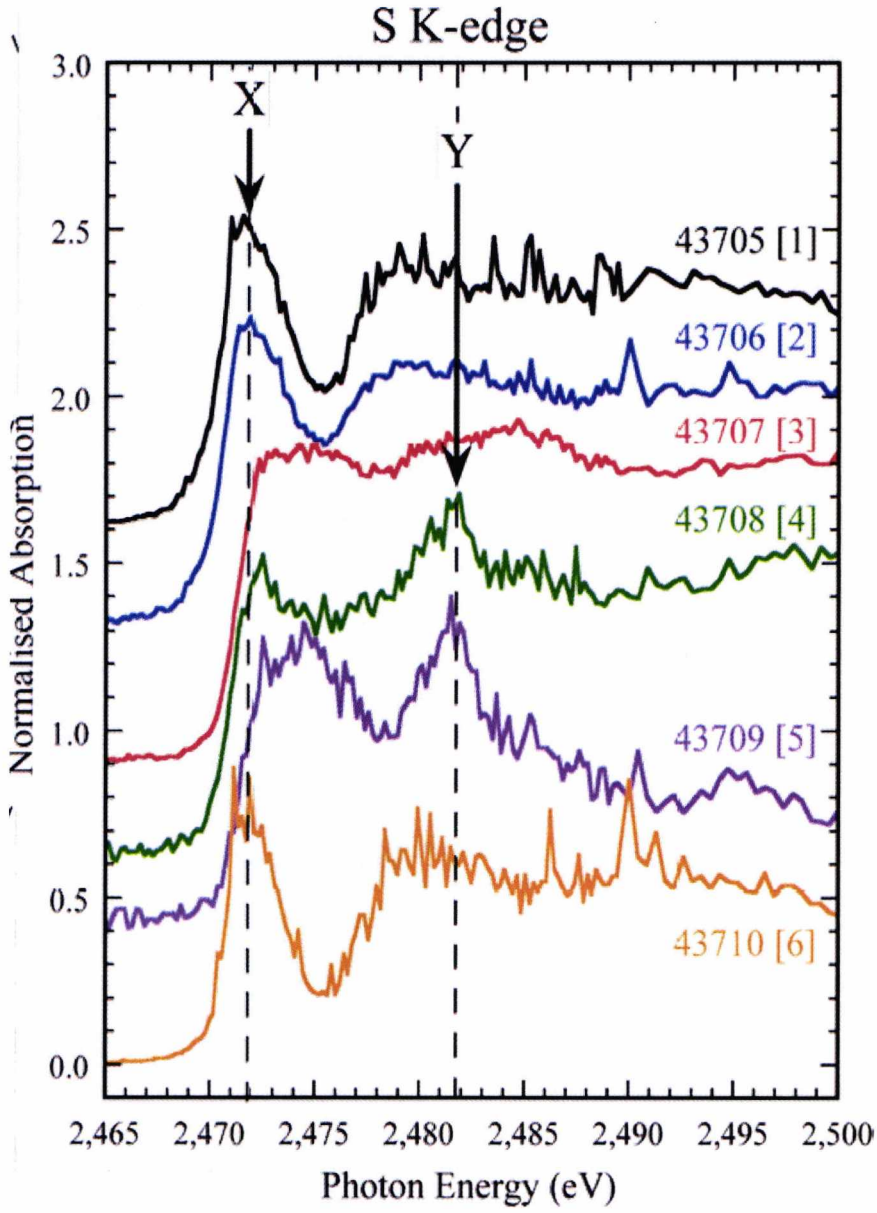

Figure 68: S K-edge spectra from six locations within the section of the arrow tip, taken after treatment with DTPA.

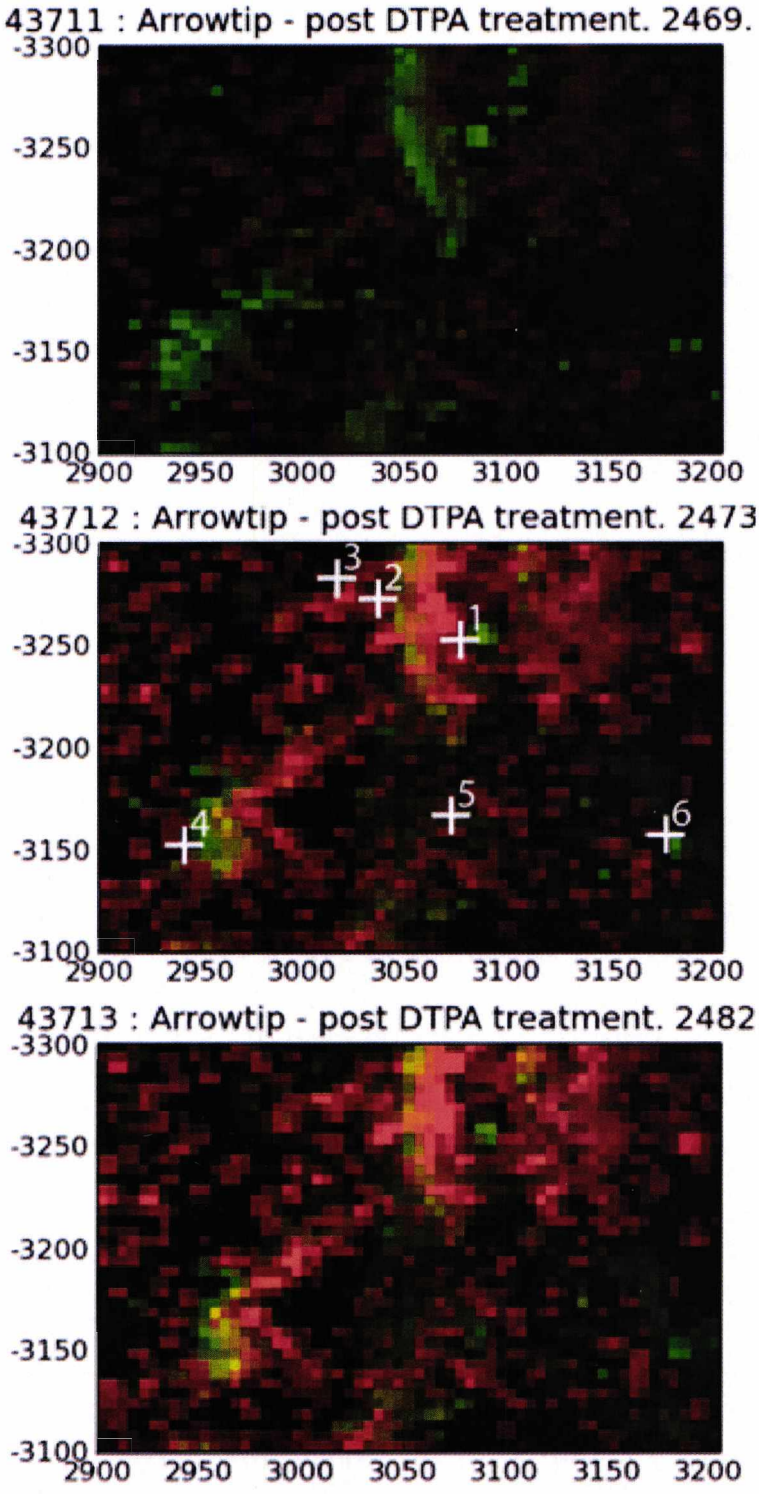

Figure 67: XRF maps collected at photon energies of 2469.5 eV, 2473 eV and 2482 eV in an area 300 µm by 200 µm, marked with the locations from which the individual spectra were collected. In the maps, red indicates the relative sulfur content, green is the iron content.

In these maps the sulfur concentration is coloured red, whilst the iron content is green (as in the other XRF maps presented here). The XRF maps suggest that there is little sulfide present in the imaged area, this is confirmed by the spectra collected from 6 locations across the mapped area and shown in Figure 66. The presence of sulfide (S^{2-}) would be evident by a peak at approximately 2469 eV in the sulfur XANES. The 6 spectra show a variety of other features; spectra [1], [2] & [6] show a peak centred at 2471.8 eV (X in Figure 66), corresponding to elemental sulfur (S0), whereas spectra [3], [4] & [5] show an absorption edge shifted to slightly higher energy. This suggests a slightly oxidised form of sulfur, such as an organo-sulfur species. Additionally, spectra [4] and [5] show a peak at 2482 eV (Y) which is related to sulfate (S^{6+}), although the percentage of sulfate is small. The iron concentration in the mapped area is largely confined to two areas and it is possible that the region of the section that was studied at the S K-edge does not correspond to that measured at the iron edge. The SEM (Figure 57) does show that the pyrite contamination only occurs in certain locations within the arrow tip and it is possible that the area selected for sulfur K-edge analysis did not correspond well to the previously selected region.

During this run the treatment of the PEG impregnated samples from *Mary Rose* with various concentrations of two chelating agents (DTPA and calcium phytate) was investigated using the Fischerscope® laboratory XRF. The samples are shown in Figure 68. The treatment was overnight for all the samples. The results can be summarised as follows:-

- Visual observations revealed that the action of the treatment solutions on the PEG impregnated samples are slower compared to the non-impregnated samples. For non-impregnated samples the orange colour that accompanies the formation of Fe-ligand complex is observed in under a minute upon immersion of samples. In the PEG impregnated samples this colour is not observed after several minutes and some cases, not at all.

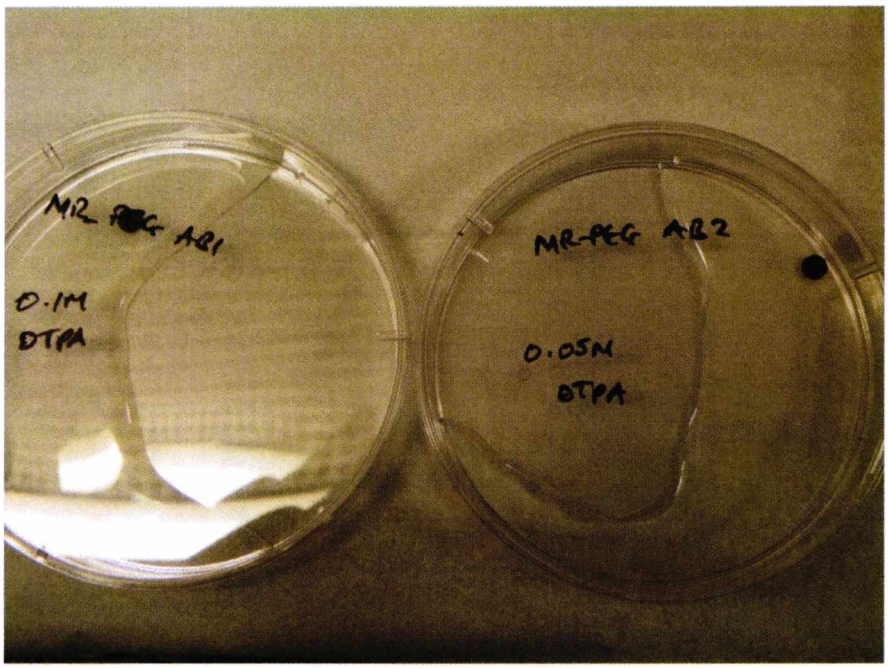

Figure 68: The PEG impregnated samples undergoing treatment.

- XRF analyses of samples before and after treatment showed that although the treatment solutions have an effect on the samples they do so to a lesser extent compared to the non-impregnated samples. In these analyses the number of iron counts per second in the sample spectrum before and after treatment was used

For the PEG samples there was a 23% drop in the Fe counts per second in the samples before and after treatment compared to 78% in the non PEG impregnated samples. As explained in the introduction PEG is used as a consolidant in the wood to plug holes in the timbers left behind by the damage of cells. This prevents the wood from shrinking and cracking when dried. It seems that this also prevents the treatment solution free access to iron species like pyrites in the wood. PEG in this instance is affecting the diffusion process and rate of the chelating solutions in the timbers. The results are summarised in Table 6 and Figure 69.

Table 6: Iron XRF analysis of the treatment of PEG impregnated wood.

Sample	Average number of counts/sec		% drop	Treatment solution
	Before Treatment	After treatment		
MR PEG_AB1	188.1	149.9	20.31	0.1M DTPA
MR PEG_AB2	229.9	147.5	35.84	0.05M DTPA
MR PEG_AB3	242	205	15.29	0.1M Cal Phy
MR PEG_AB4	220.3	173.8	21.11	0.05M Cal Phy

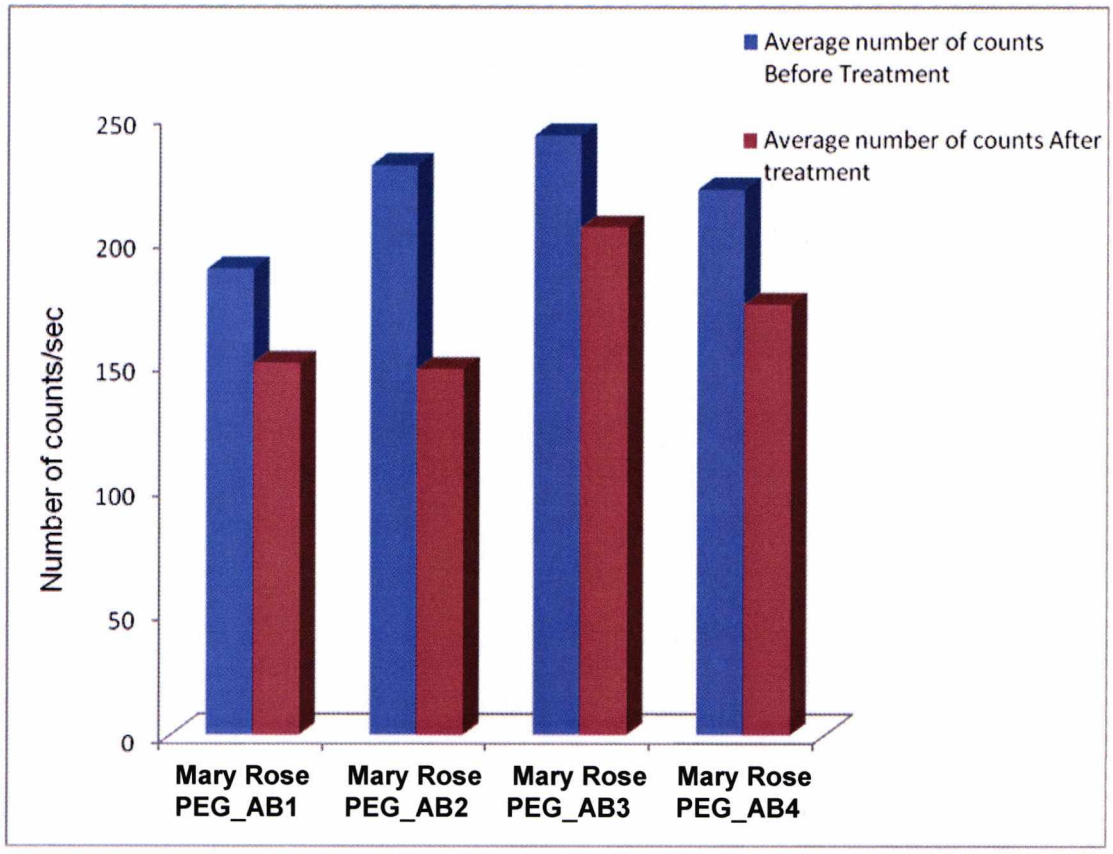

Figure 69: The graphical representation of the results in Table 6.

IV.4 Bulk XAS at Soleil station SAMBA

It is unnecessary to show the raw data for these runs as the results are best represented as concentration of iron species in the wood and the solutions. Using linear combination the percentage ratio of Fe^{2+} to Fe^{3+} was determined for pre-treated and post-treated for all the samples by fitting the XANES spectra. This is a standard procedure [56-58]. The results are shown in Figures 70 to 73.

The linear combination comparison of AB1U and AB1T (Figure 70) which was treated with 0.1M DTPA showed that the untreated wood contained a higher percentage of Fe^{3+} than Fe^{2+} (roughly 80:20). This is expected of wood that has been exposed to air for a considerable amount of time. The treated sample also contained a higher amount of Fe^{3+} than Fe^{2+} however the ratio is 72.1:27.9 an increase of about 8% of Fe^{2+} content. The treatment solution was also analysed and showed a higher concentration of Fe^{2+} ions in solution. This could be explained as DTPA preferentially sequestering Fe^{2+} ions. It could also be due to reduction of iron upon the formation of DTPA-Fe complex. If the same piece of sample was analysed pre and post treatment, as in the 16.5 experiment, then a better understanding would have been gained. However due to beam time awards this was not possible.

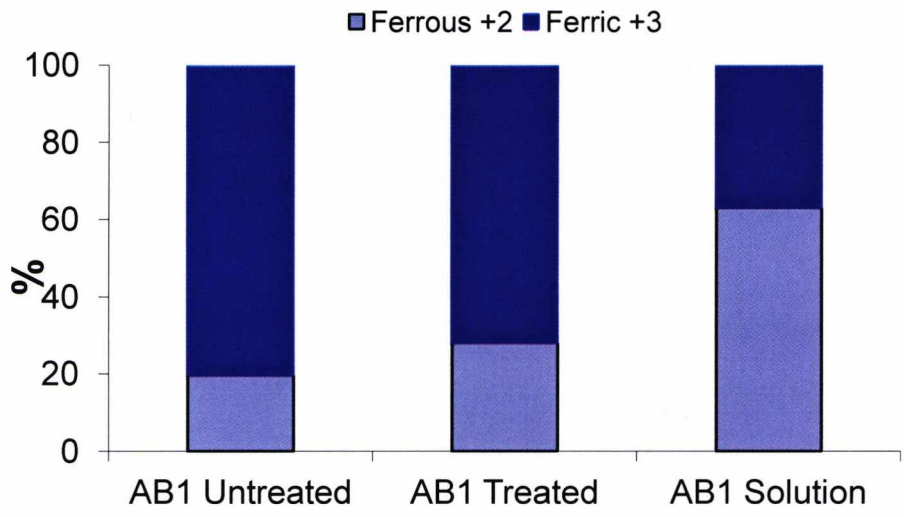

Figure 70: XANES linear combination comparison of MRT04 sample AB1U, AB1T and AB1 with 0.1 M DTPA solution.

For AB2U and AB2T (treated with 0.05M calcium phytate), the linear combination showed a Fe^{3+} / Fe^{2+} ratio of 91% : 9% for the untreated sample AB2U and 97.6% to 2.4% for the treated sample AB2T. The treatment solution contained only Fe^{3+} ions; this could point to a preferential sequestering of Fe^{3+} ions by calcium phytate but it could also depend on the availability of the Fe^{3+} or Fe^{2+} ions for complexing and also the number of moles of calcium phytate available in solution (Figure 71).

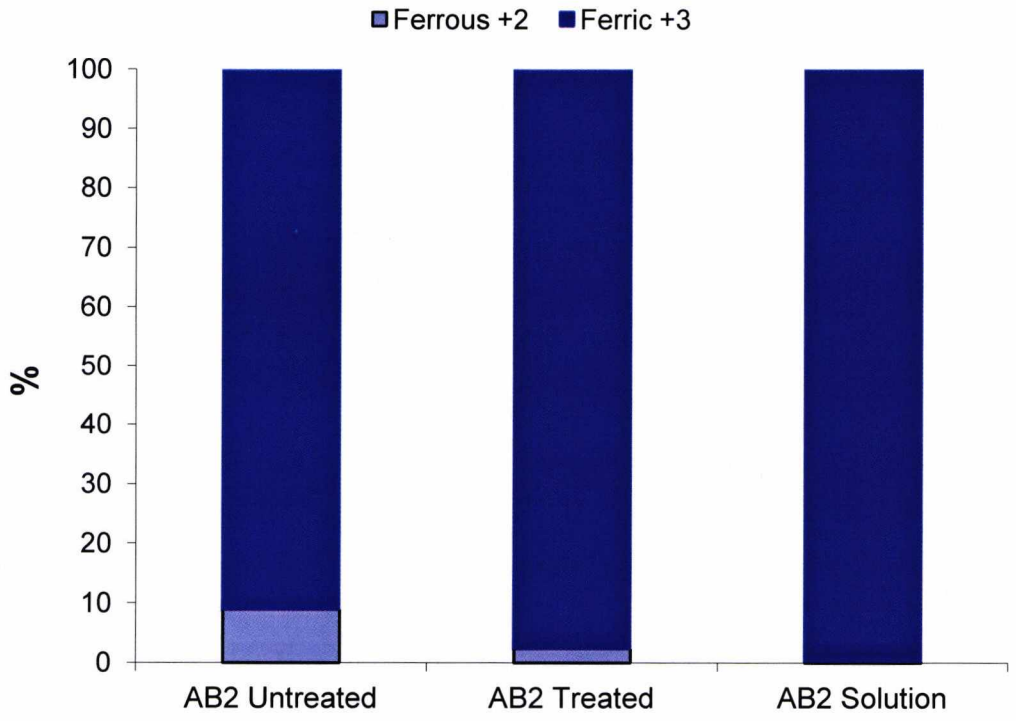

Figure 71: XANES Linear combination comparison of MRT04 samples AB2U, AB2T and AB2 with 0.05 M calcium phytate solution.

For the core sample from the upper deck of the *Mary Rose* which has been PEG treated (CS_UL); the linear combination comparison (Figure 72) for pre treatment gave a Fe^{3+} / Fe^{2+} ratio of 90.3% to 9.7%. Treated sample (treated with 0.1M DTPA) gave a ratio of 84.2% to 15.8%. Consistent with the previous analyses the treatment solution contained a higher proportion of Fe^{2+} ions compared to Fe^{3+} ions; this points to preferential chelation of Fe^{2+} ions by DTPA.

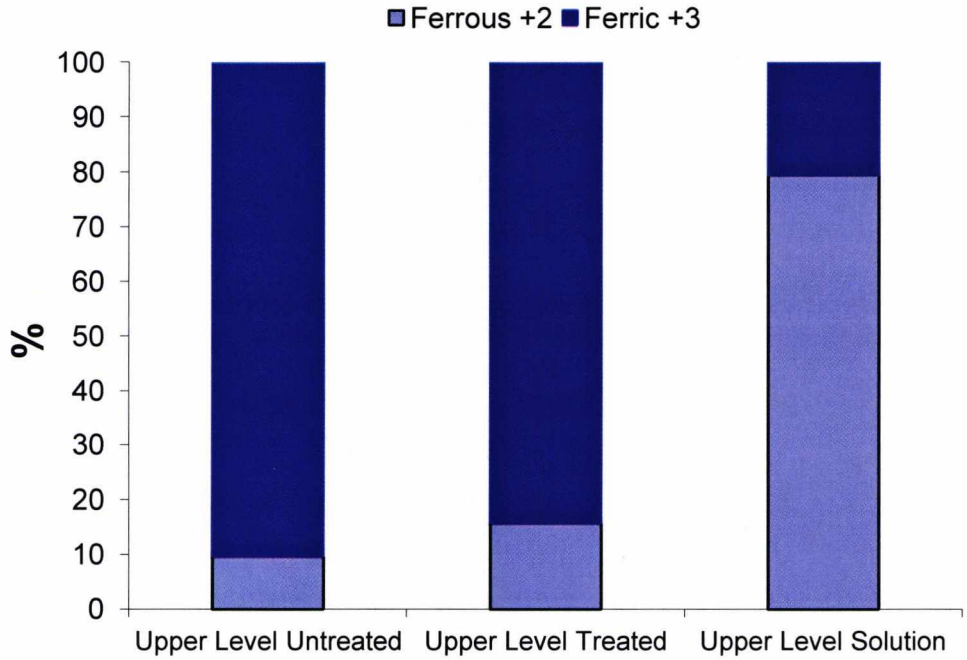

Figure 72: XANES Linear combination comparison of core samples CS_UL from the upper level of the *Mary Rose* treated with 0.1 M DTPA.

The results from the core sample from the lower level which has also undergone PEG treatment for several years (Figure 73) showed a Fe^{3+} / Fe^{2+} ratio of 84.8% to 15.2% for the untreated sample and 90% to 10% for the treated sample (treated with 0.05M Cal Phy). The treatment solutions gave a ratio of 65.9% to 34.1%. Comparing these results with those of AB2 shows that calcium phytate may preferentially bind Fe^{3+} but will also bind Fe^{2+} and the whole mechanism of complexing may depend on the availability of the Fe ion in the wood.

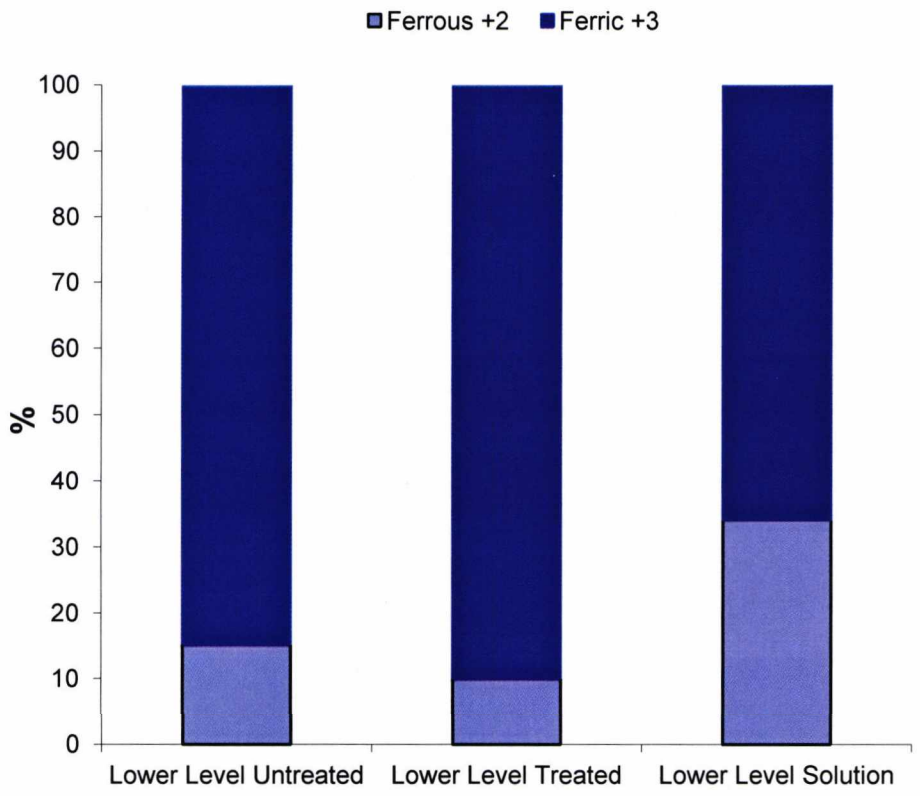

Figure 73: XANES Linear combination comparison of core samples CS_LL from the lower level of the *Mary Rose* treated with 0.05 M calcium phytate.

IV.5 SEM Results and discussion

The SEM results showed that the concentration of sulfur generally increased with increasing depth whereas the concentration of iron decreased with increasing depth in the *Mary Rose* timbers. Although the SEM analysis showed the presence of sulfur and iron, it did not provide any information about their speciation. It also showed the presence of several elements typically; sulfur, iron, sodium and chlorine (see Table 7 and the spectra below). There were also trace amounts of silicon, and magnesium in some samples. It however could not provide any information of their speciation. These trace elements will have come from a variety of sources. The sodium, magnesium and chlorine originate from the sea water. The silicon present will have originated in the sand in the silt which covered the ship.

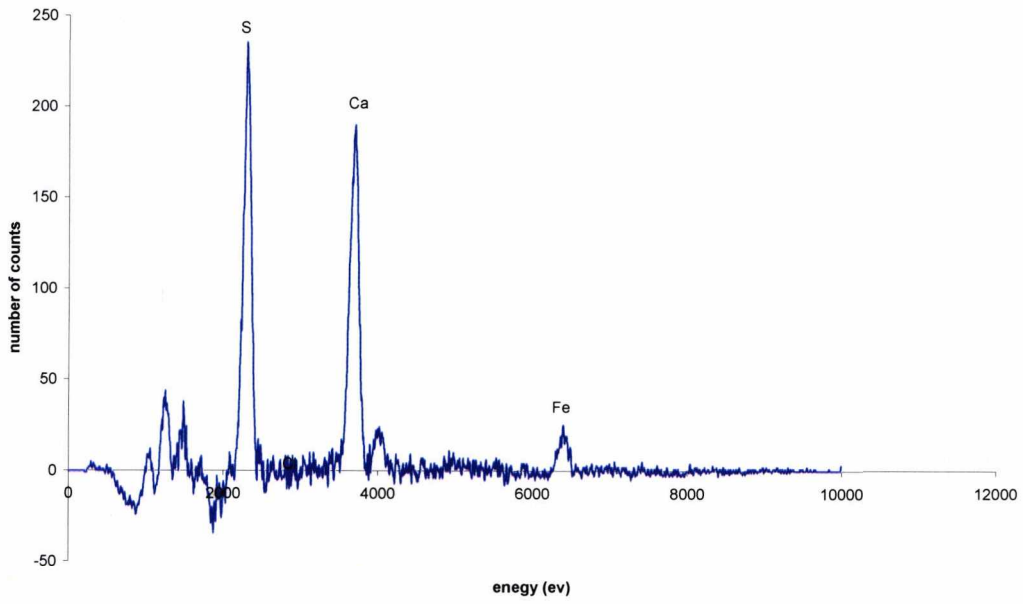

Figure 74: EDX plot of sample from the *Mary Rose* main deck.

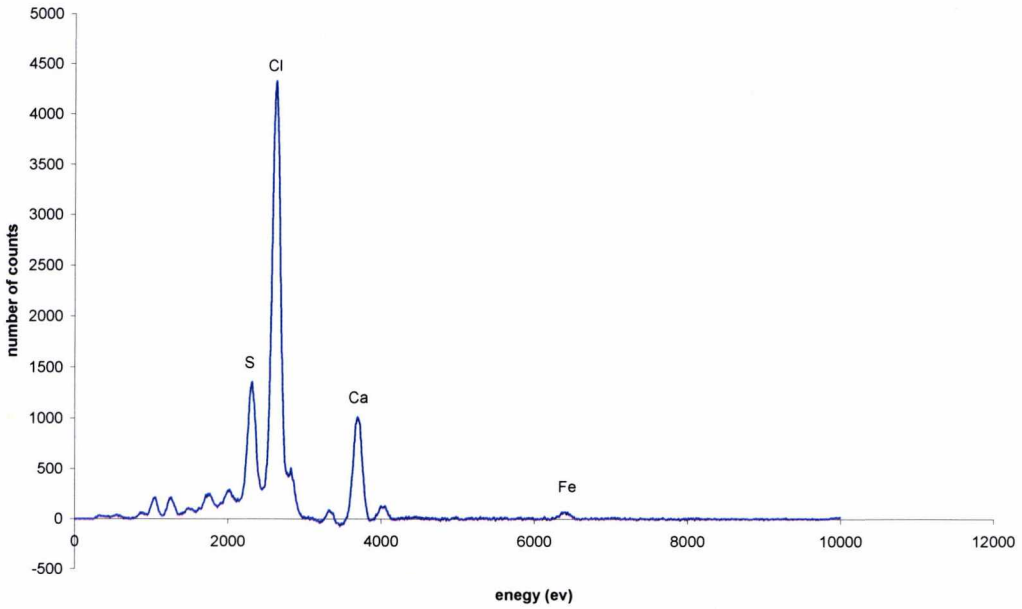

Figure 75: EDX plot of a recently recovered sample from the *Mary Rose.*

SEM analyses of *Mary Rose* Samples and samples from other wreck sites showed that amount of iron present generally decreased with increasing depth and the amount of sulphur generally increased with increasing depth (see Figure 76). This was however not typical for every *Mary Rose* sample. Some samples showed the reverse. This could be due to how the ship laid in the seabed (the *Mary Rose* rested on one side on the sea bed, as shown in Figure 5).

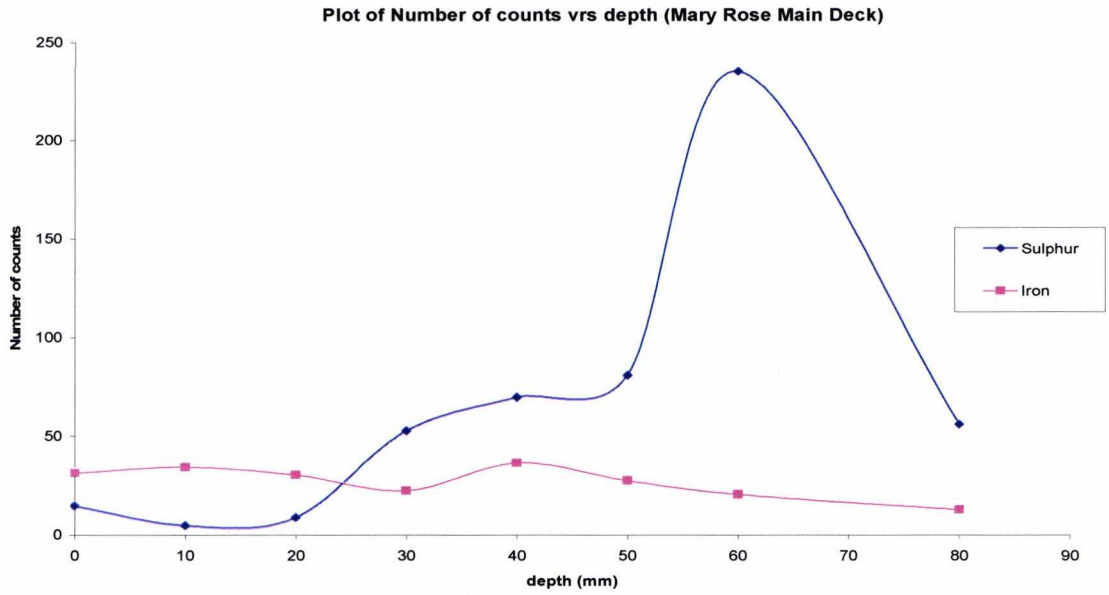

Figure 76: A graph comparing the number of counts of sulfur and iron to increasing depth

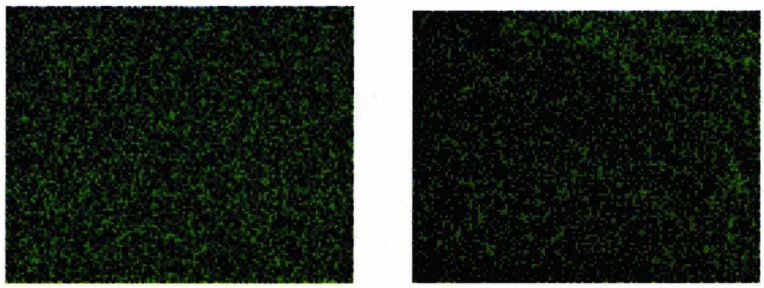

Sulfur Iron

Figure 77: X-ray maps showing sulfur and iron content of MR SPU

SEM images of the samples also showed a considerable amount of cell wall degradation, which affects the mechanical strength of these samples (see Figure 78).

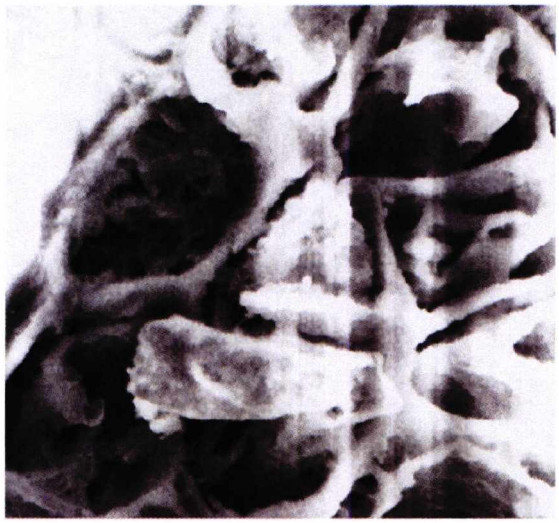

Fig. 78: SEM images of recently recovered *Mary Rose* Sample (MR 06).

SEM Analyses of samples also showed the presence of various elements mainly iron, sulfur and calcium (Table 7). Trace amounts of elements like silicon, potassium and phosphorus were also detected.

Table 7: Elements detected in samples from the *Mary Rose* and other wreck sites

Sample	Elements present				
	Iron (Fe)	**Sulfur (S)**	**Calcium (Ca)**	**Chlorine (Cl)**	**Sodium (Na)**
MR 06	Yes	Yes	Yes	Yes	-
SL 03	Yes	Yes	Yes	-	-
MR SFK	Yes	Yes	-	-	-
MR SPU	Yes	Yes	-	-	-
MR MD	Yes	Yes	Yes	Yes	Yes
NE Fe	Yes	Yes	-	-	-

IV.6 Ancillary experiments on cellulose

An investigation was carried out into role of ferrous and ferric sulfate in the breakdown of cellulose which is a main constituent of fresh wood.

It is well known that cellulose is broken down via acid hydrolysis and that strong acids like sulfuric acid have detrimental effects of cellulose. Also it has been proposed that certain metals like iron can also cause the breakdown of cellulose. As discussed in the Introduction this is assumed as the mode of decay of paper by iron gall ink [43-52]. Therefore, it was useful to examine with the techniques used in the work on the *Mary Rose* the degradation of cellulose.

Cellulose was pressed into pellets using polyvinyl acetate as a binding agent and then soaked in various concentrations of $FeSO_4$ for 48 hours. For comparison purposes cellulose pellets were also soaked in various concentrations of H_2SO_4 for the same length of time (48 hours) and then analysed using X-ray diffraction methods.

The results for the sulfuric acid treatments are shown in Figure 78. It was found that the cellulose peak around $2\theta = 24^0$ decreases with increasing H_2SO_4 concentration until 4M and then there seems to be a reconstitution of this peak. There is acid catalysed hydrolysis of the cellulose occurring here via the fission of the glycosidic oxygen link between two sugar units [111, 112].

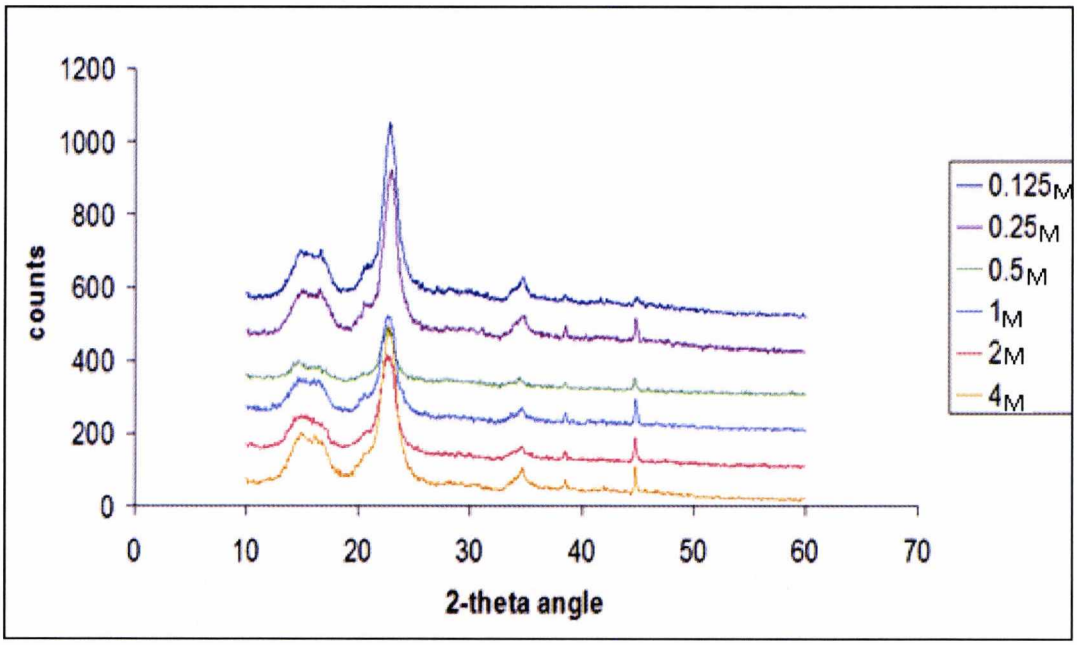

Figure 78: XRD plots of cellulose soaked in various concentrations of H_2SO_4.

For the iron sulfate experiment; there is only a slight reduction of the cellulose peak with increasing concentration of iron sulfate until concentration of 2M where the cellulose peak almost disappears, as seen in Figure 79.

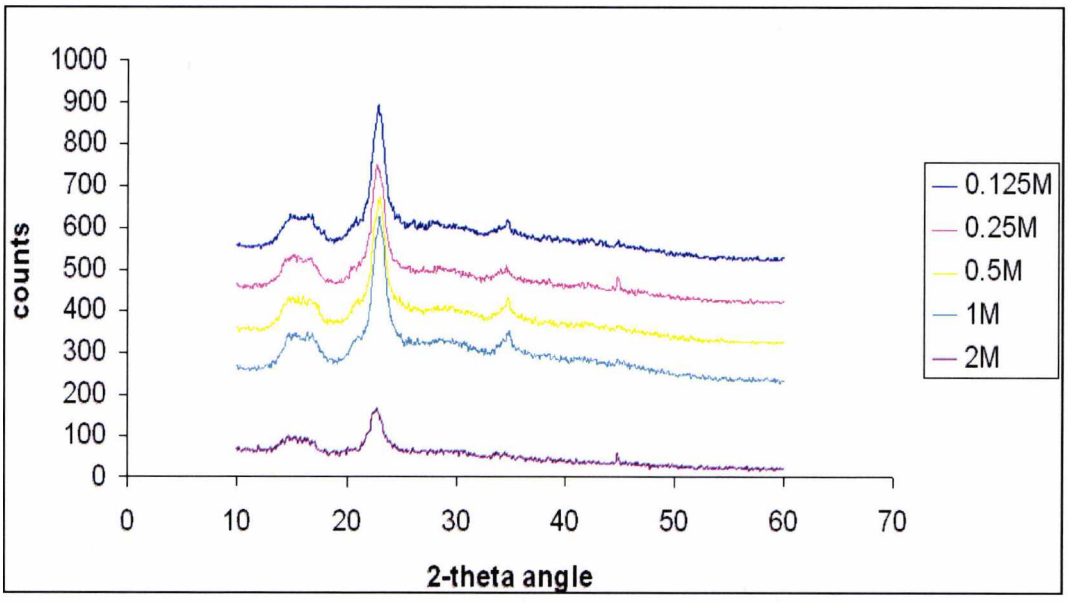

Figure 79: XRD plots of cellulose soaked in various concentrations of ferrous sulfate, $FeSO_4$.

Fe^{2+} catalysed breakdown of cellulose is via the Fenton reaction and the Fe^{2+} is in the process oxidised to Fe^{3+} [43-52]. This can easily be tracked by Fe K-edge XANES and experiments were carried out at the SRS at Daresbury SRS to investigate this process. Again cellulose pellets were soaked in concentrations of ferrous sulfate ranging from 0.125M to 0.5M. XANES runs were taken after one hour of soaking. Controlled experiments under nitrogen gas were also carried out to make sure that the oxidation of iron ions is not due to oxygenated air.

The results of the XANES experiments are shown in Figure 80. The edge positions of iron in the solutions after one hour treatment are slightly shifted higher energy and lie between the +2 and +3 edge positions. This shows a slight oxidation of the iron in the solutions starting from +2 moving to +3 oxidation state.

The XANES confirms that there is a reaction taking place; possibly a Fenton type iron catalysed degradation however the XANES tool does not allow for this to be ascertained with complete certainty. If these results are however used in conjunction with the XRD measurements then it can be concluded that there is oxidation of iron from Fe^{2+} to Fe^{3+} and the degradation of cellulose via a Fenton type mechanism is occurring.

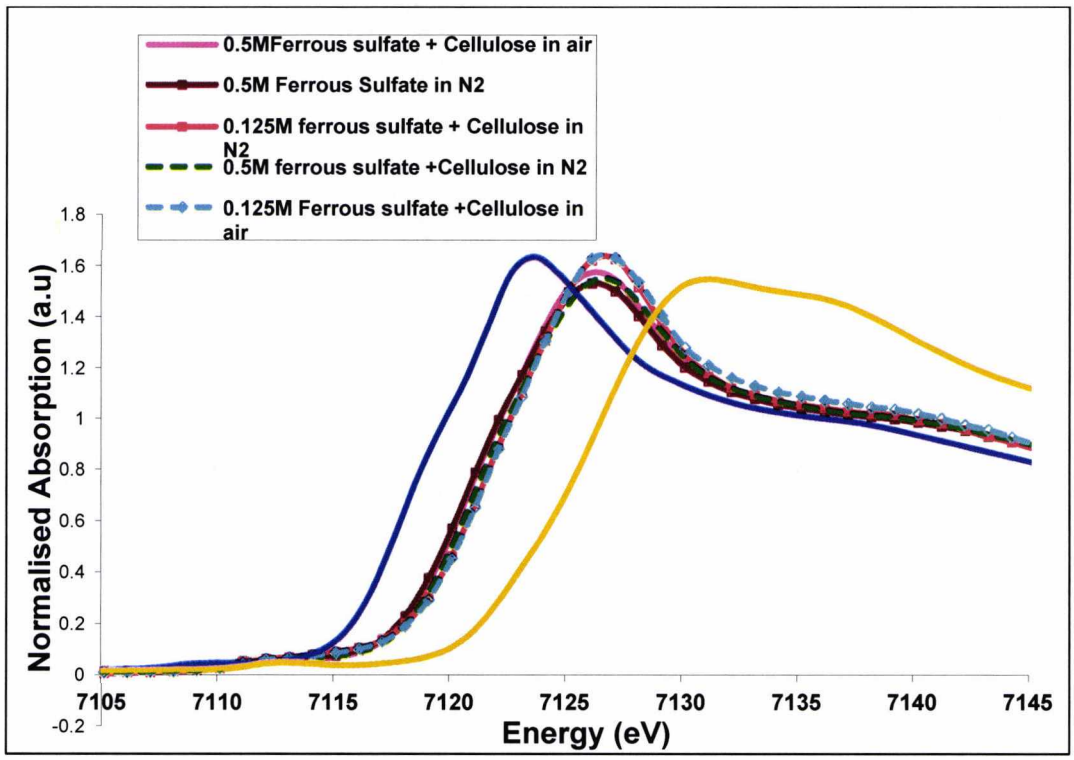

Figure 80: XANES of cellulose treated with ferrous sulfate under controlled conditions. The solid blue and yellow lines are the XANES of pure ferrous sulfate and ferric sulfate, respectively.

V. CONCLUSIONS

The work in this thesis has employed synchrotron techniques with a major emphasis on XAS measurements, both bulk and microfocus probes. Before looking at the conclusions of the work in specific detail it is worth making some general comments on the techniques. XAS measurements are almost unique in providing the speciation of atoms in a sample via the XANES. They are particularly useful for sulfur, which has a wide range of oxidation states. Another advantage of the technique is that there is no requirement for control of the sample environment; in contrast to electron microscopy which requires a high vacuum. This is important for archaeological samples which need to be conserved.

However, the current work has shown the need to use the bulk and microfocus XAS measurements in parallel, particularly for archaeological samples. It is clear that the iron and sulfur contents and speciation can vary widely from sample to sample of the *Mary Rose* timbers. Thus, whilst a microfocus experiment can give details at the wood cell level the results may not be extrapolated to the whole sample or the timbers in general. Bulk XAS measurements will give a more representative picture of the composition of the sample. However, even in this case there can be variations in composition over distances as small as a few millimetres [113]. In the current study of the effectiveness of chelating agents in removing iron from *Mary Rose* timbers, care was taken wherever possible, to ensure that the same samples and sample positions were used for the before and after treatment measurements.

V.1 The nature of iron and sulfur species in the *Mary Rose* timbers.

The nature of the iron and sulfur species is of extreme importance. In particular, it has been assumed that it is Fe^{2+} that gives rise to the production of sulfuric acid [13]. The current study has shown that in the timbers that had not been PEG treated contained iron in the surface regions that was predominantly Fe^{3+}. Others workers have also found predominantly Fe^{3+} in the surface of the timbers [8]. Most of the work in this thesis used samples close to the surface of the timbers. It was only in samples taken deep into

the timbers in the 16.5 experiments that there were significant concentrations of Fe^{2+}.

A range of sulfur species were found in the samples. The predominant species were reduced sulfur species, elemental sulfur and sulfate. Very little pyrite was found in the timbers studied, but it should be noted that these timbers had not been PEG treated. Some pyrite was found in the cell walls. The present studies were predominantly on the surface regions of the timbers and the conclusion is that the bulk of the pyrite which may have been present had oxidised in the moist, oxygen containing environment in which they had been stored after recovery from the sea bed.

A key finding of the present study is the co-location of iron and sulfate in the timbers. This had been postulated but had not been experimentally verified. The production of sulfuric acid has been proposed to involve the oxidation of iron sulfides *via* the reaction

$$2\ FeS_2 + 7O_2 + 2\ H_2O \rightarrow 2\ FeSO_4 + H_2SO_4$$

Therefore one of the products is iron sulfate. The fact that the experiments on I18 described in Section IV.3.1 showed iron and sulfate in the same positions on the XANES maps strongly supports an oxidation mechanism of iron sulfides by the above reaction.

The bulk and microfocus XAS experiments show that a large fraction of the iron in the current samples was in the form of an oxide. This is most likely to be goethite (FeO(OH)). The XANES analysis and the fitting of the EXAFS (Section IV.3.1) are consistent with this identification. Better microfocus EXAFS data are required to fully substantiate this conclusion, however the data collection times would be prohibitive.

V.2 The effect of chelating agents on the *Mary Rose* timbers.

All the four chelating agents used in this work (EDTA, DTPA, ammonium citrate and calcium phytate) were effective in removing iron from the timbers. However, the more efficient are DTPA and calcium phytate in terms of amount removed at fixed molarity. The current cost of the reagents would fight against the use of calcium phytate (£134 for 5g compared to DTPA at £120 for 50g).

The XANES studies of the chelating agents were described in Sections IV.3.1 and IV.4. The XANES experiments on the timbers show that after treatment with the DTPA there is more Fe^{2+} in the treatment solution compared to Fe^{3+}. This could mean that DTPA is removing the Fe^{2+} preferentially from the wood or the formation of the iron ligand complex in the wood is changing the coordination chemistry of the iron. The calcium phytate treatment solutions were richer in Fe^{3+} which could suggest the preferential removal of this species compared to Fe^{2+}.

The bulk XAS results (Section IV.2) show that the chelating agents DTPA, calcium phytate and ammonium citrate change the nature of the Fe K-edge XANES; the pre-edge features and post-edge shoulders are different after treatment. This could be the result of the chelating agents preferentially removing certain iron species (XAS is an average technique) or that they are breaking down more complex iron species. It would be difficult to resolve this difference using samples with a wide diversity in iron species such as exist in the *Mary Rose* timbers. The resolution of the problem would require displacement reactions with a series of model iron compounds and chelating agents.

V.3 The effect of PEG on the *Mary Rose* timbers.

The studies of the arrow tip (Section IV.3.3) were especially revealing. This sample was treated with PEG and dried immediately after it was removed from the sea bed; hence it had only a short exposure to the normal moist and oxygen rich atmosphere. The first observation was that the sample was relatively rich in iron sulfides compared to the other timbers that were studied. The evidence for this observation is from both the electron microscopy and the XAS studies. Therefore, it can be concluded that iron sulfides in the timbers are rapidly oxidised in the normal atmosphere.

These studies, along with the XRF studies of a core PEG treated sample from the *Mary Rose* (Section IV.3.3) also showed that the chelating agents are less effective at removing iron from PEG treated wood. This is presumably due to the PEG blocking the penetration of the solutions of the chelating agents into the wood. The result has significant consequences for the conservation procedures as it suggests that PEG would need to be

removed to aid effective iron remediation. For large objects this could prove problematic as the PEG treatment can take several years. Similarly PEG removal would take comparable time. Therefore the use of chelating agents is more suited to small objects and freshly raised timbers prior to their PEG treatment.

V.4 An overview of the sulfur problem.

This work has confirmed some of the aspects of the sulfur problem. The work on cellulose showed that iron sulfate as well as sulphuric acid will contribute to the degradation of cellulose in timbers. A number of iron chelating agents have been shown to be effective in removing iron species from timbers and could effectively reduce the formation of sulfuric acid. A large variety of sulfur species have been found in the timbers, which would be difficult to remove, and in some cases have unknown effects on the long term stability of the timbers. As mentioned above the identification of iron sulfate, by the co-location of iron and sulfate in the microfocus XRF maps, is excellent support for the proposed mechanism of production of sulfuric acid from iron sulfides.

The sulfur problem still remains, although the work in this thesis has provided possible routes to the iron remediation *via* chelating agents.

VI. SUGGESTIONS FOR FUTURE WORK

VI.1 Overview of the current status of conservation of the *Mary Rose* and *the Vasa*

Before considering specific areas of research that could alleviate the sulfur problem in the *Mary Rose* timbers it is worthwhile looking at what is being done in the general conservation of water-logged ships. The original recognition of the sulfur problem was at the *Vasa* in the wet summer of 2000, when the record number of visitors led to a relative humidity (RH) of 65% and an inadequate air conditioning system [9, 66, 114, 115]. As a result there has been much effort to improve the air conditioning system for water-logged archaeological wood. The *Vasa* museum curators have replaced and upgraded their air conditioning and this has alleviated the sulfur problem [114, 115]. The *Mary Rose* Trust have made use of the experience of the *Vasa* and the new museum for the *Mary Rose*, due to open in 2012 has been designed with very powerful air conditioning [116]. Thus there is now no real need to develop remediation methods for the whole of a ship's timbers. The aim now is to produce treatments for small regions, where there is a known high concentration of sulfur and/or iron, and for small artefacts.

VI.2 Iron chelating agents

There are many chelating agents that can be used to remove iron salts from the timbers; however a comparative study of the rates of removal and cost has not been published. Unfortunately there was insufficient time during this project to complete such a detailed study but it would be very worthwhile to be undertaken in future work. It is worth noting here that the *Vasa* researchers claim the EDMA is an extremely effective chelating agent for ships timbers [9, 66, 114, 115]. However, their sample of this compound was especially prepared for them by Akzo Chemicals, Sweden and is not generally available. An unsuccessful attempt to obtain a sample for the work in the current project was made. It would be useful to conduct independent studies of the chelating powers of this material.

Although there has been work on the use and selection of the iron chelating agents for archaeological wood there has been little work on the long term effects of the reagents on the wood structure. There is the possibility that the reagents could react with the wood. In addition, the control of the pH of some of the reagents is crucial. EDTA and DTPA can be quite acidic and could react with cellulose unless there is careful control of the pH. Thus research into the long term effects of the chelating agents would be useful and provide guidelines for the conservation.

VI. 3 Alkaline nanoparticle treatments

The Italian group led by Baglioni have used nanoparticles of magnesium and calcium hydroxide to treat a variety of conservation problems involving acid attack of artefacts [23, 117-122], including the *Vasa* timbers [23]. A long established technique for treating acid degraded artefacts was to use solutions or poultices of a mild alkali, such as sodium bicarbonate or carbonate. However, this leads to the formation of crystallites of reaction product, for example sodium sulfate, which can grow and destroy the structure of the artefact by simple mechanical pressure.

The main focus for de-acidification procedures has been the conservation of paper [123-125]. The most common ink used before the twentieth century was made from ferrous sulfate and gall nuts which degrades to produce sulfuric acid which hydrolyses the cellulose. In addition, the iron ions produce hydrogen peroxide by Fenton type reactions and there is further attack of the cellulose. The application of mild alkalis has been refined in the Bookkeeper procedure, a commercial technique that utilises sub-micron size particles of magnesium oxide in a fluorinated organic solvent with a fluorinated surfactant [126-128]. The concept is that the magnesium oxide in air will convert to the hydroxide which, in turn, will react with any acid in the paper. This is summarised by the following equations:-

$$MgO + H_2O \rightarrow Mg(OH)_2$$

$$\mathrm{Mg(OH)_2 + H_2SO_4 \rightarrow MgSO_4 + 2H_2O}$$

The Bookkeeper process is now widely employed in libraries and museums. Baglioni and co-workers [23, 116-122] took this concept a step further by

using nanoparticles of magnesium hydroxide (~ 100 nm) in a dispersion with an organic liquid, such as iso-propanol. The use of nanoparticles, smaller than the cell dimensions of biomaterials. will give a faster and deeper penetration than sub-micron particles. This has proved to be very successful; however there is much further work to be undertaken before this technique is used to conserve water-logged wooden objects.

The techniques used by Baglioni's group are fairly basic involving analysis of the pH of samples, thermogravimetric analysis, optical and electron microscopy and visual inspections. There are clear areas for further work in this area if nanoparticles are to be used on timbers. Firstly, there is a need for good diffusion measurements to provide reliable estimates of the penetration depths versus time for the nanoparticles. Secondly, there should be more work on the production of the nanoparticles. The nanoparticles used by Baglioni at 100 nm are not particularly small. High energy ball-milling will produce particles in the 10-20 nm range [129, 130] and it would be interesting to study the use of these smaller nanoparticles as basic oxides or carbonates. Similarly, the chemistry and physics of the process require a deeper study using the techniques used in this thesis. For example, a microfocus XAS study of nanoparticle treated *Mary Rose* timbers would show where the products of the nanoparticles reside in the timbers.

VI. 4 Antioxidant treatments

In the search for treatments to conserve archaeological wooden objects researchers have examined the old literature for techniques used by craftsmen working with wood. A material that has been used for hundreds of years in violin polish is propolis (it was reputedly used by Stradivarius). Currently this is being tested as a preservative for wooden artefacts at the *Mary Rose* Trust [116]. Propolis is a natural resin produced by bees as a sealant and building material in the hive. It appears to be a good antioxidant and has antibacterial properties; it is used by bees at the entrance to the hive prevent diseases and parasites from entering the hive, and to inhibit bacterial growth [131]. There have been remarkable claims made for propolis as an antibiotic and antifungal agent [132], as a treatment for tumors [133], as a treatment for burns [134] and as a dietary additive to improve health. It is

now widely sold in health food shops [135]. The chemical composition of propolis is very complex (containing many compounds) and varies from hive to hive [136-138]. However, samples of propolis contain a range of flavanoids, which are compounds based on a backbone of 2-phenylchromen-4-one (2-phenyl-1,4-benzopyrone), which is shown below. These compounds are widely found in biological systems, plants and animals, and have beneficial properties due to their antioxidant behaviour.

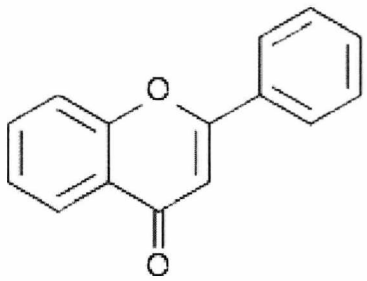

Molecular structure of the flavone backbone (2-phenyl-1,4-benzopyrone)

The preliminary studies at the *Mary Rose* Trust have shown that treatment with propolis of artefacts that exhibit discoloration due to the sulfur problem are greatly improved in terms of stability and appearance [116]. The chemical processes that are involved in this improvement are worthy of further study. Again, some of the techniques used in the current project would be helpful. For example, XAS studies of the iron and sulfur speciation before and after propolis treatment would be an interesting investigation.

VI.5 Sulfur remediation

The bulk of the sulfur in the *Mary Rose* timbers is in the form of elemental sulfur and organosulfur compounds [8]. Removal of these compounds is not practical as it would require solvents and reagents that would damage the wood. Therefore work on the long term stability of these compounds in the museum environment would be useful.

REFERENCES

1. Vine, S. *Mary Rose* Deck Construction, *Mary Rose Trust,* Portsmouth, UK (1998); *information on the Mary Rose* is also available on the website; http://www.maryrose.org/
2. Jones, M. For Future Generations: Conservation of a Tudor Maritime Collection, *The Mary Rose Trust*, Portsmouth, UK (2003).
3. www.nmm.ac.uk/explore/sea-and-ships/facts/navies-and-warships/henry-viii-and-his-navy.
4. Fenge, D., Wegner, G., Wood Chemistry, Ultrastructure, Reactions, *Walter de Gruyter,* Berlin, (1989), p, 613.
5. Blanchette, R.A., (2000) A review of microbial deterioration found in archaeological wood from different environments. *International Biodeterioration and Biodegradation,* 46, 189-204.
6. Christensen, B.B., The conservation of waterlogged wood, *The National Museum of Denmark*, Copenhagen, (1970) p. 99.
7. Kaye, B., (1995) Conservation of Waterlogged Archaeological Wood. *Chemical Society Reviews*, 24, 35-43.
8. Wetherall, K.M., Moss, R.M., Jones, A.M., Smith, A.D., Skinner, T., Pickup, D.M., Goatham, S.W., Chadwick, A.V. and Newport, R.J. (2008) Sulfur and iron speciation in recently recovered timbers of the *Mary Rose* revealed via X-ray absorption spectroscopy. *J. Archaeological Science*, 35, 1317-1328.
9. Fors, Y. and Sandstrom, M., (2006) Sulfur and iron in shipwrecks cause conservation concerns. *Chem Soc Rev.*, 35, 399-415.
10. Pallud, C. and Van Cappellen, P., (2006) Kinetics of microbial sulfate reduction in estuarine sediments. *Geochimica et Cosmochimica Acta*, 70, 1148-1162.
11. Lowson, R.T., (1982) Aqueous pyrite oxidation by molecular oxygen. *Chem. Rev.,* 82, 461.
12. Moses, C.O., Nordstrom, D. K., Herman, J. S. and Mills, A.L., (1987) Aqueous pyrite oxidation by dissolved oxygen and by ferric iron. *Geochim. Cosmochim. Acta*, 51, 1561-71.
13. Sandstrom, M. Damian, F.J., Fors, Y., Gelius, U., Jones, M., and Salome´, M., (2005) Sulfur accumulation in the timbers of King Henry

VIII's warship *Mary Rose*: A pathway in the sulfur cycle of conservation concern. *Proc. Nat. Acad. Sci. U. S. A.*, 102, 14165-14170.

14. Baker, A.J., (1974) Degradation of wood by products of metal corrosion. *Forest service research paper FPL 229*.
15. Pinion, L.C., (1970) The degradation of wood by metal fastenings and fittings. *Timberlab Paper*, 27.
16. Marian, J.E., and Wissing, A., (1960) The chemical and mechanical detorioration of wood in contact with iron. *Svensk Papperstidn*, 63, 47-57.
17. Jack, R.F., Ringelberg, D.B. and White, D.C., (1992) Differential corrosion rates of carbon steel by bacteria, *Corrosion Science,* 33 1843-1853.
18. Gonzalez, J.E.G., Santana, F.J.H. and Mirza-Rosca, J.C., (1998) Effect of bacterial biofilm on 205 SS corrosion in natural seawater by EIS, Corrosion Science, 40, 2141-2154.
19. Von Wolzogen Kuhr, C.A.H. and Van Der Vlugt, L.S., (1934) Graphitization of cast iron as an electrobiochemical process in anaerobic soils. *Water*, 18, 147-155.
20. Sheng, X., Ting, Y. and Pehkonen, S.O., (2007) The influence of sulphate-reducing bacteria biofilm on the corrosion of stainless steel AISI 316. *Corrosion Science*, 49, 2159-2176.
21. Little, B., Wagner, P. and Mansfeld, F., (1992) An overview of microbial corrosion. *Electrochim. Acta,* 37, 2185-2194.
22. Sanders, P.F. and Hamilton, W.A., Biologically induced corrosion, *NACE International*, Houston, USA, (1986) p. 47.
23. Chelazzi, D., Giorgi, R. and Baglioni, P., (2006) Nanotechnology for Vasa Wood De-aidification. *Macromolecular Symposia*, 238, 30-36.
24. Xiang,Q., Lee, Y.Y., Torget, R.W., Pettersson, P. O., Eklund, R., and Zacci, G., (2003) Heterogeneous Aspects of Acid Hydrolysis of α-Cellulose Microcrystallites. *Applied Biochemistry and Biotechnology*, 107, 505-514.
25. Howie, A., Roentgen's Legacy, *Notes and Records of the Royal Society of London*, Vol. 52, No. 2 (Jul., 1998), 376-377
26. Podgoršak, E.B., Production of X-rays, Radiation Physics for Medical Physicists, *Springer*, Berlin Heidelberg, (2010), 177-205

27. Newville, M., X-ray Absorption Fine Structure, *Consortium for Advanced Radiation Sources*, University of Chicago, (2003).
28. Dent, A., An Introduction to X-ray Spectroscopy. *Diamond Light Source*, Oxon, UK, (2007).
29. Binsted N., Campbell J.W., Gurman S.J. and Stephenson P.C., *SERC Daresbury Program Library*, Daresbury Laboratory, Warrington, Cheshire WA4 4AD, UK, (1992).
30. Gianoncelli, A., Castaing, J., Ortega, L., Dooryhee, E., Salomon, J., Walter, P., Hodeau, J-L., and Bordet, P., (2008) A portable instrument for in situ determination of the chemical and phase compositions of cultural heritage objects. *X-Ray Spectrom.*, 37, 418-423.
31. Longoni, A., Fiorini, C., Leutenegger, P., Sciuti, S., Fronterotta, G., Strüder, L., and Lechner, P., (1998) A portable XRF spectrometer for non-destructive analyses in Archaeometry. *Nuclear Instruments and Methods in Physics Research A.*, 409, 407-409.
32. Bjeoumikhov, A., Langhoff, N., Rabe, J., and Wedell, R., (2004) A modular system for XRF and XRD applications consisting of a microfocus X-ray source and different capillary optics. *X-Ray Spectrom.*, 33, 312-316.
33. Benedetti, D., Alessandri, I., Bergese, P., Bontempi, E., Colombi, P., Garipoli, D., Pedrazzani, R., Zanola, P., and Depero, L.E., (2006) Laboratory microbeam analysis applied to cultural heritage studies. *Microchim Acta,* 155, 101-104.
34. Janssens, K., Vittiglio, G., Deraedt, I., Aerts, A., Vekemans, B., Vincze, L., Wei, F., Deryck, I., Schalm, O., Adams. F., Rindby, A., Knochel, A., Simionovici, A. and Snigirev, A., (2000) Use of microscopic XRF for non-destructive analysis in art and archaeometry. *X-Ray Spectrom.*, 29, 73-91.
35. Janssens, K., Proost, K. and Falkenberg, G., (2004) Confocal microscopic X-ray fluorescence at the HASYLAB microfocus beamline: characteristics and possibilities. *Spectrochimica Acta Part B.*, 59, 1637-1645.
36. Falkenberg, G., Clauss, O., Swiderski, A. and Tschentscher, T., (2001) Upgrade of the X-ray fluorescence beamline at HASYLAB/DESY. *X-Ray Spectrom.*, 30, 170-173.

37. Riekel, C., (2004) Recent developments in microdiffraction on protein crystals. *J. Synchrotron Rad.*, 11, 4-6.
38. Vincze, L., and Riekel, C., (2003) Status and perspectives of capillary optics at a third-generation synchrotron radiation source. *X-Ray Spectrom.,* 32, 208-214.
39. Erko, A., Schäfers, F., Firsov, A., Peatman, W.B., Eberhardt, W., and Signorato, R., (2004) The BESSY X-ray microfocus beamline project. *Spectrochimica Acta B.*, 59, 1543-1548.
40. Chadwick, A.V., Berko, A., Schofield, E.J., Jones, A.M., Mosselmans, J.F.W. and Smith, A.D., The Application of Microfocus X-ray Beams from Synchrotrons in Heritage Conservation. *Int. J. Architectural Heritage,* (in press).
41. Cotte, M., Susini, J., Dik, J. and Janssens, K., (2010) Synchrotron-Based X-ray Absorption Spectroscopy for Art Conservation: Looking Back and Looking Forward. *Acc. Chem. Res.,* 43, 705-714
42. Kolar, J., Strlic, M., Novak, G. and Pilhar, B.J., (1998) Aging and stabilization of alkaline paper. *Pulp Pap. Sci.,* 24, 89-94
43. Strlic, M., Kolar,J., Ageing and stabilisation of paper,. *National and University Library*: Ljubljana, Slovenia (2005).
44. Strlic, M., Kolar, J., Selih V.S., Kocar, D. and Pilhar, B., (2003) A comparative study of several transition metals in Fenton-like reaction systems at circum-neutral pH. *Acta Chim, Slov.*, 33, 234-244.
45. Kolar, J., Stolfa, A., Pompe, M., Pilhar, B., Bundar, M., Simcic, J. and, Ressiland, B., (2006) XANES analysis of Fe valence in iron gall inks. *Anal. Chim. Acta,* 555, 167-175.
46. Hahn, O., Malzer, W., Kanngiesser, B. and Beckhoff B., (2004) Characterization of iron-gall inks in historical manuscripts and music compositions using X-ray fluorescence spectrometry. *X-ray Spectrom.*, 33, 234-239
47. Hochleitner, B., Desnica, V., Mantler, M. and, Schreiner M., (2003) Historical pigments: a collection analyzed with X-ray diffraction analysis and X-ray fluorescence analysis in order to create a database. *Spectromchim. Acta, Part B: Spectrosc,.* 58, 641-655.
48. Reiche, I., Radtke, M., Berger, A., Gorner, W., Ketelsen, T., Merchel, S., Riederer, J., Riesemeier, H. and, Roth, M., (2004) Spatially resolved

synchrotron-induced X-ray fluorescence analyses of metal point drawings and their mysterious inscriptions. *Spectrochim. Acta, Part B: at Spectrosc.*, 59, 1657-1662.

49. Mommsen, H., Beier, T., Dittman, H., Heimerman, D., Hein, A., Rosenberg, A., Boghardt, M., Hanebutt-Benz, E-M. and Halbey, H., (1996) X-ray fluorescence analysis on inks and papers of incunabula with synchrotron radiation. *Archaeometry*, 38, 347-353.
50. Zappala, A., Bajt, S., Gigante, G.E. and Hanson, A.L., (1996) Applications of EDXRF in the conservation of acid papers using a synchrotron light microbeam. *Nucl. Instrum. Methods Phy. Res. B.*, 117, 145-150.
51. Budnar, M., Simcic, J., Ursic, M., Pelicon, P., Kolar, J., Selih, V.S. and Strlic M., (2006) Analysis of iron gall inks by PIXE, *Nucl. Instrum. Methods Phys. Res. B.,* 243, 407-417.
52. Darbour, M., Bonnassies, S. and Flieder, F., (1981) Les encres métallogalliques: étude de la dégradation de l'acide gallique et analyse du complexe férrogallique. *in Preprints of the 6th Triennial Meeting, Vol. II,* 6th International Congress on Restoration of Architectual Heritage *ICOM Committee for Conservation*, Los Angeles, p. 1.
53. Neevel, J.G., (1995) Phytate: a potential conservation agent for the treatment of ink corrosion caused by iron gall inks. *Restaurator,* 16, 143-160.
54. Wagner, B., Bulska, E., Stahl, B., Heck, M. and Ortner, H.M., (2004) Analysis of Fe valence states in iron-gall inks from XVIth century manuscripts by 57Fe Mössbauer spectroscopy. *Anal. Chim. Acta*, 527, 195-203.
55. Rouchon-Quillet, V., Remazeilles, C., Wattiaux, A. and Fournes, L., (2003) The impact of gallic acid on iron gall ink corrosion. *in Proceedings Chemical Technology of Wood, Pulp and Paper*, Bratislava, Slovakia, p. 393.
56. Lytle, F.W., Greegor, R.B. and Panson, A.J., (1988) Discussion of X-ray-absorption near-edge structure - application to Cu in the high-Tc superconductors. *Phys. Rev., B,* 37, 1550 1552.
57. Pantelouris, A., Modrow, H., Pantelouris, M., Hormes, J. and Reinen D., (2004) The influence of coordination geometry and valency on the K-

edge absorption near edge spectra of selected chromium compounds. *Chem. Phys.,* 300, 13-22.

58. Rueff, J.P., Journel, L., Petit, P.E. and Farges, F., (2004) FeK pre-edges as revealed by resonant X-ray emission. *Phys. Rev., B,* 69, Article 235107.
59. Proost, K., Janssens, K., Wagner, B., Bulska, E. and Schreiner M., (2004) Determination of localized Fe2+ /Fe3+ ratios in inks of historic documents by means of mu-XANES. *Nucl. Instrum. Methods Phys. Res. B.,*213, 723-728.
60. Kanngießer, B., Hahn, O., Wilke, M., Nekat, B., Malzer, W. and Erko A., (2004) Investigation of oxidation and migration processes of inorganic compounds in ink-corroded manuscripts. *Spectrochim. Acta, Part B: At. Spectrosc.,*59, 1511-1516.
61. Jansens, K., Rouchon-Quillet, V., Remazeilles ,C., Eveno, M. and Wattiaux A., *in Proceedings of the International Conference Durability of Paper and Writing*, Ljubljana, Slovenia, 2004, p. 54.
62. Arcon, I., Kolar, J., Kodre, A., Hanzel, D. and Strlic, M., (2007) XANES analysis of Fe valence in iron gall inks. *X-Ray Spectrom.,* 36, 199-205.
63. Smith, A.D., Pradell, T., Molera, J., Vendrell, M., Marcus, M. and Pantos, E., (2003) MicroEXAFS study into the oxidation states of copper coloured Hispano-Moresque lustre decorations. *J. Phys. IV,* 104, 519-522.
64. Doremus, R.H., Glass Science, *John Wiley & Sons,* New York, (1973), p. 327.
65. Nakai, I., Matsunaga, M., Adachi, M. and Hidaka, K.I., (1997) Application of XAFS in archaeology. *J. Phys. IV France,* 7, 1033-1034.
66. Sandstrom, M, Jalilehvand, F, Persson, I, Gelius, U, Frank, P, and Hall-Roth, I., (2002) Deterioration of the seventeenth-century warship Vasa by internal formation of sulphuric acid. *Nature*, 415, 893-897.
67. Lytle, F.W., Greegor, R.B., Sandstrom, D.R., Marques, E.C., Wong J., Spiro, C.L., Huffman, G.P. and Hugins F.E., (1984) Measurement of soft-X-ray absorption spectra with a fluorescent ion-chamber detector. *Nucl. Instr. Meth.*,226, 542 548.
68. Argast, A. Diffraction and Bragg's law. www.geosci.ipfw.edu/XRD.

69. Young, M.L, Casadio, F., Schnepp, S., Almer, J., Haeffner, D.R. and Dunand, D.C., (2006) Synchrotron X-ray diffraction and imaging of ancient Chinese bronzes. *Appl. Phys. A.,* 83, 163-168.
70. Gettens, R.J., (1951) The corrosion products of an ancient Chinese bronze. *J. Chem. Educ.*, 28, 67-80.
71. Gettens, R.J., The Freer Chinese Bronzes. *in Freer Gallery of Art: Oriental Studies,* No. 7. Smithsonian Institution, Washington, (1969), p. 127.
72. Kampf, G., Characterisation of Plastics by Physical Methods, Hanser Publishers, New York, (1986).
73. De Ryck, A., Adriaens. A., Pantos, E. and Adams F., (2003) A comparison of microbeam techniques for the analysis of corroded ancient bronze objects. *Analyst,* 128, 1104-1109.
74. Newbury, B., Stephenson, B., Almer, J.D., Notis, M., Cargill, G.S., Stephenson, G.B. and Haeffner D.R., (2004) Synchrotron applications in archaeometallurgy. Analysis of high zinc brass astrolabes. *Powder Diffr.* 19, 12-15
75. Stephenson, G.B., Stephenson, B. and Haeffner D.R, (2001) Investigations of astrolabe metallurgy using synchrotron radiation. *MRS Bull.*,26, 19-23.
76. Jenkins, R., X-Ray Fluorescence Spectrometry, *2nd Edition*, John Wiley and Sons, New York, (1999).
77. Lahanier, Ch., Amsel, G., Heitz, Ch., Menu, M. and Andersen H.H., (1985) Proceedings of the International Workshop on ion-beam analysis in the arts and archaeology - Pont-a-Mousson, Abbaye des Premontres, France, February 18-20, 1985 – editorial, *Nucl. Instrum. Methods Phys. Res. B.,* 14, (1986) R7-R8.
78. Riise, B.L. and Biddle, M.B., (2000) X-Ray Fluorescence Spectroscopy in Plastics. *American Plastics Council*, Arlington, VA, USA
79. Janssens, K., Vittiglio, G., Deraedt, I., Aerts, A., Vekemans, B., Vincze, L., Wei, F., Deryck, I., Schalm, O., Adams, F., Rindby, A., Knochel, A., Simionovici, A. and Snigirev, A., (2000) Use of Microscopic XRF for Non-destructive Analysis in Art and Archaeometry. *X-ray Spectrometry*, 29, 73-91.

80. P. Kirkpatrick, P. and Baez, A.V., (1948) Formation of Optical Images by X-rays. *J. Opt. Soc. Am.* 38, 766-773.
81. Ziegler, E., Bigault, T. and Hoszowska, J., (2004) An X-ray focusing system combining a sagittally-bent crystal and a Kirkpatrick-Baez system. *AIP Conf. Proc.,* 705, 768-771.
82. Barrea, R.A., Huang, R., Cornaby, S., Bilderback, D.H., and Irving, T.C. (2009) High-flux hard X-ray microbeam using a single-bounce capillary with doubly focused undulator beam. *J. Synchrotron Rad.*, 16, 76-82.
83. Chu, Y.S., Yi, J.M., De Carlo, F., Shen, Q., Lee, W.K., Wu, H.J., Wang, C.L., Wang, J.Y., Liu, C.J., Wang, C.H., Wu, S.R., Chien, C.C., Hwu, Y., Tkachuk, A., Yun, W., Feser, M., Liang, K.S., Yang, C.S., Je, J.H., and Margaritondo, G., (2008) Hard X-ray microscopy with Fresnel zone plates reaches 40 nm Rayleigh resolution. *Applied Physics Letters*. 92 article number 103119.
84. Kang, H.C., Maser, J., Stephenson, G.B., Liu, C., Conley, R., Macrander, A.L., and Vogt, S., (2006) Focusing of hard X-rays to 16 nanometers with a multilayer Laue lens. *Physical Review Letters*, 96 article number 127401.
85. Snigirev, A. and Snigireva, I., (2008) High energy X-ray micro-optics. *Comptes Rendus, Physique*. 9, 507-516.
86. Snigirev, A., Bjeoumikhov, A., Erko, A., Snigireva, I., Grigoriev, M., Yunkin, V., Erko M. and Bjeoumikhova S., (2007) Two-step hard X-ray focusing combining Fresnel zone plate and single-bounce ellipsoidal capillary. *J. Synchrotron Rad.*, 14, 326-330.
87. Farges, F., Etcheverry, M-P., Scheidegger, A. and Grolimund, D., (2006) Speciation and weathering of copper in "copper red ruby" medieval flashed glasses from the Tours cathedral (XIII century. *Applied Geochemistry*, 21, 1715-1731.
88. Ferreira da Silva, M.G. and Fernandez Navarro, J.M., (1987) Colour of silicate sol–gel glasses containing CuO. *J. Non-Crystalline Solids*, 100, 447-452.
89. Nagao, H., Misonou, M. and Kawahara, H., (1990) Mechanism of colouration in copper-stained float glass. J. *Non-Crystalline Solids*, 120, 199-206.

90. Burns, R.G. (1993) *Mineralogical Applications of Crystal Field Theory.* Cambridge University Press, Cambridge, UK.
91. Ching, W.Y., Xu, Y-N. and Wong, K.W., (1989) Ground-state optical properties of Cu2O and CuO crystals. *Phys. Rev. B.* 40, 7684-7685.
92. Spitzer-Aronson, M., (1975) Etude de vitraux rouge médiévaux à l'aide de microscope optique, microscope à balayage avec image par electrons rétrodiffusés et microsonde électronique à rayons X. *Verres et Réfractaires*, 29, 145-153.
93. Araujo, R.J., Butty, J. and Peyghambarian, N., (1996) Optical properties of glasses containing copper oxide particles. *Appl. Phys. Lett.*, 68, 584-586.
94. Arletti, R., Dalconi, M.C., Quartieri, S., Triscari, M. and Vezzalini, G., (2006) Roman coloured and opaque glass: a chemical and spectroscopic study. *Appl. Phys. A.* 83, 239-245.
95. Colomban, P. and Schreiber, H.D., (2005) Raman signature modification induced by copper nanoparticles in silicate glass. *J. Raman Spectros.*, 36, 884-890.
96. Padovani, S., Borgia, I., Brunetti, B., Sgamellotti, A., Giulivi, A., d'Acapito, F., Mazzoldi, P., Sada, C., and Battaglin, G., (2004) Silver and copper nanoclusters in the lustre decoration of Italian Renaissance pottery: an EXAFS study. *Appl. Phys. A.* 79, 229-233.
97. Song, Y., Doomes, E.E., Prindle, J., Tittsworth, R., Hormes, J. and Kumar, C.S.S.R., (2005) Investigations into sulfobetaine stabilized Cu nanoparticle formation: toward development of a microfluidic synthesis. J. *Phys. Chem. B.,* 109, 9330-9338.
98. Rothe, J., Hormes, J., Bönemann, H., Brijoux, W. and Siepen, K., (1998) In situ X-ray absorption spectroscopy investigation during the formation of colloidal copper. *J. Am. Chem. Soc.*, 120, 6019-6023.
99. Cheah, S.F., Brown, G.E. and Parks, G.A., (2000) XAFS study of Cu model compounds and Cu sorption products on amorphous SiO_2, gamma–Al_2O_3, and anatase. *Am. Mineral.*, 85, 118-132.
100. Faa, G. and Crisponi, G., (1999) Iron chelating agents in clinical practice, *Coordination Chemistry Reviews*, 184, 291-310.

101. Knepper, T.P., (2003) Synthetic chelating agents and compounds exhibiting complexing properties in the aquatic environment. *Trends in Analytical Chemistry*, 22, 709-724.

102. Witter A.E., Hutchins, D.A., Butler, A. and Luther, G.W., (2000) Determination of conditional stability constants and kinetic constants for strong model Fe-binding ligands in seawater, *Marine Chemistry,* 69, 1–17.

103. Raboy, V., (2001) Seeds for a better future: 'low phytate' grains help to overcome malnutrition and reduce pollution, *TRENDS in Plant Science*, 6, 1-36.

104. Glusker, J.P., (1980) Citrate conformation and chelation. *Accounts of Chemical Research,* 13, 345-352.

105. www.unl.edu/CMRAcfem/em.htm. Electron microscopy.

106. Bogner, A., Jouneau, P.H., Thollet, G., Basset, D. and Gauthier, C., (2007) . A history of scanning electron microscopy developments: Towards "wet-STEM" imaging. *Micron*, 38, 390-401.

107. Bilsborrow, R.L., Atkinson, P.A., Bliss, N., Dent, A.J., Dobson, B.R. and Stephenson, P.C., (2006) A wide-aperture dynamically focusing sagittal monochromator for X-ray spectroscopy and diffraction. *Journal of Synchrotron Radiation*, 13, 54–58.

108. Mosselmans, J.F.W., Quinn, P.D., Dent, A.J., Cavill, S.A., Moreno, S.D., Peach, A., Leicester, P.J., Keylock, S.J., Gregory, S.R., Atkinson, K.D. and Rosell, J.R., (2009) I18 – the microfocus spectroscopy beamline at the Diamond Light Source. *Journal of Synchrotron Radiation*, 16, 818–824.

109. Kaneko, K., Kosugi, N. and Kuroda, H., (1989) Characterization of Iron Oxide-dispersed Activated Carbon Fibres with Fe K-Edge XANES and EXAFS and with Water Adsorption. *J. Chem. Soc., Faraday Trans. I,* 85, 869-881.

110. Jones, A.M., (2011) *private communication.*

111. Wada, M. and Okano, T., (2001) Localization of Iα and β IIβ phases in algal cellulose revealed by acid treatments. *Cellulose,* 8, 183–188.

112. Zhao, H., Kwak, J.H., Wang, Y., Franz, J.A., White, J.M. and Holladay, J.E., (2006) Effects of Crystallinity on Dilute Acid Hydrolysis of Cellulose by Cellulose Ball-Milling Study. *Energy & Fuels*, 20, 807-811.

113. Schofield, E.J., (2010) *private communication.*
114. Hocker, E., (2010) Maintaining a Stable Environment: Vasa's New Climate-Control System. *J. Preservation Technology*, 41, 3-9.
115. Hocker, E., (2006) From the Micro- to the Macro-: Managing the Conservation of the Warship, Vasa. *Macromol. Symp.*, 238, 16–21.
116. Jones, A.M., (2011) *private communication.*
117. Poggi, G., Giorgi, R., Toccafondi, N., Katzur, V. and Baglioni, P., (2010) Hydroxide Nanoparticles for Deacidification and Concomitant Inhibition of Iron-Gall Ink Corrosion of Paper. *Langmuir*, 26, 19084–19090.
118. Giorgi, R., Ambrosi, R., Toccafondi, N. and Baglioni, P., (2010) Nanoparticles for Cultural Heritage Conservation: Calcium and Barium Hydroxide Nanoparticles for Wall Painting Consolidation. *Chem. Eur. J.*, 16, 9374 – 9382.
119. Giorgi, R., Baglioni, M., Berti, D. and Baglioni, P., (2010) New Methodologies for the Conservation of Cultural Heritage: Micellar Solutions, Microemulsions, and Hydroxide Nanoparticles. *Accounts of Chemical Research*, 43, 695-704.
120. Giorgi, R., Chelazzi, D., Fratini, E., Langer, S., Niklasson, A., Rådemar, M., Svensson, J-E. and Baglioni, P., (2009) Nanoparticles of calcium hydroxide for wood deacidification: Decreasing the emissions of organic acid vapors in church organ environments. *J. Cultural Heritage*, 10, 206–213.
121. Giorgi, R., Chelazzi, D. and Baglioni, P., (2006) Conservation of acid waterlogged shipwrecks:nanotechnologies for de-acidification. *Appl. Phys. A*, 83, 567–571.
122. Giorgi, R., Bozzi, C., Dei, L., Gabbiani, C., Ninham, B.W. and Baglioni, P., (2006) Nanoparticles of Mg(OH)2: Synthesis and Application to Paper Conservation. *Langmuir, 21,* 8495-8501.
123. Carter, H.A., (1996) The chemistry of paper preservation .1. The aging of paper and conservation techniques, *J. Chemical Education,* 73, 417-420.
124. Carter, H.A., (1996) The chemistry of paper preservation .2. The yellowing of paper and conservation bleaching, *J. Chemical Education,* 73, 1068-1073.

125. Carter, H.A., (1996) The chemistry of paper preservation .3. The strengthening of paper, *J. Chemical Education,* 73, 1160-1162.
126. The Bookkeeper® Process is a product of Preservation Technologies; web site http://www.ptlp.com/deacid.html.
127. Zumbühl, S. and Wuelfert, S., (2001) Chemical Aspects of the Bookkeeper Deacidification of Cellulosic Materials: The Influence of Surfactant. *Studies in Conservation*, 46, pp. 169-180.
128. Polovka, M., Polovkova, J., Vizarova´, K., Kirschnerova, S., Bielikova, L. and Vrska, M., (2006) The application of FTIR spectroscopy on characterization of paper samples, modified by Bookkeeper process. *Vibrational Spectroscopy,* 41, 112–117.
129. Indris, S., Bork, D. and Heitjans, P., (2000) Nanocrystalline ceramic oxides produced by high-energy ball milling. *J. Materials Synthesis and Processing,* 8, 245-250.
130. Chadwick, A.V., Pooley, M.J., Rammutla, K.E., Savin, S.L.P. and Rougier, A., (2003) A comparison of the extended X-ray absorption fine structure of nanocrystalline ZrO_2 prepared by high-energy ball milling and other methods. *J. Phys.: Condens. Matter*, 15, 431–440.
131. Walker, M., (2009) Honeybees sterilise their hives. http://news.bbc.co.uk/earth/hi/earth_news/newsid_8152000/8152574.stm
132. Orsi, R.O.; Sforcin, J.M., Rall, V.L.M., Funari, S.R.C., Barbosa, L., and Fernandes J.R.A., (2005) Susceptibility profile of Salmonella against the antibacterial activity of propolis produced in two regions of Brazil. *Journal of Venomous Animals and Toxins including Tropical Diseases,* 11, 109–116.
133. Sugimoto, Y., Iba, Y. and Kayasuga, R., (2003) Inhibitory effects of propolis granular A P C on 4-(methylnitrosamino)-1-(3-pyridyl)-1-butanone-induced lung tumorigenesis in A/J mice. *Cancer Lett.,* 193, 155–159.
134. Hosnuter, M., Gürel, A., Babucçu, O., Armutcu, F., Kargi, E. and Işikdemir, A.. (2004). The effect of CAPE on lipid peroxidation and nitric oxide levels in the plasma of rats following thermal injury. *Burns,* 30, 121–125.
135. http://www.promer.org/getdoc.php?docid=860

136. Gregoris, E. and Stevanato, R., (2010) Correlations between polyphenolic composition and antioxidant activity of Venetian propolis. *Food and Chemical Toxicology,* 48, 76–82.

137. Alencar, S.M., Oldoni, T.L.C., Castro, M.L., Cabral, I.S.R., Costa-Nieto, C.M., Cury, J.A., Rosalen, P.L. and Ikegaki, M., (2007) Chemical composition and biological activity of a new type of Brazilian propolis: red propolis. *J. Ethnoph.* 113, 278–283.

138. Gomez-Caravaca, M., Gomez-Romero, M., Arraez-Roman, D., Segua-Carretero, A. and Fernandez-Gutierrez, A., (2006). Advances in the analysis of phenolic compounds in products derived from bees. *J. Pharm. Bio. Anal.,* 41, 1220–1234.

APPENDIX A

Publications from work in this thesis

1. Shelley L.P. Savin, Aaron Berko, Aran N. Blacklocks, William Edwards, Alan V. Chadwick

   The applications of X-ray absorption spectroscopy in the study of nanocrystalline materials and electrochemical systems

   Comptes Rrendu. Chimie 11 (2008) 948-963

2. A. Berko, A.D. Smith, A.M. Jones, E.J. Schofield, J.F.W. Mosselmans, and A.V .Chadwick

   XAS studies of the effectiveness of iron chelating treatments of

   Mary Rose timbers

   Journal of Physics: Conference Series 190 (2009) 012147

3. A.V. Chadwick, A. Berko, E.J.Schofield, A.M. Jones, J.F.W. Mosselmans and A.D. Smith

   The Application of Microfocus X-ray Beams from Synchrotrons in Heritage Conservation

   International Journal of Architectural Heritage (in press)